Implementation of an unequal path length, heterodyne interferometer on the MOCHI LabJet experiment

Alexander Harrison Card

A thesis
submitted in partial fulfillment of the
requirements for the degree of

Master of Science in Aeronautics & Astronautics

University of Washington

2017

Committee:

Setthivoine You

Raymond Golingo

Program Authorized to Offer Degree:
William E. Boeing Department of Aeronautics & Astronautics

University of Washington

Abstract

Implementation of an unequal path length, heterodyne interferometer on the MOCHI LabJet experiment

Alexander Harrison Card

Chair of the Supervisory Committee:

Assistant Professor Setthivoine You

Aeronautics & Astronautics

The MOCHI LabJet experiment aims to explore the stability of magnetic flux tubes through the medium of laboratory astrophysical plasmas. The boundary conditions of large gravitational bodies, namely accretion disks, are replicated and allowed to influence a plasma over short timescales. Observation of the plasma is enabled through use of a variety of fast diagnostics, including an unequal path length, heterodyne, quadrature phase differen-tial interferometer, the development and implementation of which is described in detail. The LabJet gun, a triple-electrode planar plasma gun featuring azimuthally symmetric gas injection achieves a new, long-duration, highly-stabilized, jet plasma formation. The line-integrated density in this new LabJet formation is found to be $n_e = (6 \pm 3)\text{x}10^{20}$ $[m^{-2}]$. By observing the axial expansion rate of the jet over multiple chord locations (all perpendic-ular to the propagation axis), the interferometer provides an Alfvén velocity measurement of $v_A = 41.3 \pm 5.4$ $\left[\frac{km}{s}\right]$, which at the jet density observed indicates an axial magnetic field strength of $B_Z = 0.15 \pm 0.04$ $[T]$. Various other laboratory components are also detailed, such as a shot-based MDSplus data storage architecture implemented into the LabVIEW experiment control code, and the production and performance of ten fast neutral gas injection valves which when fired in unison provide a total particle inventory of $(7.8 \pm 0.6)\text{x}10^{23}$ $[HI\ particles]$.

TABLE OF CONTENTS

LIST OF FIGURES

LIST OF TABLES

ACKNOWLEDGMENTS

Aside from the reading committee, the author wishes to express sincere appreciation to his lab mates Evan Carroll, Jens von der Linden and Eric Sander Lavine. The experience of building the lab with you guys will forever be a cherished one. Also the outstanding members of the ZaP Flow Z-Pinch research team, namely Dr. Raymond Golingo, Dr. Brian Nelson, and Mike Ross. I would also like to acknowledge Dr. Tom Mattick; without his experienced input I might still be working on the amplifier. Finally I would like to extend my gratitude towards Dr. Simon Woodruff, whose continued support enabled me to pursue a higher education.

to my family

Chapter 1

THE MOCHI LABJET EXPERIMENT

1.1 Introduction

MOCHI is an acronym for Measurements Of Canonical Helicity Injection, which summarizes the central theme of this laboratory: experimental investigations into canonical helicty. MOCHI has made contributions to the theoretical side of canonical helicity [26, 20, 25], and is on the verge of doing so from an experimental point of view with *LabJet*, a newly-commissioned laboratory astrophysical jet experiment. LabJet is purposed to replicate the boundary conditions of gravitationally-active objects in order to experimentally investigate the stability of the flux tubes (plamsa jets) that form as a result [3, 27, 23]. On an experimental level, three-dimensional magnetic and ion-doppler spectroscopic measurements will be taken on LabJet in order to observe the exchange between different types of canonical helicities, particularly the conversion between magnetic helicity and kinetic flow helicity [26]. The goal will be to invetigate whenther this helicity conversion could be a mechanism of astrophysical jet collimation seen in nature [26, 20, 27].

1.1.1 Experimentally simulating the boundary conditions of astrophysical jets

In nature, astrophysical jets launch from accretion disk systems that feature massive, centralized objects, the scale of these formations ranging from protostellar jets (scale of a solar system) to jets emanating from active galactic nuclei (scale of a galaxy). This difference in jet scaling indicates that there is not a prerequisite threshold in physical size of these jets, but rather on dimensionless parameters [3]. The LabJet experiment aims to meet the

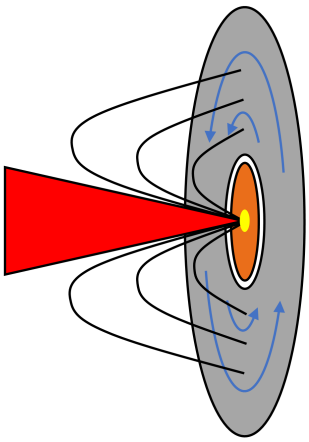

Figure 1.1: Cartoon schematic of astrophysical jet

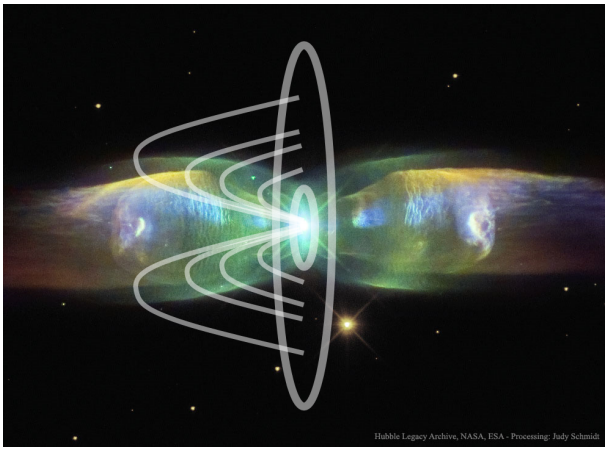

Figure 1.2: NASA image of astrophysical jet. Overlaid is the equivalent electrode setup that would create such a jet, as well as the section of the solenoid field line resulting from the magnetically active core.

boundary conditions implied by these dimensionless parameter [6].

The boundary conditions of an astrophysical jet are: azimuthal symmetry, a centralized mass source, a toroidally-rotating accretion disk (figure 1.1), a poloidal magnetic field (overlaid lines seen in figure 1.2), and a radial electric field. The radial electric field is produced from the interaction between the poloidal magnetic field and rotating accretion disk, and drives current along the poloidal field lines. In previous laboratory astrophysical jet experiments, two-electrode planar plasma guns have simulated these boundary conditions to a satisfying extent. The azimuthal symmetry and poloidal field boundary conditions are easily replicated by a planar plasma gun with a solenoid bias field coil, however the mass source and rotating accretion disk is impossible to replicate in a laboratory experiment. Therefore to produce the required radial electric field, power supplies are discharged over the planar electrodes: the inner electrode (cathode) representing the central object, and outer electrode representing the accretion disk (anode) [3, 27, 17, 2].

The LabJet experiment features a spherical vacuum chamber, 1.4 m in diameter (seen in figure 1.3). This chamber satisfies another boundary condition inherent to the space surrounding astrophysical jets: the walls are far enough away that they do not provide a stabilizing effect on the plasma jet formations. The vacuum chamber features two 1 m flanges which house two planar plasma guns: *LabJet*, and *SpheromakGun*. SpheromakGun is a two-electrode planar plasma gun which is on loan from Los Alamos National Laboratory (LANL). The LabJet gun is a triple-electrode planar plasma gun (figure 1.4); a new configuration to date. Having a second cathode electrode allows control over the radial current profile across the jet through the potentials supplied by the lab power supply units (PSUs, section 1.2). Furthermore, the azimuthally symmetric gas injection featured in LabJet allows the plasma to rotate toroidally at the base, effectively creating a new type of operation for a planar plasma gun [6]. Combined access of our jets to certain radial current profiles, increased jet aspect ratios, and rotation creates highly stabilized flux tubes (see chapter 3) [23, 20].

1.1.2 Motivations for an electron density measurement

One of the goals of LabJet is to study the flows of magnetic flux tubes (jets), therefore it is important to measure the time-dependent plasma density of LabJet's jet. In fact for any new plasma experiment the three initial measurements taken (post-commissioning phase) are: density (n), temperature (T), and magnetic field (B). These quatities serve as common comparision between all plasma experiments [2, 9]. Heterodyne, quadrature phase differential interferometers are overwhelmingly utilized to measure electron density in plasma experiments [16, 4, 18, 17, 14, 10, 13, 7, 12]

This thesis details the design, construction, and first results of a new, single-chord, heterodyne, quadrature phase differential interferometer purposed to measure electron density (n_e) of the plasma produced by LabJet. The interferometer was motivated by a diagnostic built for an astrophysical jet experiment which was similar to LabJet in nearly all experimental constraints [18, 17], particularly the difficulty of equal length interferometry based on the size of the chamber and unavailability of space in the laboratory. Chapter 2 provides

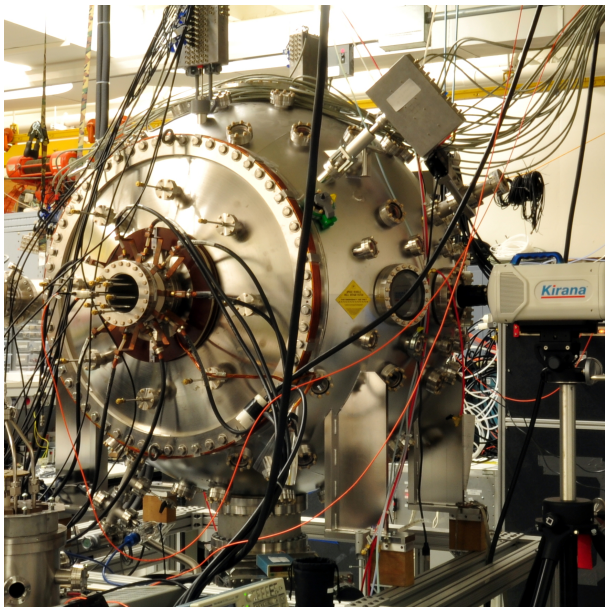

Figure 1.3: Picture of MOCHI vacuum chamber. Note that it is highly modular, featuring an even spread of 192 ConFlat ports of various sizes.

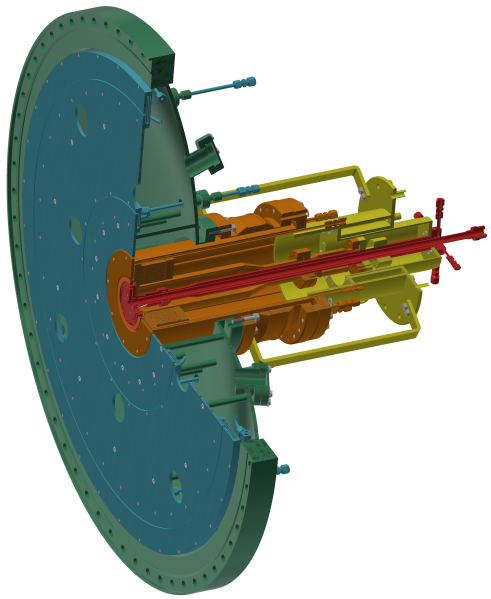

Figure 1.4: CAD model of plasma gun. The outer electrode (blue) connects to the chamber (green), which itself is connected to the ground plate (yellow). The middle (orange) and inner (red) electtrodes can be biased at up to 10 kV [6].

detail on the design and construction of the diagnostic, and chapter 3 displays a discussion of the results of the electron density measurements.

1.2 Hardware and software of MOCHI

The LabJet experiment has access to a whole host of hardware and software that that was obtained from typical sources (commercial, inherited), however a large amount of the laboratory infrastructure was built in-house by graduate students. LabJet gun is powered by twin 10 kV, 600μF pulsed PSUs (figure 1.5) [6], and fueled by ten fast gas valves (section 1.3), each powered by a 1.5 kV, 25 μF independent pulsed PSUs. The bias magnetic field

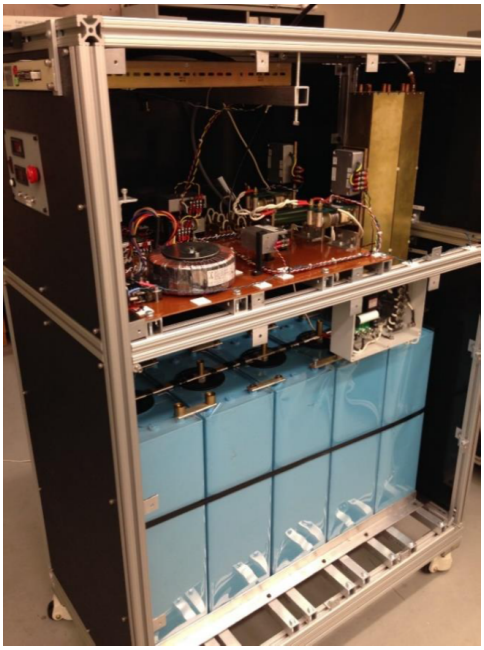

Figure 1.5: Picture of main power supply bank. These were built in-house, and feature a 10 $[kV]$, 600 $[\mu F]$ capability. Read E. Carroll's thesis for more information [6].

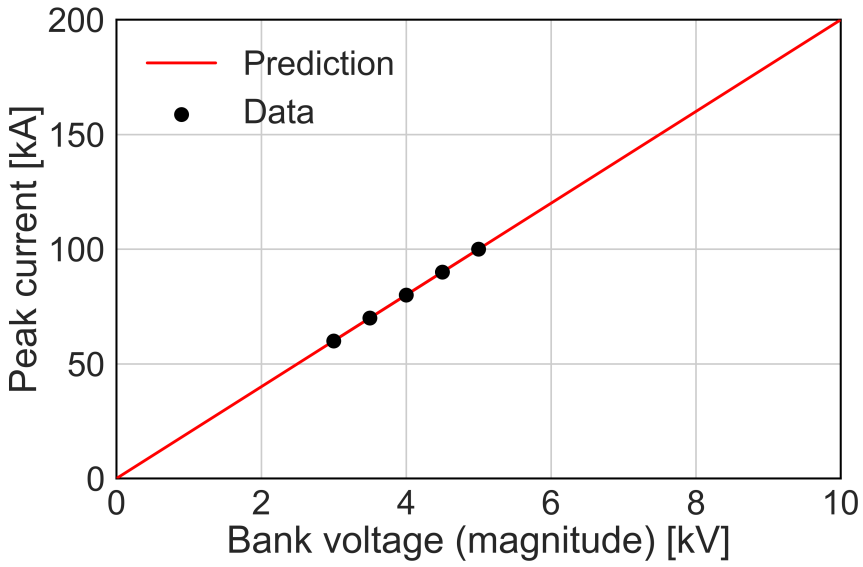

Figure 1.6: Prediction of peak main bank currents. Note that the error bars are smaller than the size of the data points.

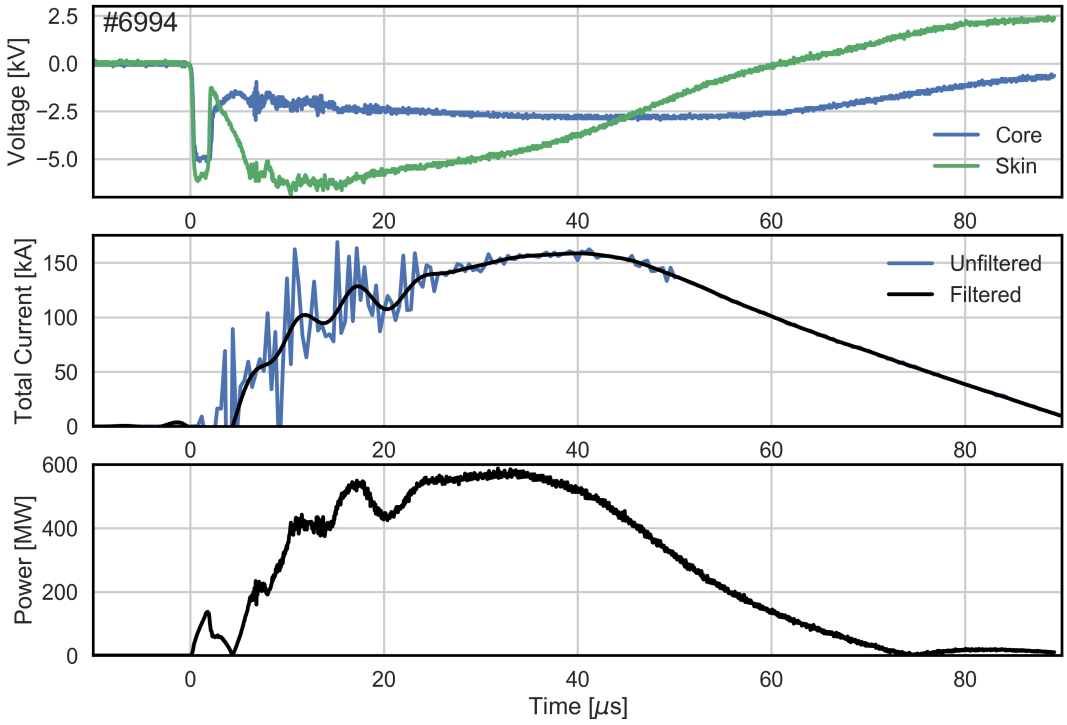

Figure 1.7: Voltage, current, and power traces for shot #6994. The voltage traces are independently measured by Tektronix probes. Total current is measured by a rogowski coil, and numerically filtered by a 188 [kHz], 5th-order butterworth filter. Power is calculated using the filtered current, and the average of the two voltage traces.

is provided by a solenoid seated directly behind the two inner electrodes (figure 1.4), and is powered by a 450 V, 48 mF pulsed PSU.

Typical LabJet gun voltage and current traces (shot #6994) are seen in figure 1.7. The voltages are measured using two Tektronix fast voltage probes, and an in-house rogowski coil used to measure the gun current. The rogowski coil is sensitive to noise pickup during the first 20 μs of a plasma discharge. This turned out to be common feature of many diagnostics, including the diagnostic described in chapter 3. It is likely due to the PSU ignitron firing, causing the electrodes to quickly energize to the set bank voltage (as seen in the voltage trace in figure 1.7), as well as the initial plasma breakdown and jet formation (see section 3.2.1, chapter 3). A 188 kHz, numerical 5th-order butterworth filter was used to filter the current data, and along with the averaged voltage the $P = V_{avg} I_{filtered}$ power was calculated to be $\sim$ 600 MW for a bank charge of 6 kV (figure 1.7). The main banks delivering this power the LabJet gun were built in-house, and are seen in figure 1.5. Figure 1.7 also portrays a prediction of possible peak currents for a single PSU, given the history of a only a few shots. Theoretically, at 10 kV, the gun should be able to hit a peak current of 400 kA with both banks firing.

The LabJet experiment had access to a Kirana fast imagine camera (right side, figure 1.3). This camera has a frame rate up to 5 MHz, and a total of 180 $frames$. During the operational campaigns, the Kirana camera was typically set to 2 MHz with a 500 ns frame exposure. This produced a time window of 90 μs, which covered the whole relevant duration of LabJet.

The LabJet experiment uses National Instruments and Tectronix equipment to interface with the experiment [23]. The available timing and data acquisition (DAQ) cards are as follows:

- 16 timing channels with independent counters (2 x PXI-6602)
- 8 channels at 2.5 MHz (3 x PXI-6133)

- 96 channels at 50 MHz (3 x NI-5752/PXIe-7962R)

- 8 oscilloscope channels (2 x Tektronix TDS-2024B)

1.2.1 LabVIEW/MDSplus interface

The MOCHI LabJet experiment is controlled by MochiControl: a single LabVIEW (LV) virtual instrument (VI) that is designed to simultaneously control all timings, relays and data flow [24, 23]. All MochiControl operation I/O is optically isolated from the experiment [6, 23]. MochiControl is interactive in real-time, a capability made possible through the implementation of a multi-threaded, producer-consumer architecture. In this architecture the producer and consumer refer to two independent threads that are implemented as `while` loops which communicate with each other via a `queue` that runs through both threads simultaneously. The producer contains an event structure which produces and enqueues a case structure reference, allowing the consumer to dequeue the reference and take the action according to its case structure. Running through the consumer thread is a data cluster called Experiment State cluster, which is a conglomerate of every data array that the LabJet experiment interacts with; all experimental settings, user-defined labels, and recorded data are stored and referenced from this cluster throughout the operational phases of MochiControl during a plasma pulse [24, 23].

An MDSplus tree structure has been produced which was designed using the Experiment State cluster as an outline. MDSplus is a shot-based data storage architecture that lends itself well to plasma experiments [22]. In order to interface with MDSplus, a LabVIEW library was developed (see appendix C for full code). Two routines were created using this library: `MDSstore` which stores all information to the tree (including data), and `MDSload`, which loads all experiment settings and labels from a previous shot (excluding data). Figure 1.9 depicts the flow diagram of `MDSstore` and how it interacts with the Experiment State cluster and the MochiControl code as a whole [23, 24]. Similarly, figure 1.10 depicts the flow diagram of `MDSload` and how it interacts with the Experiment State cluster. The data

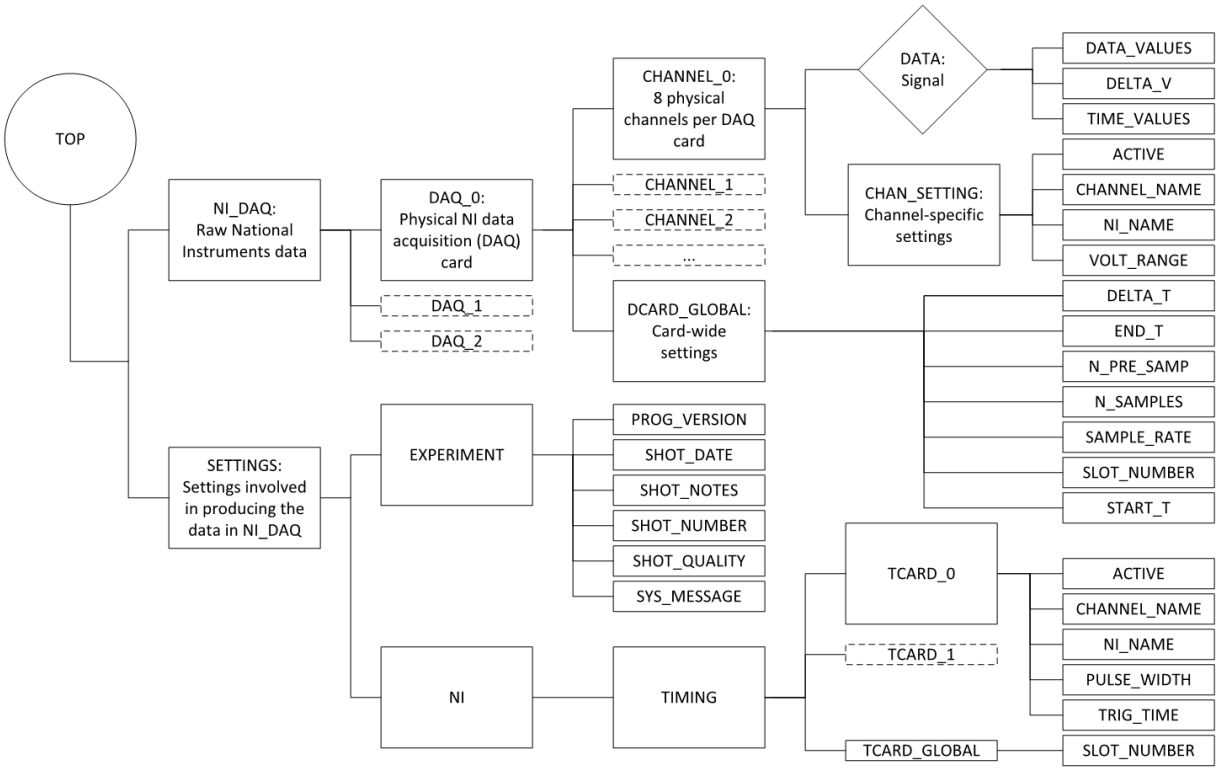

Figure 1.8: Breakout of proto tree, the MDSplus model tree

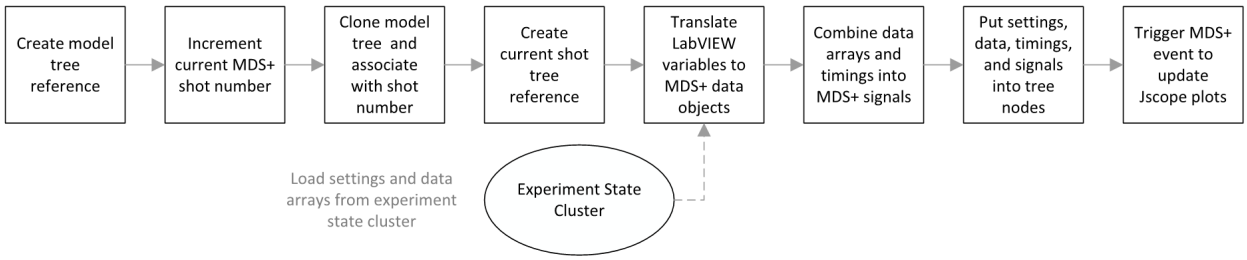

Figure 1.9: Flow diagram of MDSplus Store. Figure courtesy of von der Linden, J.

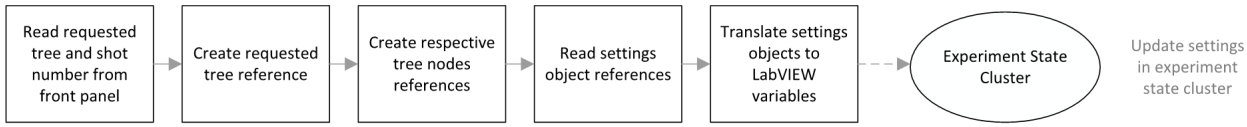

Figure 1.10: Flow diagram of MDSplus load. Figure courtesy of von der Linden, J.

created from NI DAQs was straightforward to store to MDSplus, but peripheral devices (such as the oscilloscopes) external Python scripts had to be called via a Windows CMD function within LV, the source code of this can be found in a recent Zenodo release [5].

1.3 Neutral particle inventory

The LabJet plasma gun features azimuthally symmetric neutral gas injection, which is achieved by a complicated system of plenum gas runners, located between the electrodes and outer chamber flange [6]. There is a pair of azimuthally symmetric injection plenums for each nested plasma gun (inner, middle). In order to fuel symmetrically, the inner and middle injection plenums require one valve, and both of their paired outer electrode plenums require four valves each [6]. Therefore, for full control over the azimuthally symmetric gas injection, ten, independently-timed fast gas valves were required.

The ten required gas valves were built entirely in-house (figure 1.12), and the engineering drawings used can be found in appendix B. The design of the fast gas valves was based off valves inherited from LANL to accompany the SpheromakGun; a design which initially orig-

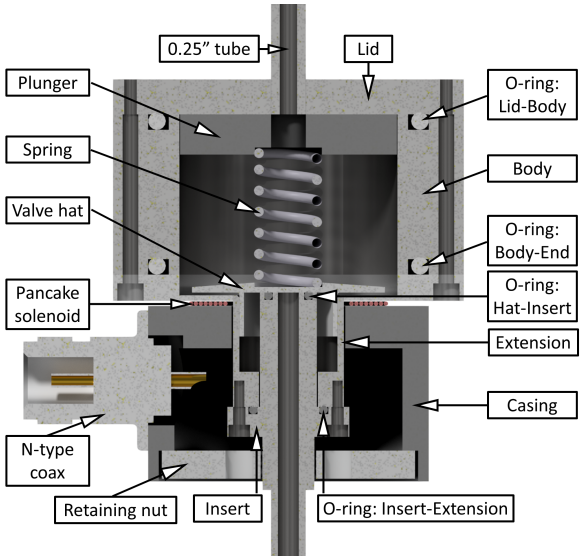

Figure 1.11: Cutaway of fast valve CAD model

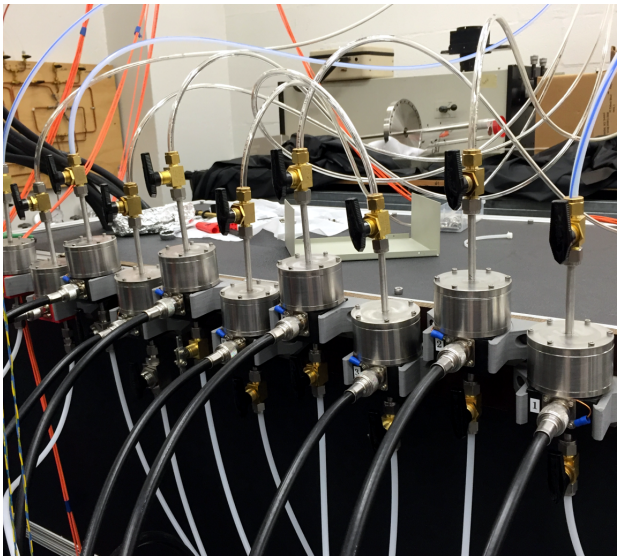

Figure 1.12: Pictures of all completed fast valves

inated from the California Institute of Technology [1]. The valve parts and part dimensions were made identical to the inherited valves, however modifications were made to enable the large-scale manufacturing of the valves by hand (figure 1.11).

Two properties that are unique compared to commercial valves are sub-millisecond opening times and large gas throughput. The the valve operates by driving a pancake solenoid (with a pulsed, 10-channel PSU), which produces a magnetic field that then induces opposite image currents within the "brim" of the valve hat, causing it to repel which drives it open (figure 1.11). Due to the high relative permeability of stainless steel, the bottom of the stainless steel body is designed to 0.04 *in* to avoid losses in the magnetic field. The spring compression and pressure difference (internal pressure typically set at $80 - 100$ *psi*) simultaneously provide the restoring force on the valve hat, which is made of aluminum: a lightweight, rigid material which has an order magnitude higher electrical conductivity than the stainless steel that surrounds it, helping to ensure that the image currents produced in the body do not have a negative impact on the valve opening.

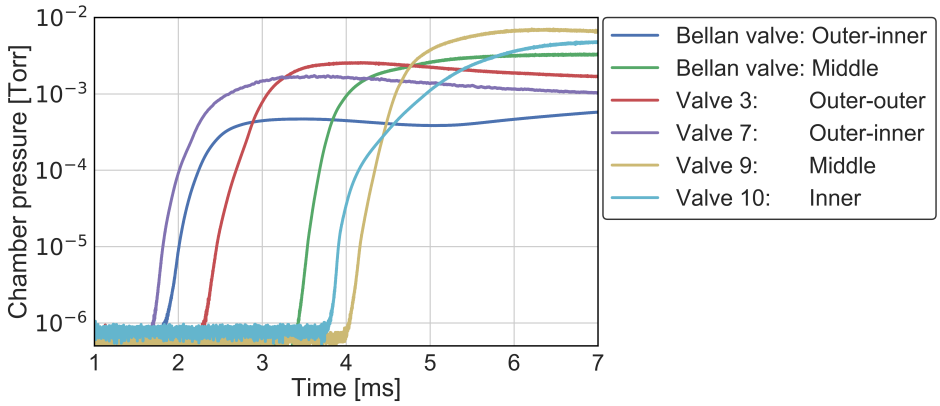

Figure 1.13: Comparison of select fast gas valves.

The valve injects gas from the inside of the body, through a narrow inlet, into the vacuum chamber, and as such an analogy can be drawn to a rocket nozzle firing into a vacuum. Since the system will be experiencing choked flow, the only way to increase the throughput is to widen the diameter of the nozzle throat [21]. The value is built around a $\frac{1}{4}$" tube as an inlet, which allows for peak pressures reaching $\sim 10^{-3}$ $torr$ with a ~ 1 ms rise time, or, a micron in a millisecond (see figure 1.13). This measurement was taken using a fast ion gauge built in-house [19]. Also in this plot you can see that the MOCHI vacuum chamber is able to pump down to $\sim 3x10^{-7}$ $[torr]$, represented by the zero line. The chamber is held to such low pressures by a Sumitomo Marathon CP-12 adsorption cryopump.

With ten valves firing at once, it is beneficial to determine the total density of neutral particles sent into the chamber during a plasma shot. To do this, the chamber was isolated from its vacuum pumps, a single valve was fired, the final chamber pressure was recorded with a thermocouple pressure gauge, and the pumps were re-opened again allowing the chamber pressure to drop back to high vacuum. The average pressure that each valve sent into the chamber was $\Delta P_{avg} = (0.21 \pm 0.02)$ $torr$.

Utilizing the ideal gas law (equation 1.1) with $T = 300$ K, $V = 11.5$ m^3, and $k_B = 1.38x10^{-23}$ JK^{-1}, it was determined that a total particle count of $N_{valves} = (7.8 \pm 0.6)x10^{23}$ $particles$

were fired into the chamber: a little over one mole of neutral hydrogen. This measurement corresponds to a total neutral density of $n_{valves} = (6.8 \pm 0.6)x10^{22}$ $[m^{-3}]$ over the whole chamber. The uncertainty was calculated using the error propagation displayed in equation 1.2. These neutral particles represent the inventory that the plasma dynamics will act upon during an experimental shot procedure, and the results of chapter 3 will discuss the dynamics of the time-dependent electron densities.

$$PV = Nk_BT \rightarrow \Delta N_{valves} = 10\frac{\Delta P_{avg}V}{k_BT} \tag{1.1}$$

$$\sigma_{\Delta N} = \frac{\partial \Delta N}{\partial \Delta P_{avg}}\sigma_{P_{avg}} = 10\frac{\sigma_{P_{avg}}V}{k_BT} \tag{1.2}$$

Chapter 2

UNEQUAL PATH LENGTH, HETERODYNE, QUADRATURE PHASE-DIFFERENTIAL INTERFEROMETER

This chapter will detail the theory, construction, and operation of an unequal path-length, heterodyne, quadrature phase-differential interferometer: the diagnostic used to produce the results of chapter 3. These diagnostics have become a inexpesnive and robust diagnostic that can measure electron densities reliably since their introdcution in the late 1970s [16, 4]. Appendix A showcases the effort to re-create this diagnostic using monolithic additive manufacturing techniques. This effort was completed as a side project for Woodruff Scientific, Inc.

2.1 Theory

This diagnostic is a passive diagnostic, meaning it does not alter the properties of the plasma. The only means of communication it has is through the manipulation of the index of refraction N of the laser media by the plasma itself. Therefore we need to begin this discussion at the plasma dispersion relation.

2.1.1 Dispersion Relation

In a magnetized plasma, O-mode waves are defined by a wave propagation vector that is perpendicular to the magnetic field [2, 12, 9]. For this diagnostic, the dispersion relation is the same as that of the unmagnetized case, wherein the wave is a light wave that is modified by the plasma [12]. The light wave in this diagnostic originates from the laser, and is modified by the changing index of refraction N of the plasma. This change in N is small enough that the angle of refraction, introduced according to Snell's Law, is negligible since the laser is

intersecting the azimuthally symmetric perpendicularly along the density gradient ∇n_e [17].

We begin with a simplified version of the Appleton-Hartree dispersion relation [12, 10, 13, 7]. Solving the dispersion relation (equation 2.1) for the index of refraction N yields equation 2.2, where the plasma frequency is ω_p, the wave source (laser) frequency is ω, and $X = \frac{\omega_p^2}{\omega^2}$.

$$N^2 = 1 - X \tag{2.1}$$

$$N = \sqrt{1 - \frac{\omega_p^2}{\omega^2}} \tag{2.2}$$

We can assume that the laser frequency is much larger than the plasma frequency, $\omega >> \omega_p$, so the dispersion relation becomes equation 2.3.

$$N = 1 - \frac{\omega_p^2}{2\omega^2} \tag{2.3}$$

The plasma frequency ω_p and laser frequency ω are both defined in equation 2.5. We see that the plasma frequency is defined with respect to the electron density n_e, and the laser frequency is defined with respect to a characteristic cutoff density of electrons in the plasma (equation 2.4). The cutoff density represents the maximum density that can be measure, and for a Helium-Neon (HeNe) laser - the laser used for this interferometer - the cutoff density is $n_c = 3\text{x}10^{27}\ \ [m^{-3}]$. In equations 2.5 and 2.4, c is the speed of light in a vacuum, λ_{laser} is the source laser's wavelength, e is the electron charge, m_e is the mass of the electron, and ϵ_o is the permitivity of free space.

$$n_c = \frac{4\pi^2 c^2 m_e \epsilon_o}{\lambda_{laser}^2 e^2} \tag{2.4}$$

$$\omega_p = \sqrt{\frac{n_e e^2}{m_e \epsilon_o}}\ ; \quad \omega = \sqrt{\frac{n_c e^2}{m_e \epsilon_o}} \tag{2.5}$$

Inserting into equation 2.3 yields our final reduced form of the Appleton-Hartree dispersion relation (equation 2.6): the index of refraction defined with respect to a ratio of electron density to laser cutoff density.

$$N = 1 - \frac{n_e}{2n_c} \tag{2.6}$$

2.1.2 Refractive Index Interferometry

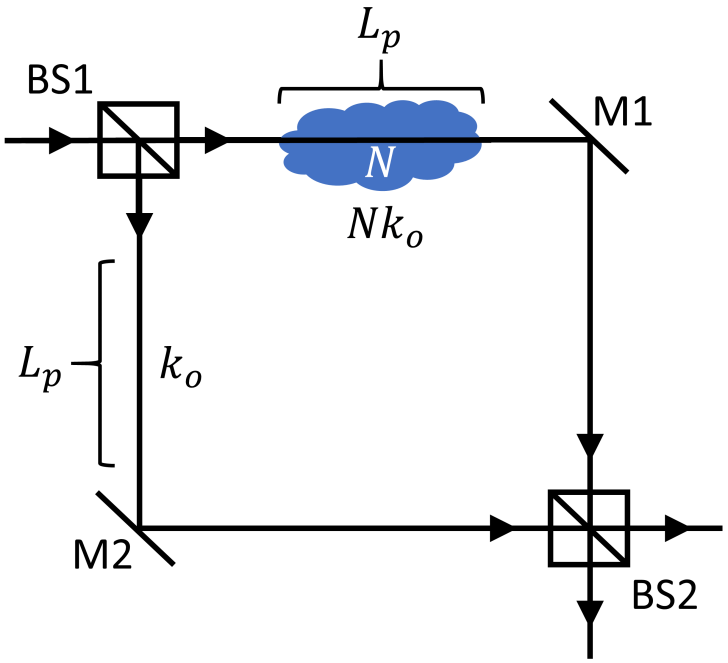

Figure 2.1: Basic schematic of Mach-Zehnder interferometer

The phase angle difference $\Delta\phi$ between two arms of a Mach-Zehnder interferometer is determined by taking the difference between the phase angle of the two propagating waves: inside (scene beam) and outside (reference beam) the plasma. Note that outside the plasma, we assume the index of refraction to be 1 (e.g. figure 2.1). This is illustrated in equation 2.7, where k_o is the free-space wavenumber, and L_p is the length of plasma over which the

wave propagates:

$$\Delta\phi = \int_0^{L_p} k_{plasma} dl - \int_0^{L_p} k_o dl = \int_0^{L_p} (Nk_o - k_o) dl = \int_0^{L_p} (N-1)\frac{\omega}{c} dl \tag{2.7}$$

The interferometer takes two transits across the plasma which doubles the phase angle difference imposed by the plasma's index of refraction. We utilize the two relations $\omega = 2\pi\nu_{laser}$ and $\nu_{laser} = \frac{c}{\lambda_{laser}}$ to arrive at equation 2.8.

$$\Delta\phi = 2\int_0^{L_p} (N-1)\frac{\omega}{c} dl = 2\int_0^{L_p} (N-1)\frac{2\pi}{\lambda_{laser}} dl = \frac{4\pi}{\lambda_{laser}} \int_0^{L_p} (N-1) dl \tag{2.8}$$

Inserting the reduced form of the Appleton-Hartree dispersion relation (equation 2.6) yields:

$$\Delta\phi = \frac{4\pi}{\lambda_{laser}} \int_0^{L_p} (1 - \frac{n_e}{2n_c} - 1) dl = \frac{1}{n_c}\frac{2\pi}{\lambda_{laser}} \int_0^{L_p} n_e dl \tag{2.9}$$

We substitute the inverse equation for the laser cutoff density (equation 2.10) into the result of equation 2.9 to arrive at equation 2.11: the final form of phase angle difference defined with respect to the line-integrated density.

$$\omega^2 = \frac{4\pi^2 c^2}{\lambda_{laser}^2} = \frac{n_c e^2}{m_e \epsilon_o} \quad \rightarrow \quad \frac{1}{n_c} = \frac{\lambda_{laser}^2 e^2}{4\pi^2 c^2 m_e \epsilon_o} \tag{2.10}$$

$$\Delta\phi = \frac{\lambda_{laser} e^2}{2\pi c^2 m_e \epsilon_o} \int_0^{L_p} n_e dl \tag{2.11}$$

A single chord interferometer can only take a single sample of the line-integrated density of the plasma. This is not enough information to make assertions about the cross-sectional density profile. Therefore we can simplify the integral in equation 2.11, as seen in equation 2.12.

$$\Delta\phi = \frac{\lambda_{laser} e^2}{2\pi c^2 m_e \epsilon_o} n_e L_p \tag{2.12}$$

At this point we can define the line-integrated electron density $\overline{n}_e$ (equation 2.13). The line-integrated density is dependent on $\Delta\phi$, the quantity that the experimental interferometer will ultimately measure, and is given numerically in equation 2.14.

$$\overline{n_e} = n_e L_p \tag{2.13}$$

$$\overline{n}_e = \frac{2\pi c^2 m_e \epsilon_o}{\lambda_{laser} e^2} \Delta\phi = 2.78\text{x}10^{20} \Delta\phi \ \left[m^{-2}\right] \tag{2.14}$$

2.2 An empirical verification: Spatially periodic nature of interference

The interferometer utilizes unequal beam path lengths. In order to do so, it is first necessary to determine the spatial interference envelope of the laser. This interference envelope is periodic in ΔL path length difference between the scene and reference beams, and arises from laser cavity spatial resonant modes beating with the laser's Doppler broadened, narrow frequency band [17, 15].

Typical interferometers use scene and reference beams that are equal in path length. This guarantees that the interference signal will be at maximum constructive interference [15], but often times promotes tricky optical setups. By allowing the scene beam to be unequal in length to the reference beam, the optical setup can easily conform to any restrictions imposed by the lab. However, effort must be made to make sure that the interference is indeed maximized. In this chapter, the ΔL path length difference over which the laser interference is spatially periodic will be determined empirically.

2.2.1 Optical design used in the verification

The optical setup used to measure the spatially periodic ΔL path length difference was a standard Michelson interferometer with a variable scene arm, as seen in figure 2.2 [18, 17]. In order to negate the effects of beam divergence as the scene beam arm is extended, the beam is expanded using $EL1$ and $EL2$. $EL1$ has an effective focal length (EFL) of 25 mm, and

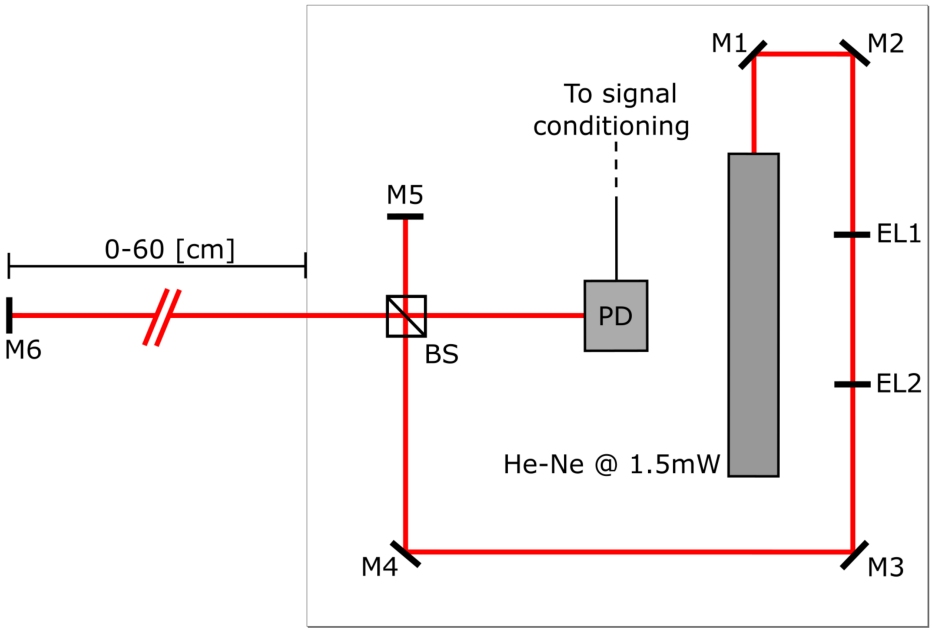

Figure 2.2: Optical setup for periodic interference envelope measurement

Laser	Gas tube	Helium-Neon @ 1.5 [mW]
M1-M4	Steering mirrors	1” circular
M5	Reference mirror	1” circular
M6	Scene mirror	2” square
EL1	Expansion Lens	Plano-concave (KPC043)
EL2	Expansion Lens	Plano-convex (KPX118)
BS	Recombination beamsplitter	1” cube
PD	Photodiode	Newport 818-BB-21

Table 2.1: Optical components utilized for periodic envelope measurement. Corresponds to figure 2.2

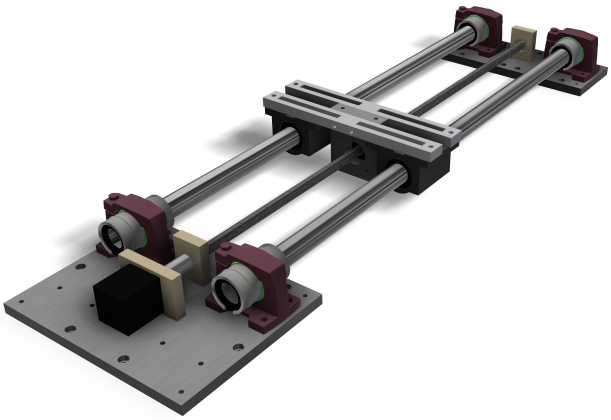

Figure 2.3: CAD model of the Auto-Stage

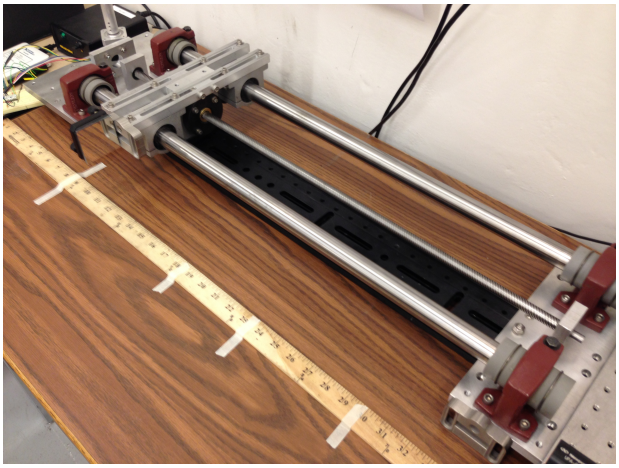

Figure 2.4: Picture of the Auto-Stage

$EL2$ has an EFL of 500 mm. Therefore the beam expands by a factor of $\frac{500}{25} = 20$ $times$, and the divergence angle, inverse to the magnification, is reduced by a factor of $\frac{1}{20}$ [15]. The scene beam expansion cavity is controlled by the Autostage (figures 2.3 and 2.4), a custom-built linear translation stage that expands from $0 - 60$ cm. The photodiode PD was not sensitive enough to pick up the signal when terminated into a 50 Ω resistor (for which it is calibrated). Since the photodiode acts as a current source, a higher termination value (1 $M\Omega$) was used to artificially boost the signal. While this did introduce some amplitude variations in the photodiode signal (reflective noise from large impedance mismatch), the amplitude modulation was small compared to the interference signal. As we are only looking for the relative interference peaks, modulation of interference amplitude does not effect the final result.

2.2.2 Result: Spatially periodic interference of our laser

The data, seen in figure 2.5, portrays the periodic nature of interference as dependent on the $\frac{\Delta L}{2}$ mirror difference. The data begins at a maximum at 0 cm mirror offset (equal length scene and reference beams). From this plot, we see that the interference is periodically maximum

at twice the mirror distance of $\Delta L = 70\ cm$ However since the final optical setup involves reflecting the scene beam back along the same axis (as it does in this optical design), only the mirror distance of $\frac{\Delta L}{2} = 35\ cm$ (~ 14") is necessary information for the final diagnostic setup.

From figure 2.2, we can conclude that the diagnostic is robust against deviations in the ΔL path length difference due to the width of maximum interference, and the fact that the interference never entirely disappears. This means that no matter where the setup lands on the ΔL path length difference, the diagnostic will still provide a working interference signal.

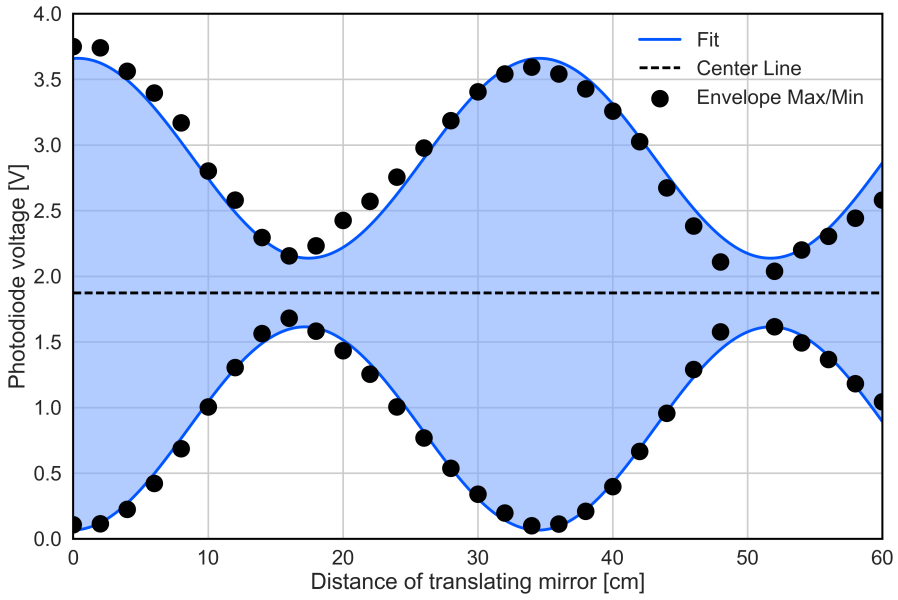

Figure 2.5: Spatially periodic interference envelope. Note that 0 cm refers to equal length scene and reference beams. From this plot we infer that the interference maximum occurs periodically over a integer multiplicative of a $\Delta L = \sim 70\ cm$ path length difference.

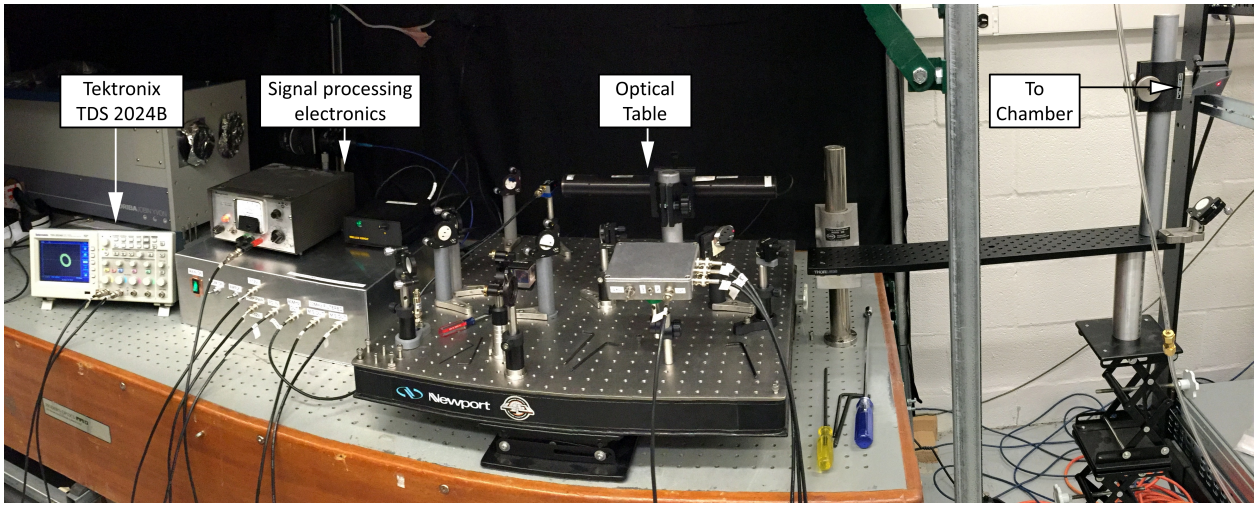

Figure 2.6: Picture of completed interferometer diagnostic. Each component labeled is discussed in the following sections.

2.3 Optical design of the interferometer

This optical design is neatly summarized as a "pseudo Mach-Zehnder," with the Acousto-Optical Modulator (AOM) serving as the leading beamsplitter. Because we are not utilizing equal path length beam arms we do not need to stress the alignment lengths prior to the secondary beamsplitter, therefore this beamsplitter functions in a Michelson recombination configuration and boasts its inherent ease of alignment [18, 17]. Since only a single beam is sent off to the chamber (and back again), the optics are compact; they all fit on a single 25" $\times$25" table (figure 2.6). The response of the diagnostic to the changing index of refraction is doubled, since it operates in a double-pass configuration, and the due to the results of section 2.2.2 the diagnositc is robust against variances in ΔL path length difference away from an integer maxima [18, 17]. That being said, the path length difference in the optical setup was accurately (on the order of 1 cm) measured, and adjusted to hit an integer maximum. Adjustment of ΔL was achieved by simply moving the optical table until an integer maxima was found.

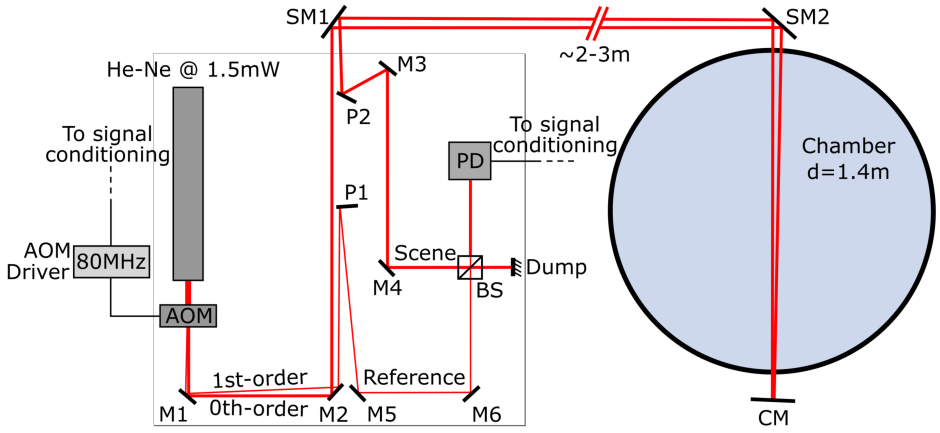

Figure 2.7: The unequal path length optical schematic implemented on the MOCHI LabJet experiment.

Laser	Gas tube	Helium-Neon @ 1.5 $[mW]$
AOM	Acousto-optical modulator	Isomet 1205C-2 ($f_o = 80$ $[MHz]$)
AOM Driver	AOM function generator	Isomet 232A-1 ($f_o = 80$ $[MHz]$)
SM1	Steering mirror	1" circular
SM2	Steering mirror	2" square
CM	Concave mirror	Spherical ($R = 4$ $[m]$)
M1, M2	Steering mirrors	1" circular
M3, M4	Scene beam mirrors	1" circular
M5, M6	Reference beam mirrors	1" circular
BS	Recombination beamsplitter	1" cube
PD	Amplified photodiode	Custom ($f_o = 80$ $[MHz]$)

Table 2.2: Optical components utilized in the schematic displayed in figure 2.7

A walkthrough of the optical schematic (figure 2.7) is as follows. The laser first interacts with the AOM. The AOM introduces the heterodyne beat signal, and functions as a Bragg cell of which we use the unmodulated 0^{th} and 80 MHz 1^{st} harmonic. The harmonic represents a small portion of the total power that passes through the AOM, so the 0^{th} order (scene) beam is the stronger of the two. The 80 MHz reference beam exits the the AOM at a narrow angle (13.9 $mrad$ for the Isomet 1205C-2), and is allowed to expand through mirrors $M1$ and $M2$ prior to being picked off by pickoff mirror $P1$. Mirrors $M5$ and $M6$ are used to align the reference beam perpendicular to the beamsplitter BS. Steering mirrors $SM1$ and $SM2$ are mounted on tripods which, dude to the availability of ConFlat ports, allow the alignment of the laser through the chamber at three discrete locations (figure 2.9), at an angle depicted in 2.8. The spherically-concave mirror CM, with a curvature radius of $R = 4\ m$, is used to send the beam back (at a narrow offset angle) and reverse the effects of the laser beam divergence. The radius of curvature defines the rough difference in path length that the that optical layout seeks to achieve [15]. As the scene beam travels through the chamber, the spatial difference introduced by the slightly offset return path is offset by the widened beam due to the laser's divergence angle. The scene beam is picked off by pickoff mirror $P2$, and mirrors $M3$ and $M4$ allow the beam to be aligned perpendicular to the beamsplitter. Finally, an amplified photodiode (described in section 2.4.1) picks up the interference signal.

2.3.1 For reference: Alignment procedure

Alignment is simple, since the optical layout is not relying on equal path lengths. Simply steer the beams through all their paths, and use a set of two irises in a typical fashion to align the single beamsplitter. Mirrors $M5$ and $M6$ are the two mirrors you need to set the final reference beam optical axis. This axis should be aligned with the beamsplitter BS in place. Finally, use mirror $M4$ and the beamsplitter itself (along with your two irises, though this diagnostic was implemented with only one) to align the scene beam onto the reference beam's optical axis. Increase the gain on the photodiode, move until you see a response on a oscilloscope (view it in X-Y display mode). Then, tweak the beamsplitter until you

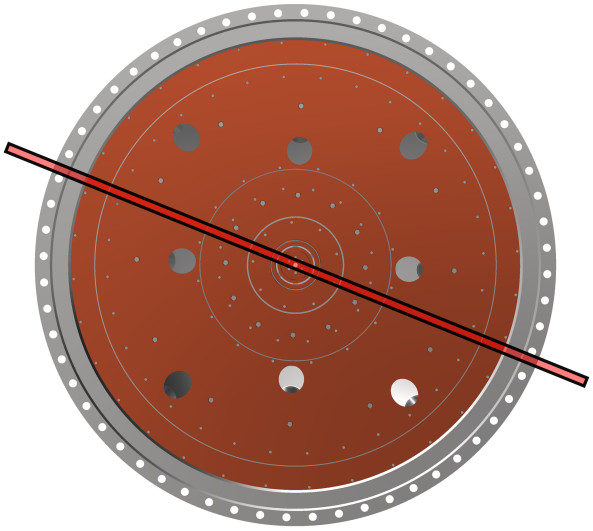

Figure 2.8: Transverse path of laser across gun face. The angle is dictated by the MOCHI vacuum chamber ConFlat ports.

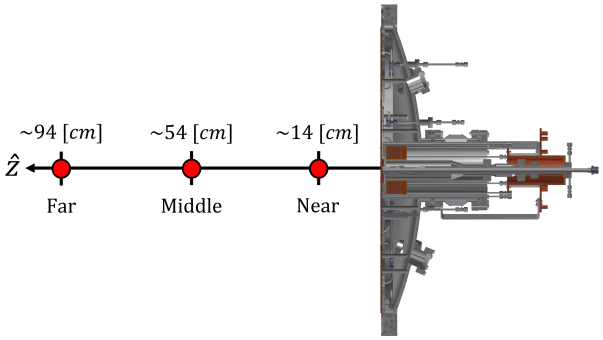

Figure 2.9: Distance of laser positions from gun face. There are three options perpendicular to the gun's $\hat{Z}$ axis: Near, Middle, and Far.

get a maximum radius on your Lissajous figure. Tweak the AOM angle until Lissajous is maximized. The gain was kept at $G = 0$ for the duration of the LabJet experiment to avoid noise pickup.

2.3.2 Heterodyne operation

Heterodyne operation refers to the superimposition of multiple frequencies in order to extract modulated information; a common technique used in FM radio [16]. In this interferometer, the AOM Bragg cell modulates the laser frequency by superimposing an 80 MHz harmonic frequency. The AOM driver produces the 80 MHz sinusoidal function that drives the AOM crystal; this function has a phase angle that is stationary in time. After interfering the scene and reference beams in the recombination beamsplitter (BS), the resulting interference

signal beats at the 80 MHz harmonic frequency. The changing index of refraction of the plasma or other phenomenon (vibrations, etc.) modulates the phase angle of the beating interference signal in time. The phase angle difference $\Delta\phi$ between the phase angle of the beating interference signal and the constant phase angle of the AOM driving frequency is produced by the quadrature mixer/splitter box and digitized. This is further discussed in section 2.4.2.

2.4 Associated electronics

Figure 2.10 portrays a schematic overview of the analog signal processing electronics that produce the output signals S_1 and S_2. The core of the signal processing is the quadrature mixer/splitter box (section 2.4.2), which takes the stationary 80 MHz AOM driver frequency and the time-varying interference signal (which beats at an imposed 80 MHz), and extracts the phase angle difference $\Delta\phi$ [16, 4, 10, 13]. The quadrature box receives these two inputs from the AOM driver itself, and the signal from an amplified photodiode (section 2.4.1).

The output signals from the electronics was digitized with a Tectronix TDS-2024B oscilloscope (2500 *samples* in total). A time resolution of 25 $\frac{\mu s}{div}$ was chosen because the next size down (10 $\frac{\mu s}{div}$) was too short of a total time window, and the next step up (50 $\frac{\mu s}{div}$) was unnecessarily long, sacrificing temporal resolution. So, with 2500 *samples* available over a 250 μs window, we have a sampling rate of 10 MHz. Therefore in-line, BNC, low-pass filters were selected at the oscilloscope Nyquist frequency (5 MHz).

2.4.1 Amplified photodiode

The amplified photodiode circuit is based off a chip designed by Professor Tom Mattick in 2004 for the ZaP flow Z-pinch experiment at the University of Washington [13, 7]. Figure 2.12 is a snippet of Dr. Mattick's original hard-drawn circuit diagram, and highlighted is the resonant LC band-pass filter that is used to select the frequencies which is amplified by $U2$, a variable-gain wide band amplifier. For the original hand-drawn circuit diagram, as well as a list of chips used, see appendix B.

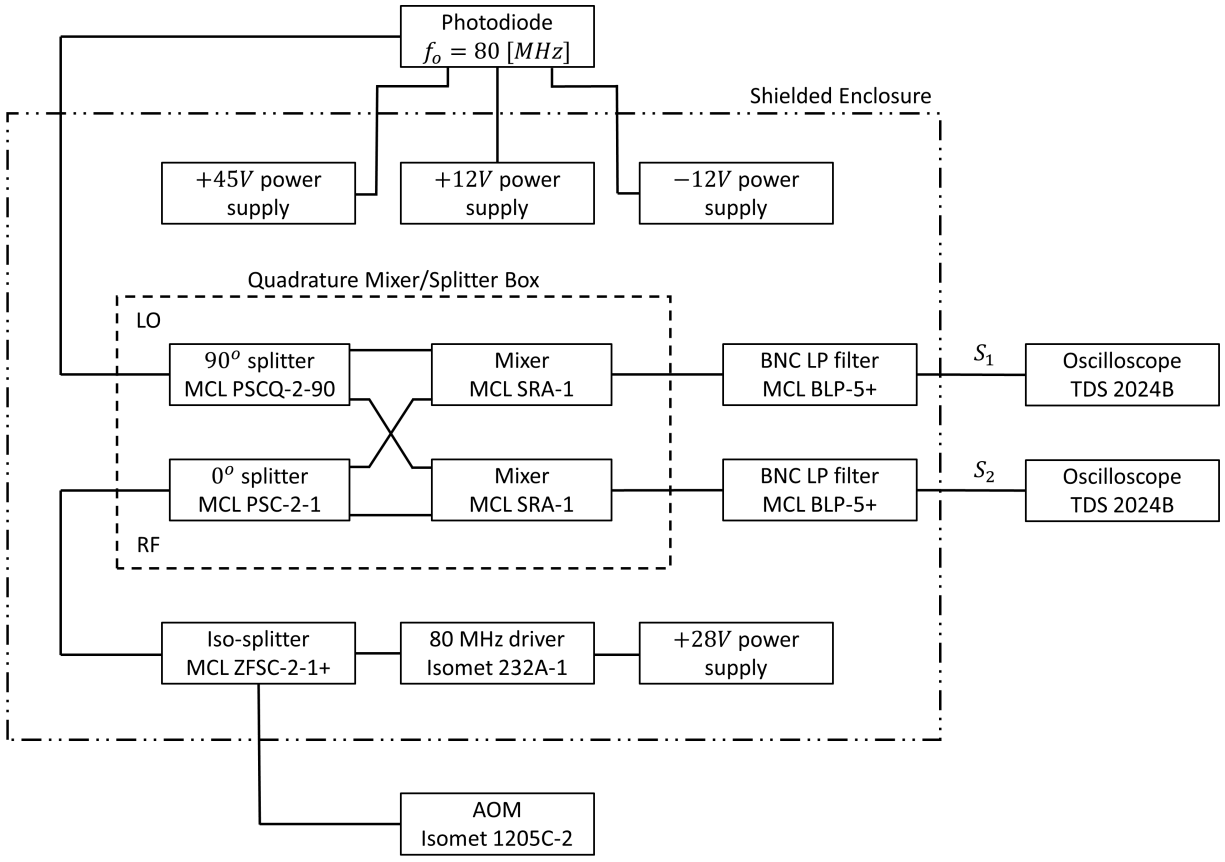

Figure 2.10: Signal processing electronics for the interferometer. Here the photodiode and AOM, and oscilloscope are located external to the shielded enclosure that houses the rest of the components

The amplifier's band-pass filter was modified to suited MOCHI's AOM frequency of 80 MHz (versus ZaP's original 40 MHz). Being a resonant band-pass filter, it can be characterized by a Q-factor. The Q-factor can be thought of as a ratio of the pass-band central frequency ω_r (defined in equation 2.15) to the pass-band bandwidth. Therefore, a lower Q filter would have a wider pass-band relative to its central frequency, and a high-Q filter would have a narrow pass-band. Desired Q factors can be selected by selecting a value for the inductor L_1 according to equation 2.16. In equation 2.16, the frequency ω_r and resistance R_p are both constant ($\omega_r = 2\pi(80\ MHz)$ and $R_p = 50\ \Omega$). With a L_1 value chosen, equation 2.15 can be solved for the capacitor value C_5 (see table 2.3 for corresponding L_1 and C_5 surface-mount chip values).

The filter response of three Q-factor options is seen in figure 2.11. Note that in this plot the gain (ordinate) is normalized to 1 to make the filter shape more evident. In application, the area under the curve (gain) is conserved so the high-Q filter would have a much larger peak than the low-Q filter, with the med-Q curve in between the two.

During the debugging process, two amplifier chips were produced. The amplifier chip is a small, $\sim 2" \times 1"$, double-sided surface-mount PCB, and can be seen in figure 2.15. The first chip produced was hand-populated, and used the low-Q option, the second was professionally-populated using the high-Q option. The high-Q option was found to be unstable, so the original low-Q option was used for the diagnostic. The photodiode is reverse-biased at 45 V, fed by a power supply located in the electronics box, and the amplifier is powered by $\pm 12\ V$ rails, also fed by two power supplies in the electronics box.

$$\omega_r = \frac{1}{\sqrt{L_1 C_5}} \tag{2.15}$$

$$Q = \frac{R_p}{\omega_r L_1} \propto \frac{1}{L_1} \tag{2.16}$$

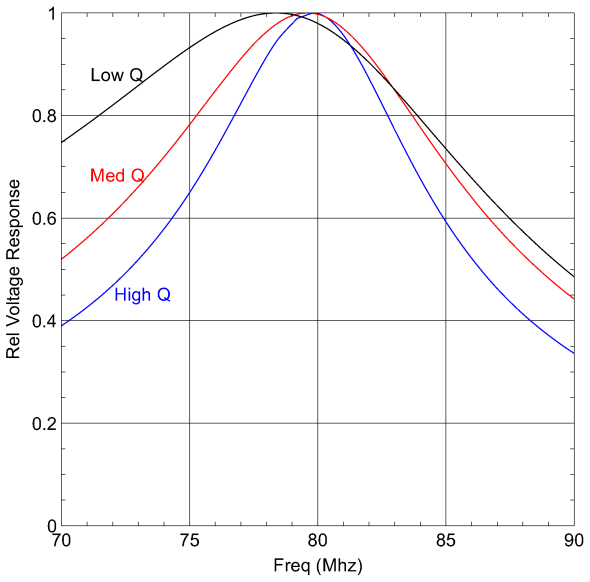

Figure 2.11: Plot of Q for different amplifier notch filters. Plot courtesy of Dr. Tom Mattick.

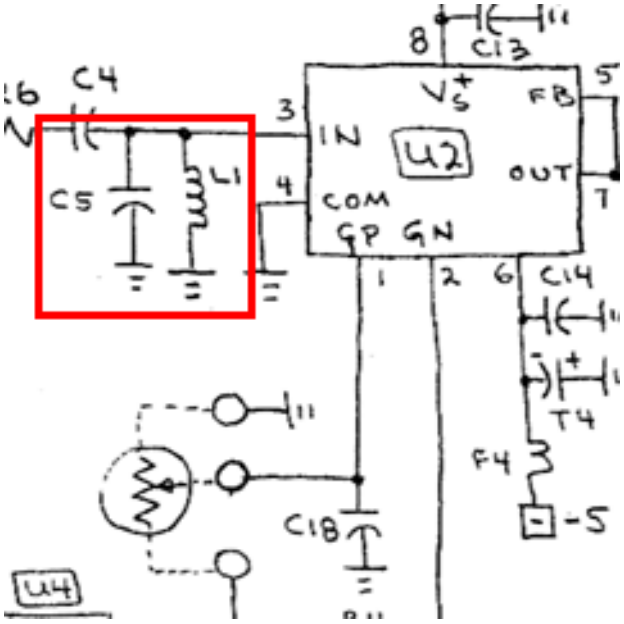

Figure 2.12: Notch filter circuit diagram. Circuit diagram courtesy of Dr. Tom Mattick (see appendix B.

	L1 [nH]	**C5 [pF]**
Low Q	20	200
Med Q	14	280
High Q	10	390

Table 2.3: Notch filter inductance and capacitance values. Corresponds to plot 2.11.

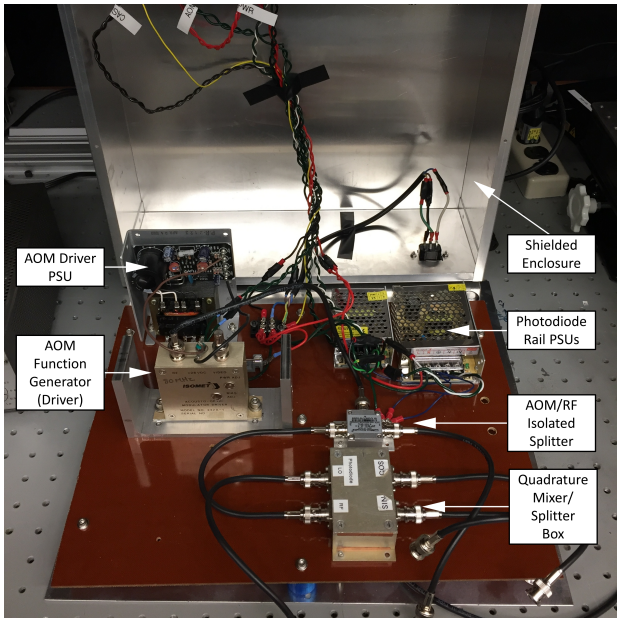

Figure 2.13: Picture of the inside of the interferometer electronics box. The labeled components are discussed in section 2.4.

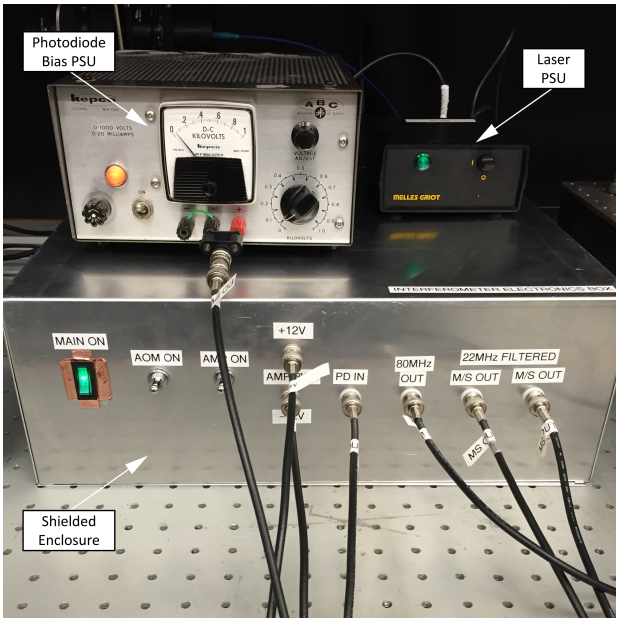

Figure 2.14: Picture of electronics box exterior. Note that this was before the final 45 V power supply was installed, so the bench supply up top is providing the 45 V required by the photodiode.

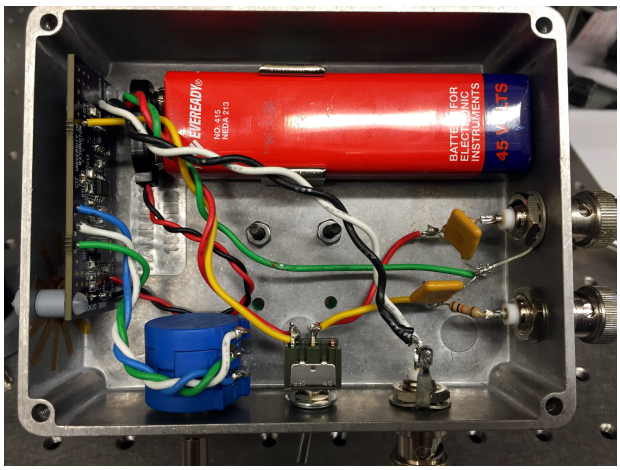

Figure 2.15: Picture of amplified photodiode internals. Note that the 45V battery has been replaced with a 45V power supply.

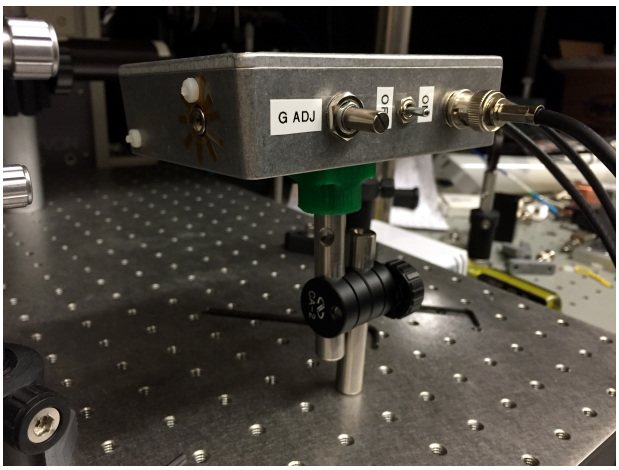

Figure 2.16: Picture of amplified photodiode on the optical table. The gain dial was left at minimum during experimentation to avoid noise pickup.

2.4.2 Quadrature mixer/splitter

The quadrature mixer/splitter box is another modified design from an existing ZaP component [10, 13, 7]. The 90^o splitter is the only narrowband component (the 0^o splitter, and two mixers were both broadband), and therefore was the only component that needed to be altered to accommodate the new 80 MHz central frequency. The Radio Frequency (RF) input is the 80 MHz AOM driver frequency, which is stationary in relative phase. The AOM driver signal is split to both the quadrature mixer/splitter box, as well as the AOM itself. The Isomet AOM driver supplied a signal strong enough that the diagnostic worked without the need for amplification after splitting. The Local Oscillator (LO) input is the signal from the photodiode, which varies in time with the changing index of refraction of the plasma. The quadrature mixer/splitter box is where these two are combined in order to extract the phase angle difference $\Delta\phi$.

The output from the quadrature mixer/splitter box is signals S_1 and S_2, seen in their full output form as equations 2.17 and 2.18 [13, 7]. In this equation, A_s and A_r are the amplitudes of the scene and reference beams, and A_b is the amplitude of the 80 MHz AOM driving (beat) frequency ω_b.

$$S_1 = \frac{1}{8}(A_s^2 + A_r^2)A_b \cos\omega_b t + \frac{1}{8}A_s A_r A_b\{\cos[\Delta\phi(t)] + \cos[2\omega_b t + \Delta\phi(t)]\} \tag{2.17}$$

$$S_2 = \frac{1}{8}(A_s^2 + A_r^2)A_b \cos\omega_b t + \frac{1}{8}A_s A_r A_b\{\sin[\Delta\phi(t)] + \cos[2\omega_b t + \Delta\phi(t)]\} \tag{2.18}$$

After filtering using the 5 MHz BNC low-pass filters, the terms that contain the high frequency ω_b are cut out. After making the substitution for the Lissajous radius $R = \frac{1}{8}A_s A_r A_b$, we arrive at the final signals S_1 and S_2 that are digitized by the TDS-2024B oscilloscope (equations 2.19 and 2.20). In this equation A and B are DC-level constants which arise as a undesired by-product of the system as a whole.

$$S_1 = R\cos\left[\Delta\phi(t)\right] + A \tag{2.19}$$

$$S_2 = R\sin\left[\Delta\phi(t)\right] + B. \tag{2.20}$$

2.5 Lissajous figure indicates proper operation

The digitized outputs are S_1 and S_2 (equations 2.19 and 2.20). By blocking the scene beam, we can measure the DC-offsets A and B, subtract them, and plot the the $\cos\Delta\phi$ against the $\sin\Delta\phi$. This is known as a Lissajous figure, and intuitively it is a 'unit circle' representation of the phase angle difference between the scene and reference arms of the interferometer at any point in time. Since maximum radius means maximum interference, it is used both as an alignment tool as well as a overall figure of merit.

Figure 2.17 is an example of a working Lissajous ($R =\sim 50\ mV$) figure under idle operation. The change in phase angle difference $\Delta\phi$ is due to the the background noise in the form of vibrations, air currents in the room altering the index of refraction, or expansion and contraction of mirror surfaces from heating [10]. The time scale of this systematic noise is on the order of 1.6 ms. Therefore, over the 100 μs plasma shot duration (described in chapter 1) the background vibrational, etc., noise will be linear.

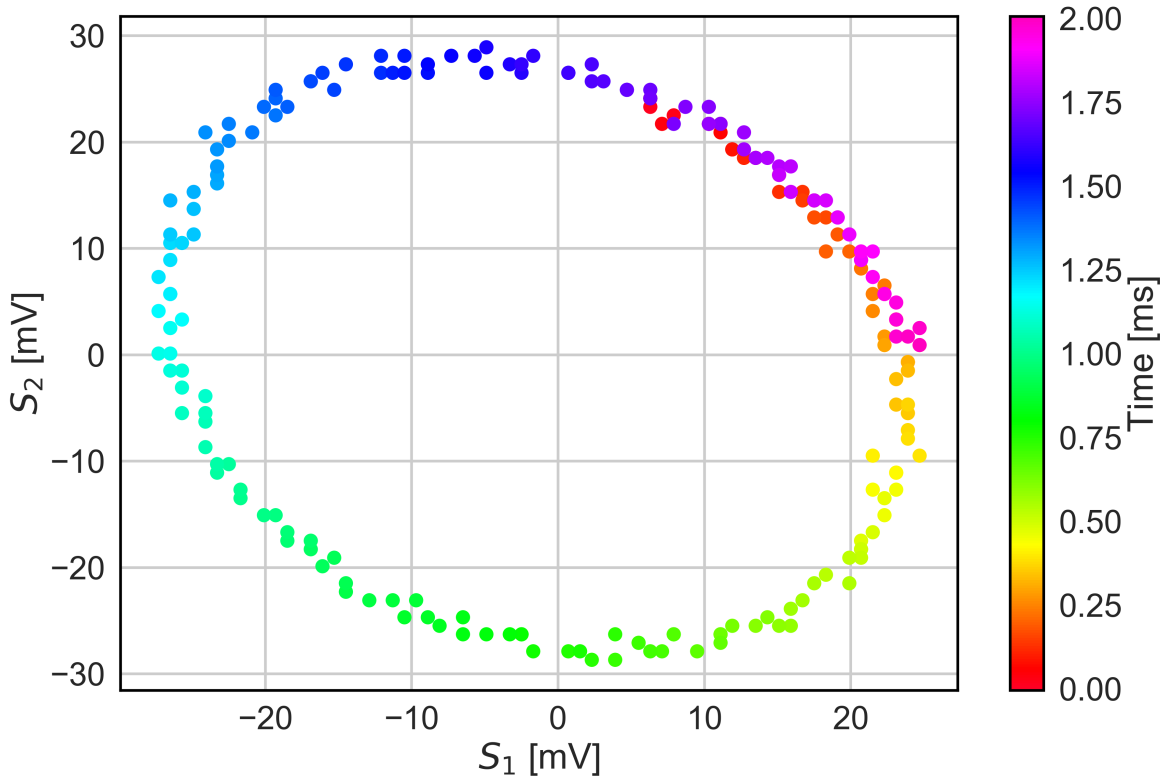

Figure 2.17: Idle interferometer Lissajous figure. Amplifier gain is set to $G = 1$, which results in ~ 25 $[mV]$ radius. From this plot we can infer a vibration timescale of ~ 1.6 $[ms]$, or 625 $[Hz]$.

Chapter 3

ELECTRON DENSITY MEASUREMENTS

3.1 Computational analysis

The S_1 and S_2 signals digitized using a *Tectronix TDS 2024B* oscilloscope, which features dynamic interplay between sample domain and the available limit of $2500 samples$. The oscilloscope was set to digitize at 10 MHz, resulting in a 250 μs total window. The oscilloscope was triggered with a optical-to-TTL box built in-house, which has a sub-microsecond rise time following a received optical pulse [6].

The remainder of this section is the data analysis procedure used to obtain the line-integrated electron density $\overline{n}_e$ for a given plasma discharge. In the analysis, shot #6994 was used: a typical representative plasma shot. The code for this analysis can be found in appendix C.

3.1.1 Noise reduction and Lissajous analysis

The output of the interferometer electronics box is two signal signals, S_1 and S_2, which are defined in equations 2.19 and 2.20. The first step in processing this data is to remove the constant DC-offset voltages. This is done by manually blocking the scene branch of the interferometer in order to kill interference, then digitize the resulting flat-line signal on the scope. By taking the mean of the available $2500 samples$ we get an accurate reading of the DC-offset for each signal, and this is simply subtracted, resulting in figure 3.1.

With the raw signals now available it becomes possible to use shot #6994's Lissajous figure, which is a unit circle representation of the phase angle difference ($\Delta\phi$) of the plasma, to further process the data. Due to the noise susceptibility of the diagnostic, there is often a variance in signal amplitudes R, which simultaneously is radius of the Lissajous figure.

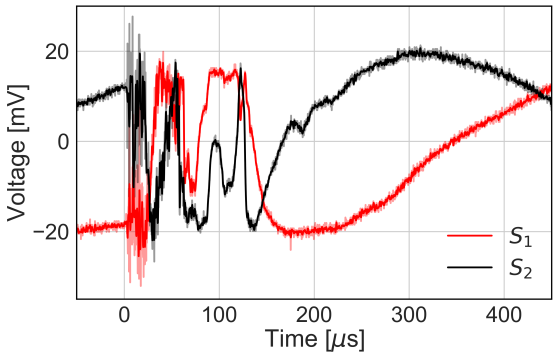

Figure 3.1: This plot presents the raw signals, both filtered and unfiltered, output from the interferometer electronics box detailed in chapter 2. The signals already have the DC-offsets removed. $S_1 = R\cos\Delta\phi$ and $S_2 = R\sin\Delta\phi$. The filtered signal (seen as solid) is the result of a convolution of the unfiltered signal (seen as transparent) with a 750 [kHz], 5th-order butterworth filter.

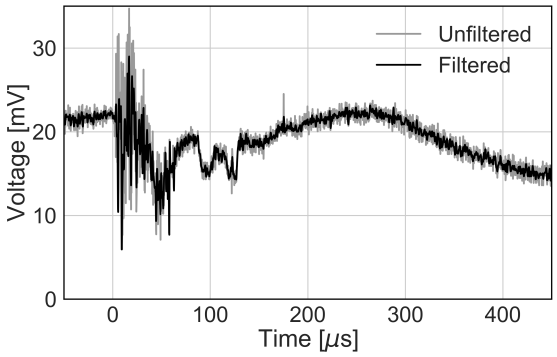

Figure 3.2: The Lissajous figure radius for shot #6994. The filtered signal (seen as solid) is the result of a numerical convolution (completed using Python) of the unfiltered signal (seen as transparent) with a 750 [kHz], 5th-order butterworth filter.

The noise pickup can cause the signal amplitude to jump in such a way that the radius of the Lissajous figure reduces to zero or below (which would be a positive radius in the opposing quadrant). This effect manifests as an instantaneous jumps in the phase angle of the Lissajous figure. In order to to prevent this, a 5th-order butterworth filter is used to filter the two signals, the frequency of which is determined by a iterative while loop. This loop iterates on the filter frequency while tracking the radius of the Lissajous figure, further decreasing the frequency until the Lissajous radius stays within some predetermined value (3 [mV] for shot #6994). Figure 3.1 is the result of the iterative filtering: the comparison between filtered and unfiltered raw signal outputs for shot #6994. Figure 3.2 is similar,

displaying the filtered and unfiltered Lissajous radius.

There is a small chance that the jump in the Lissajous figure could be so large, that two corresponding points in opposite quadrants could both have a radius value $R > 3$. In order to confirm that the noise filtering has been successful and will result in a correct $\Delta\phi$, we need to visually make sure that the filtered Lissajous does not move across this $R = 0$ boundary. Figure 3.3 is the filtered Lissajous figure overlaid atop the unfiltered points. It is clear that the Lissajous figure does not cross the $R = 0$ boundary, as thus will result in a correct $\Delta\phi$ measurement.

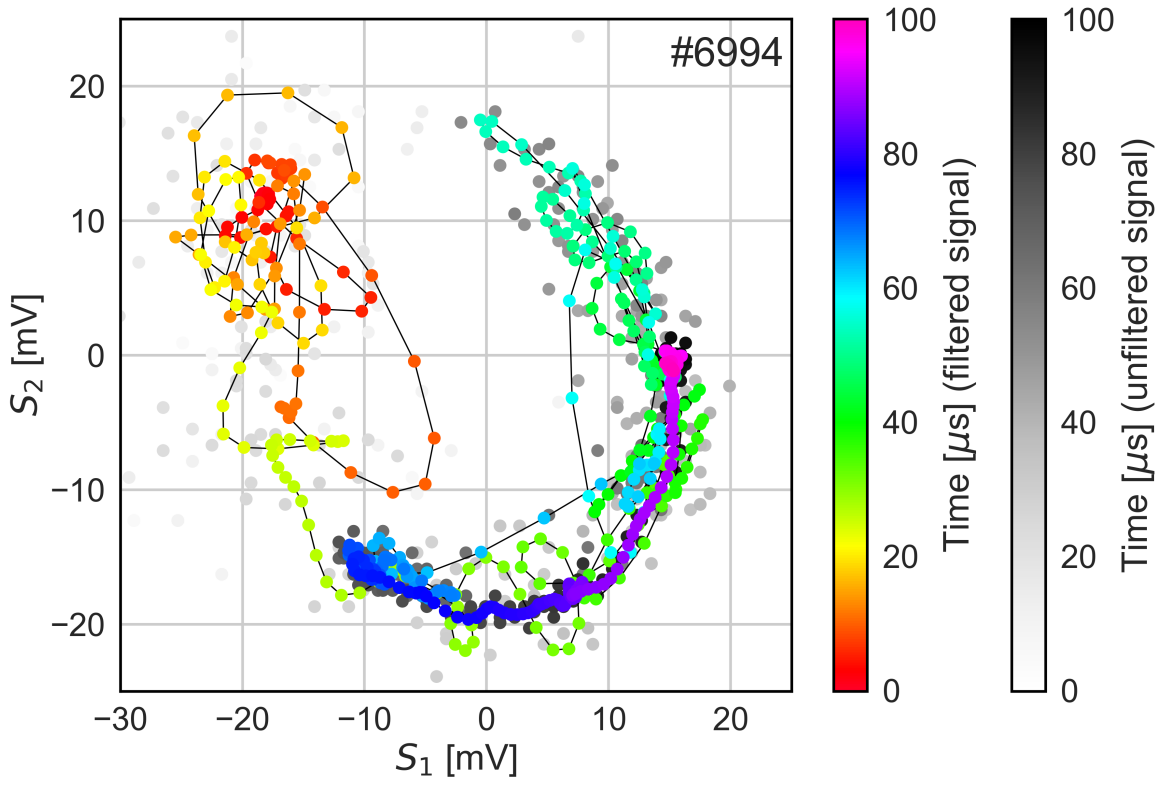

Figure 3.3: This is the Lissajous figure for shot #6994. This can be thought of as a unit circle tracking the phase angle difference $\Delta\phi$ in time. Notice how the radius does not cross the $R = 0$ boundary.

3.1.2 Obtaining electron density from raw data

Once the data filtering is complete, we can extract the phase angle difference $\Delta\phi$ from the quadrature outputs S_1 and S_2. While the equation utilized is a simple trigonometric relationship (equation 3.1), there are two major obstacles that must be overcome before the $\Delta\phi$ that will be used in 2.14 is obtained: arctan asymptotes, and the initial $\Delta\phi$ offset.

$$\Delta\phi = \arctan\frac{S_2}{S_1} \tag{3.1}$$

In order to avoid the arctan asymptotes, the Python function `numpy.arctan2`, which is designed to track the quadrant of the angle and provide correct boundary solutions at $[\frac{\pi}{2},\ \frac{-\pi}{2}]$, is utilized. The output of `numpy.arctan2()` is seen in figure 3.4. This function is defined in the range $[-\pi,\ \pi]$ and calculates the $\Delta\phi$ angle with a positive sign in quadrants I and II, and with a negative sign in quadrants III and IV resulting in a instantaneous jump of 2π across the *pi* boundary. To adjust for this, we add 2π to data points located in quadrants III and IV, which means simply whenever the value of the sine data trace (S_2) is negative. This produces the positive, absolute $\Delta\phi$ angle over a full unit circle range $[0,\ 2\pi]$, shown in figure 3.5.

As seen in figure 3.5, there are still 2π jumps in phase angle that occur at the $0,\ 2\pi$ boundary. These are defined as fringe jumps. To remove fringe jumps, we first set a conservative limit of π to the difference between any two adjacent points. Then, if a point jumps beyond a difference of π, the two points are subtracted and depending on the sign, a value of 1 is added or subtracted from an integer from an array. This integer array is effectively tracking what transit the unit circle is on as the phase angle increases or decreases. If a point changes by a value larger than π relative to the previous, we say that it is due to a fringe jump and add/remove 2π accordingly. The result is the $\Delta\phi$ that is jump-adjusted relative to the starting value. This is seen as the 'Initial' trace in figure 3.6.

From figure 2.17, we infer that the timescale of vibration is on the order of $\sim 1\ [ms]$. In comparison, the region of interest during a typical plasma shot is $\sim 100\ [\mu s]$. Therefore

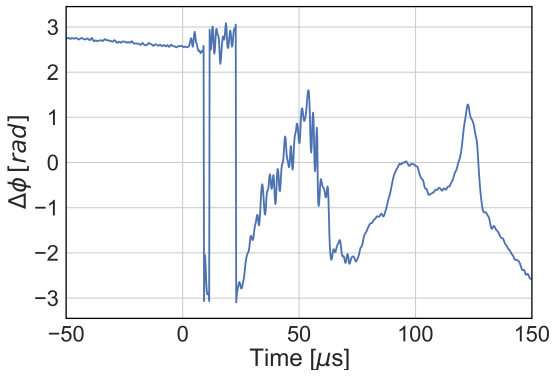

Figure 3.4: The raw $\Delta\phi$ output from `numpy.arctan2()`. The Python function `numpy.arctan2()` is defined in the range $[-\pi,\ \pi]$, which is evident from the 2π jumps at those locations.

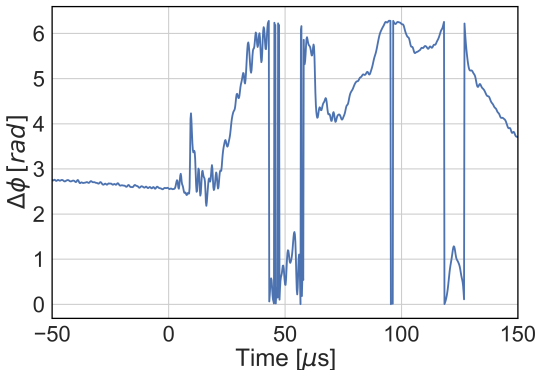

Figure 3.5: $\Delta\phi$ after being adjusted for the range that `numpy.arctan2()` imposes. $\Delta\phi$ is now defined in the range $[0,\ 2\pi]$, which is evident from the 2π jumps located at those locations.

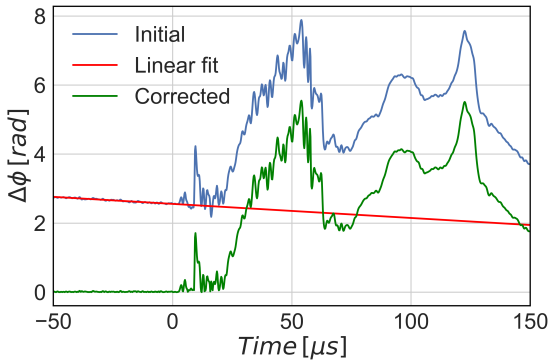

Figure 3.6: Here we see the true $\Delta\phi$, the linear fit used to correct for the initial offset, and the final $\Delta\phi$ that will be used to produce $\overline{n}_e$. We assume that the background noise is linear over the time domain shown.

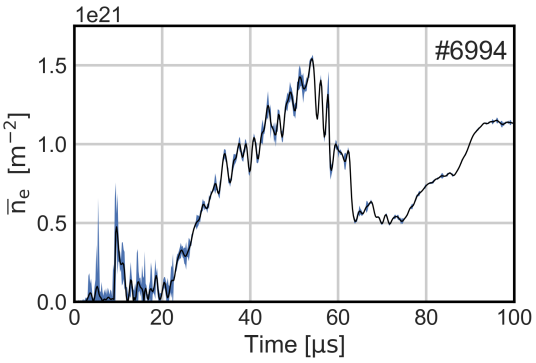

Figure 3.7: The final plot of $\overline{n}_e$ for shot #6994. Note the increase in SNR over time.

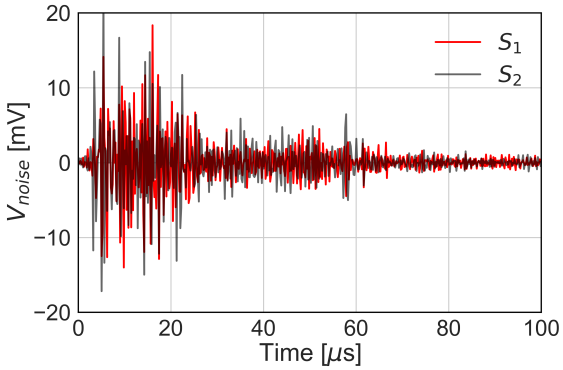

Figure 3.8: The result of subtracting the filtered data from the unfiltered data. We see that the noisiest period is the first 20 μs, a typical feature of every shot

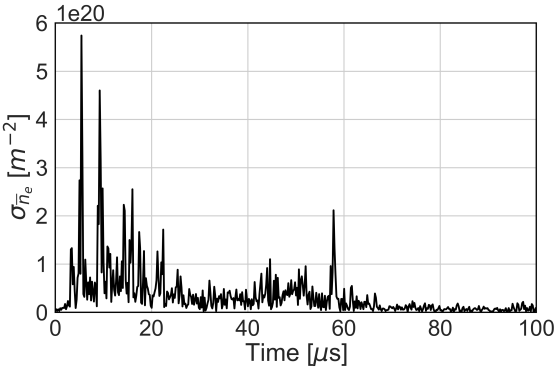

Figure 3.9: Time-dependent standard deviation of $\overline{n}_e$ for shot #6994

the assumption is made that the variation in the the phase angle difference $\Delta\phi$ due to background vibration follows a linear relationship over the shot duration. A period of 50 [μs] is digitized before experiment zero in order to determine the background linear trend, and this is subtracted off of $\Delta\phi$. This subtraction is depicted in figure 3.6.

With the final $\Delta\phi$ measurement obtained, it is simply a matter of a calibration factor to go from $\Delta\phi$ to $\overline{n}_e$. We utilize equation 2.14 to arrive at the line-integrated electron density measurement, seen in figure 3.7.

3.1.3 Error analysis

The error in the line-integrated density measurement $\overline{n}_e$ arises from the uncertainty in the two digitized signals S_1 and S_2. The equation utilized to produce $\Delta\phi$ from the two raw signals is defined in equation 3.1, and equation 2.14 represents the conversion between $\Delta\phi$ and $\overline{n}_e$. The error propagation is seen in equation 3.2, where the partial derivatives of each uncertainty source are weighted by their uncertainty and added in quadrature. The final

equation for the standard deviation of the line integrated density $\sigma_{\overline{n}_e}$ is seen in equation 3.4.

$$\sigma_{\Delta\phi}^2 = \left[\frac{\partial(\Delta\phi)}{\partial S_1}\sigma_{S_1}\right]^2 + \left[\frac{\partial(\Delta\phi)}{\partial S_2}\sigma_{S_2}\right]^2 \tag{3.2}$$

$$\sigma_{\Delta\phi} = \sqrt{\left[-\frac{S_2}{S_1^2+S_2^2}\sigma_{S_1}\right]^2 + \left[\frac{S_1}{S_1^2+S_2^2}\sigma_{S_2}\right]^2} \tag{3.3}$$

$$\sigma_{\overline{n}_e} = 2.78x10^{20}\sigma_{\Delta\phi} \ \ [m^{-2}] \tag{3.4}$$

The two uncertainties in S_1 and S_2 (σ_{S_1} and σ_{S_2}) are obtained from the noise directly. By subtracting the filtered signals from the unfiltered signals, we obtain figure 3.8. This figure is typical for every shot: we find that the noisiest sections occurs consistently within the $0-20$ $[\mu s]$ window following main bank switching (5 μs), and it overlaps the period when the plasma first breaks down, which is likely one of the sources of such excessive noise. If we assume that the time-dependent uncertainties is directly this noise measurement, we can insert the array into equations 3.3 and 3.4 to arrive at figure 3.9, the time-dependent standard deviation of $\overline{n}_e$. The $\overline{n}_e$ line-integrated electron density measurement, plotted with errorbars, can be seen in figure 3.7. Here, higher uncertainties are prevalent in the first 20 μs of the plasma shot, decreasing in time, and achieve a high signal-to-noise ratio.

3.2 First Operational Campaign

The first operational campaign lasted from August to November 2016, and was marked by the final commissioning the LabJet gun. Up until this point there had been consistent arcing between the middle and outer electrodes preventing jet formation by drawing available current away from the plasma formation. The arcing was fixed using a $\frac{1}{16}$" sheet of PTFE Teflon plastic which protruded out from the electrodes by ~ 1 $[cm]$ (section 3.2.2). For this first campaign, basic diagnostics were online alongside the interferometer: fast voltage probes purposed to measure the two gun voltages, rogowski coils purposed to independently measure the two gun currents, a Pearson monitor purposed to measure the bias field coil

current, and the Kirana camera purposed to observed light emission from the plasma. Only hydrogen was used, and the interferometer laser was located at the *Near* position ($\sim 14\ cm$, figure 2.9).

During this operational campaign the interferometer also reached its final commissioning stage. The issues overcome were mainly related to excess noise in the system as well as improper triggering of the oscilloscope, and it was determined that these issues were in fact related. Initially he diagnostic was triggered off itself, so as to save NI timing channels, but the sensitivity to noise was causing premature pick up, and oscilloscope was triggering early. The solution was to obtain an optical-to-TTL triggerbox [6], and use a NI triggering channel. Another issue was that the interferometer signals would swing on the same timescale as the gun currents. This appeared to be a result of the rising common ground of the LabJet gun. The solution was re-working LabJet's grounding scheme and an effort to minimize the noise within the diagnostic itself: making a twisted pair out of the S_1 and S_2 BNC cables themselves.

Shot #6580 represents a typical shot from this operational campaign. The density, Lissajous, and Kirana imagery for #6580 is seen in figures 3.10 - 3.12. The experimental parameters were set as follows: he core gun was fired at 4 kV, the skin gun at 4.6 kV, the bias at 173 V, and all enabled valves at 1.1 kV. The banks were fired at $t = 0\ s$, and defines the experiment zero of the plasma discharge. The bias coil was fired at $-4.25\ ms$, the outer-outer gas valves at $-4\ ms$, the middle valve at $-6\ ms$, and the inner valve at $-7\ ms$. The outer-inner valves were not enabled. The Lissajous was numerically 5th-order butterworth filtered at 250 kHz.

In figure 3.10, we see the Kirana camera images taken during shot #6580. The early section of this shot ($\sim 0 - 20\ [\mu s]$) is representative of typical planar plasma gun operation, where a jet forms, kinks, and breaks off (section 3.2.1 [27, 3, 17]. However, because our main bank PSUs have a quarter-cycle discharge period of $\sim 90\ [\mu s]$, peaking at $\sim 40\ [\mu s]$ (figure 1.7), there is still current available to drive plasma dynamics. Beginning in frame 6 (figure 3.10), we see that diffuse plasma 'spray' occurs, but does not collimate, which has a line

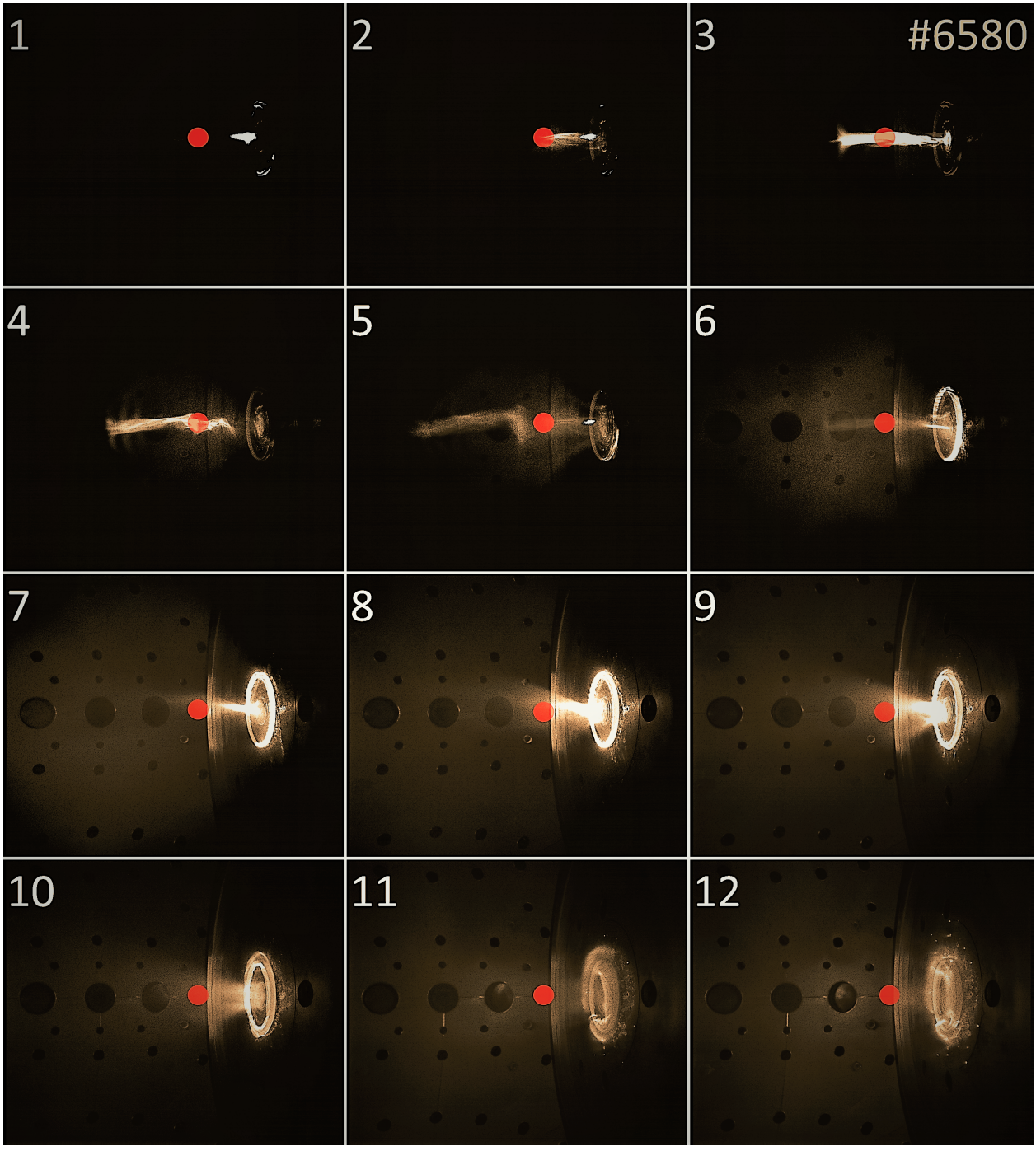

Figure 3.10: Frames taken from the Kirana video for shot #6580.

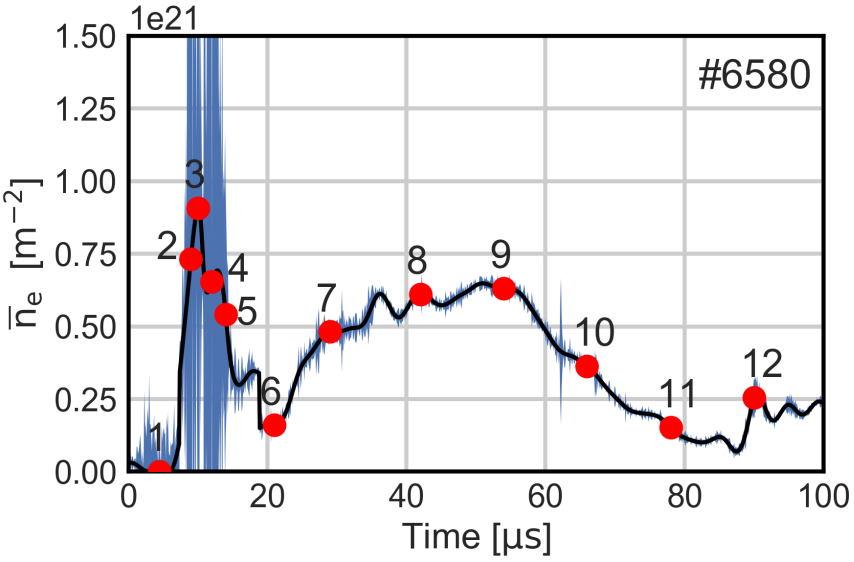

Figure 3.11: Line integrated density plot for shot #6580.

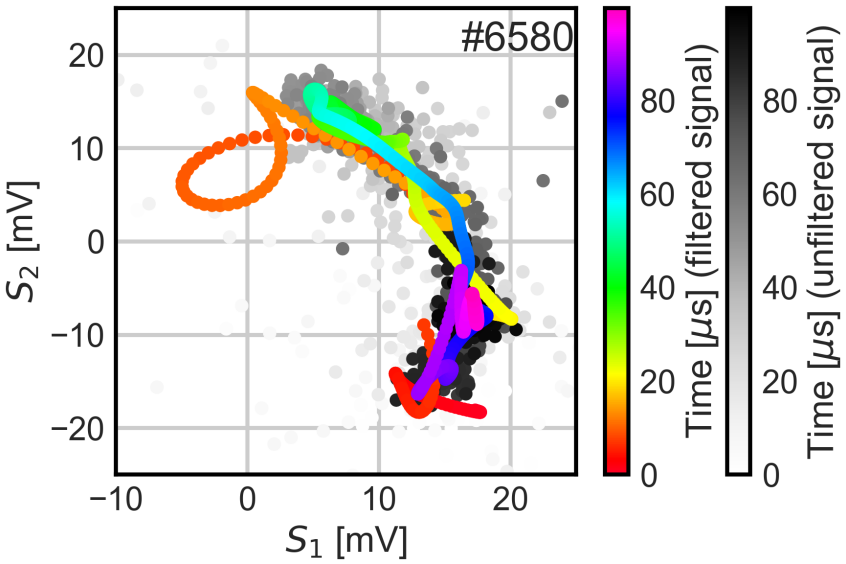

Figure 3.12: Lissajous figure produced over the course of shot #6580.

integrated density of $\sim 6x10^{20}$ $[m^{-2}]$. From frames $6-12$, we see that the Teflon insulator is a source from a secondary formation: a small bundt-cake-like plasma formation which links the middle to outer electrode. Note that this shot in particular had excessively large error bars. This secondary formation is initially tight around the Teflon insulator, but gradually expands in frames $10-12$, and creates a small ejection in the last frame (picked up in the 12^{th} frame in figure 3.11). Shortly following this observation, the first operational campaign was ended in order to implement the alumina end cap solution (section 3.2.2).

3.2.1 Interpretation of first campaign jet formation

The LabJet plasma gun operation is summarized in the overview seen in figure 3.13. This process of plasma breakdown, collimation, lengthening, kinking, and breaking is typical to planar plasma guns [27, 3, 17].

An experimental sequence is as follows. Panel 1 (figure 3.13) shows the vacuum magnetic field generated by firing the bias PSU through the bias field coil. This occurs $\sim 5-20$ ms before the main bank PSUs (which mark experiment zero). Next the fast gas valves are fired, which creates the initial condition of neutral density seen in panel 2 [6]. This typically occurs $\sim 1-10$ ms prior to experiment zero. Panel 3 represents the plasma breakdown that occurs $\sim 1-5$ μs after firing the main banks. The breakdown occurs along the bias field lines that are designed to link the two plasma guns. This which forms two azimuthally symmetric, nested 'bundt cake' plasma formations [6]. A single bundt cake formation is similar to the 'spider leg' formation that previous two-electrode planar plasma guns formed with discrete gas injection [27, 3], with the difference being azimuthally symmetric breakdown versus discrete. The symmetric, current-carrying bundt cake formation attracts to itself, narrows in the center, and begins the collimation phase of the jet, seen in panel 4 [27]. Azimuthally symmetric $J \times B$ forces act to further extend and collimate the jet (panel 5), increasing the jet aspect ratio. Eventually the jet extends far enough along the $\hat{Z}$ axis that it becomes susceptible to a kink instability [23, 25] which causes the jet to break, seen in panel 6. The broken jet propagates downstream as a detached plasmoid.

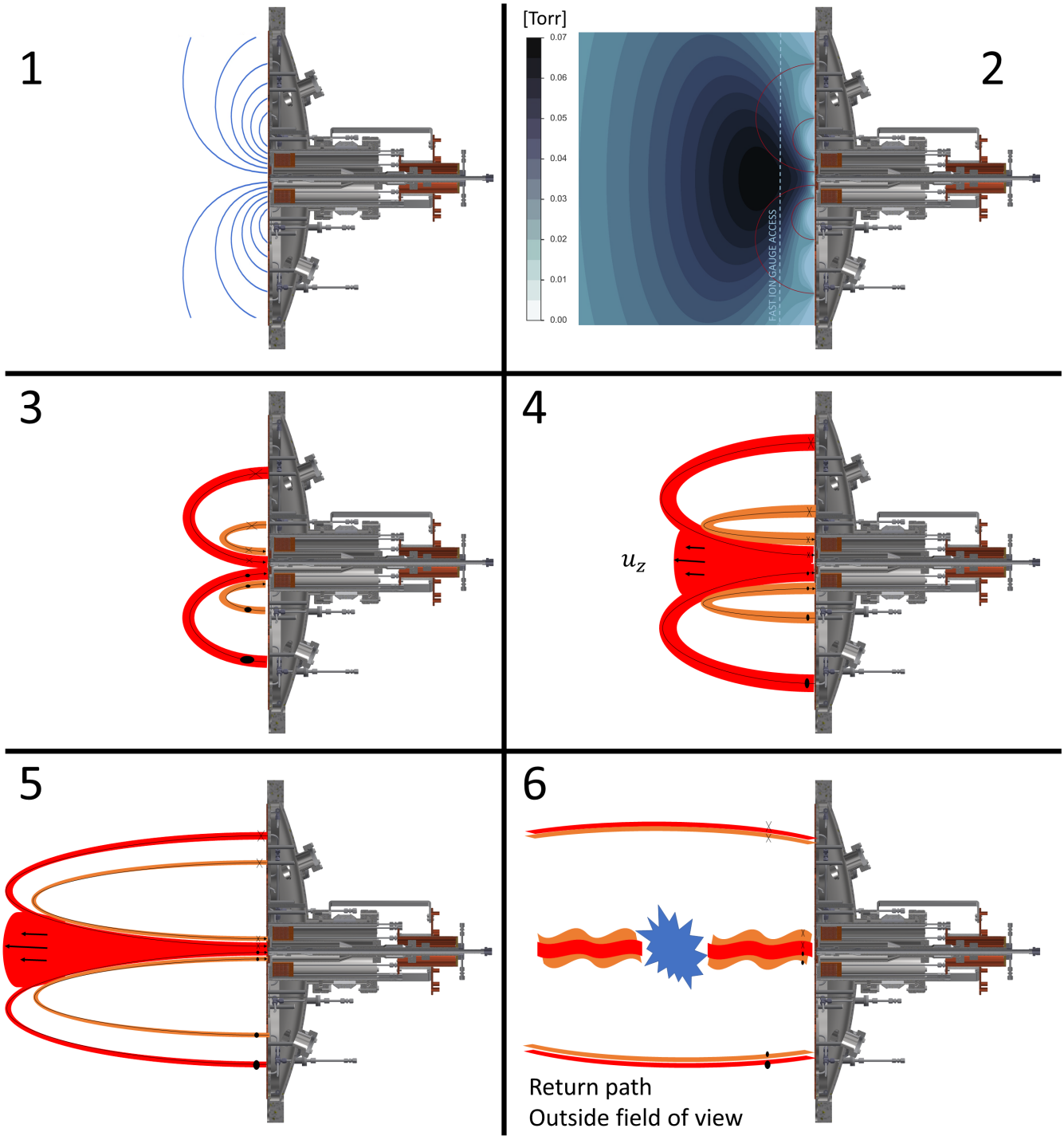

Figure 3.13: Step-by-step cartoon schematic of LabJet gun operation

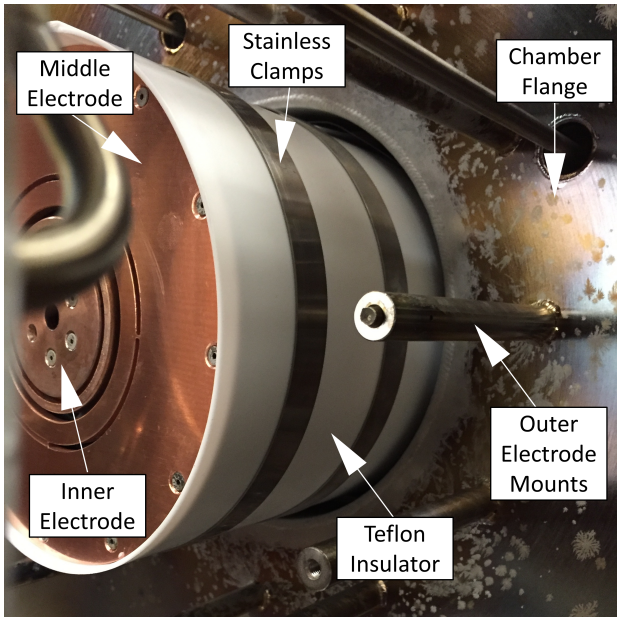

Figure 3.14: Image of Teflon wrapped around the middle electrode assembly.

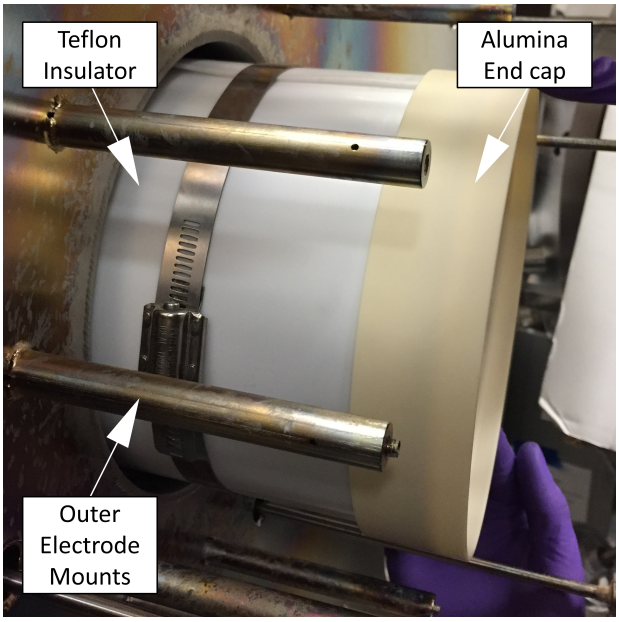

Figure 3.15: Image of Teflon wrap with Alumina insulator end cap

3.2.2 Electrode insulation

The LabJet gun electrodes were designed with an 8 mm (radial) gap purposed to insulate both the inner from the middle potentials, and the middle from the outer (common) potentials. During its commissioning phase the LabJet gun experienced issues with undesired arcing across the insulating gap between the middle and outer electrodes. The inner and middle electrode gap did not experience the same arcing due to the minimal potential difference between the two electrodes with respect to the middle-outer difference; it was found that even in situations where one of the two electrodes was not energized, it would still swing to a comparable potential.

The initial unsuccessful effort to fix the arcing took the form of shortening the insulating gap so as to access the lower Pressure x Distance (PD) region of the Pascal curve, where small changes in PD causes a large jump in requred breakdown voltage for a given pressure

[9, 2, 6]. The first successful insulation technique, shown in figure 3.14, was a sheet of PTFE Teflon plastic was wrapped around the middle electrode assembly, protruding out of the insulating gap by about 1 cm. This allowed for the first fully-operational campaign, which lasted from August to November 2016.

An upgrade to the Teflon insulator occurred between the first and second operational campaigns. The Teflon was pushed back behind the lip of the middle electrode, and a alumina end cap replaced the Teflon as the protrusion piece (seen in figure 3.15). The alumina extends far enough back behind the electrode such that the Teflon does not experience regions of high electric field. The insulating end cap drawing can be found in appendix B. This proved to be the final fix, allowing for the second, and third operation campaigns.

3.3 Second Operational Campaign

The second operational campaign lasted from December 2016 to February 2017 and is marked by the LabJet gun entering its final configuration. In an attempt to remove the secondary plasma formation seen in shot #6580 (first operational campaign), PTFE Teflon insulator was bolstered by an alumina HV insulator (see section 3.2.2). As intended, the Teflon-based plasma formation was removed and did not sap any available current. Since the arcing was still prevented by the alumina end cap, the entirety of the gun current was channeled into the plasma dynamics. In all second campaign shots, a new plasma formation is seen: a highly stable, highly collimated long-duration plasma jet formation ("long" jet).

An updated shot sequence overview is seen in figure 3.25. Panels 7 and 8 (figure 3.13) depict a new 'long jet' formation; a formation unique to the LabJet's triple electrode, azimuthally-symmetric gas-injected planar gun design. Following the short, initial jet going kink-unstable and breaking off, a secondary jet collimates (panel 7) and extends outward along the $\hat{Z}$ axis into the detached plasmoid left behind from the initial, kink-unstable jet (panel 8). As evident by the Kirana camera images, this jet is highly rotational screw pinch, and extends the entire available chamber length (1.1 m), even reflecting off the Spheromak-Gun on the opposite end of the chamber. This lasts from $\sim 40-80$ μs, which corresponds to

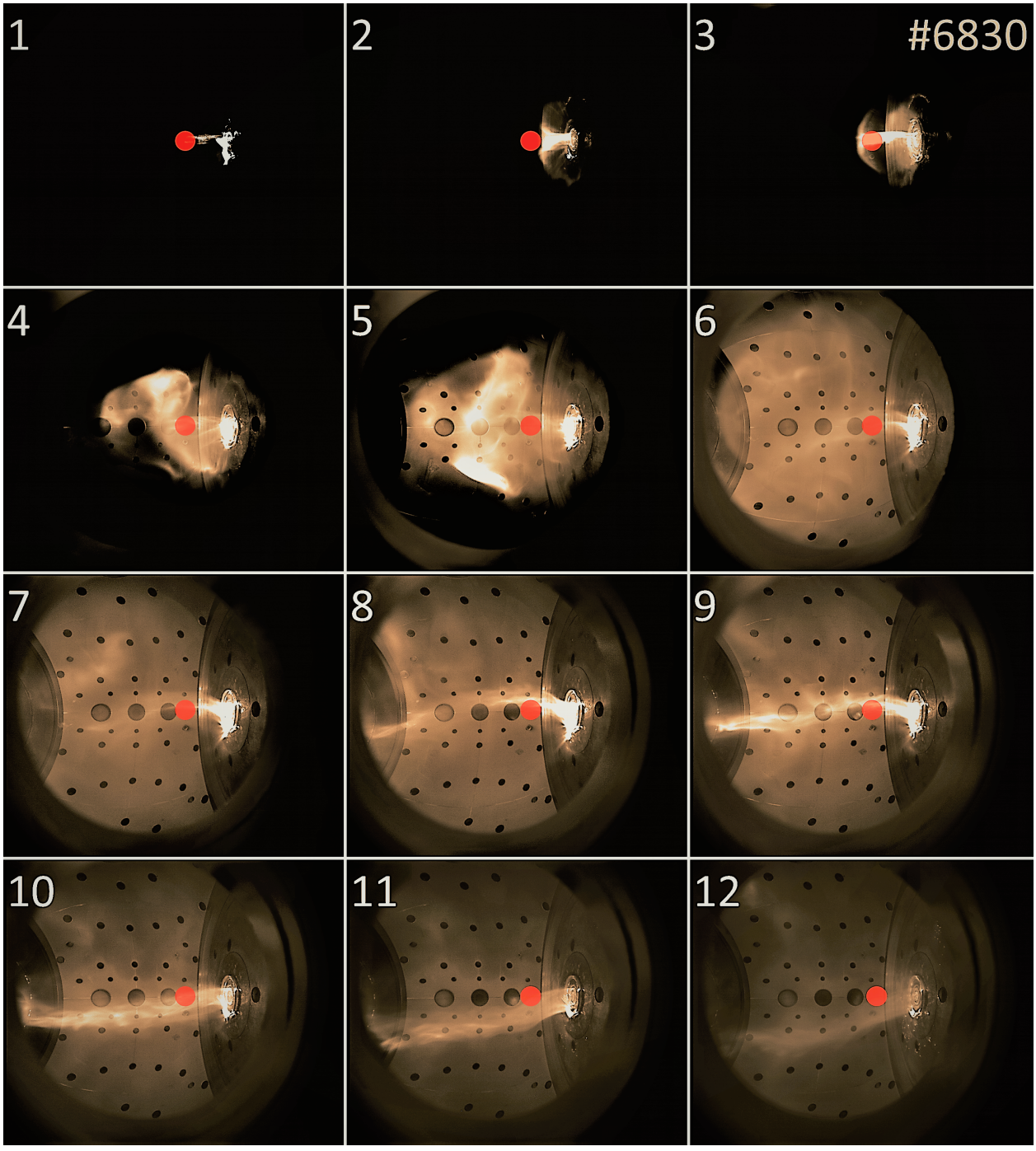

Figure 3.16: Frames taken from the Kirana video for shot #6830.

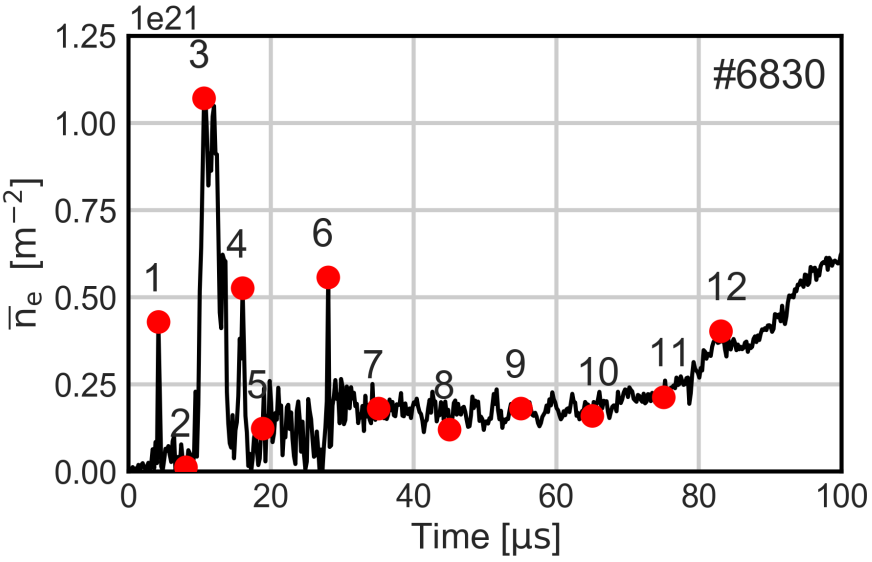

Figure 3.17: Line integrated density plot for shot #6830.

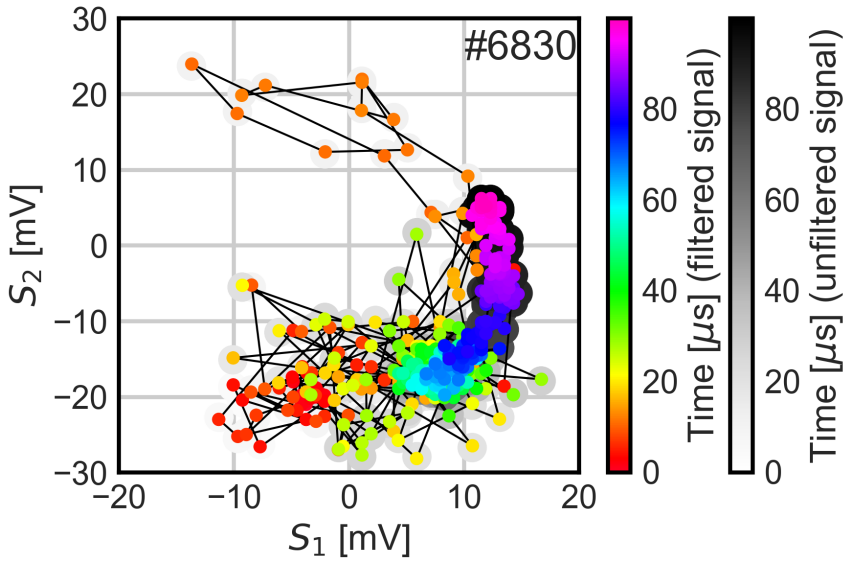

Figure 3.18: Lissajous figure produced over the course of shot #6830.

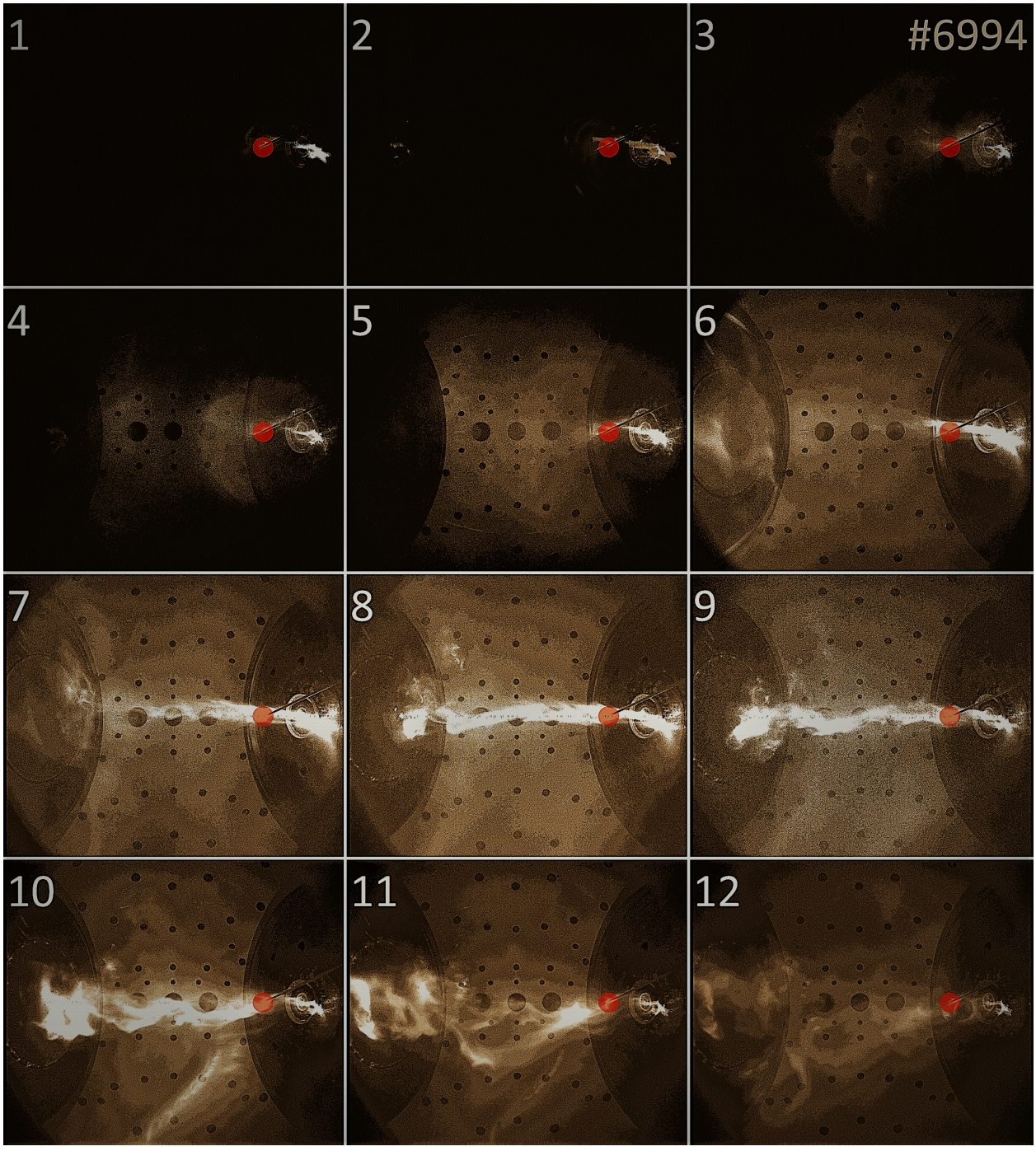

Figure 3.19: Frames taken from the Kirana video for shot #6994.

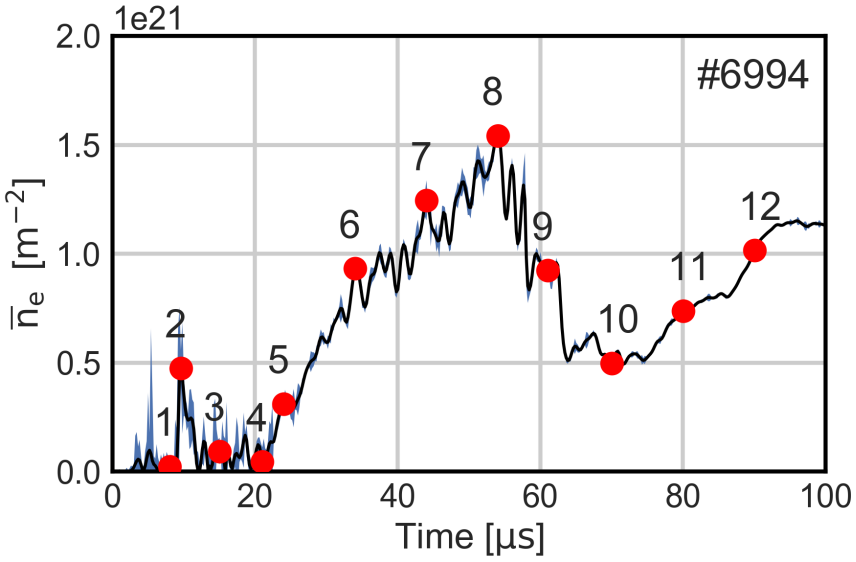

Figure 3.20: Line integrated density plot for shot #6994.

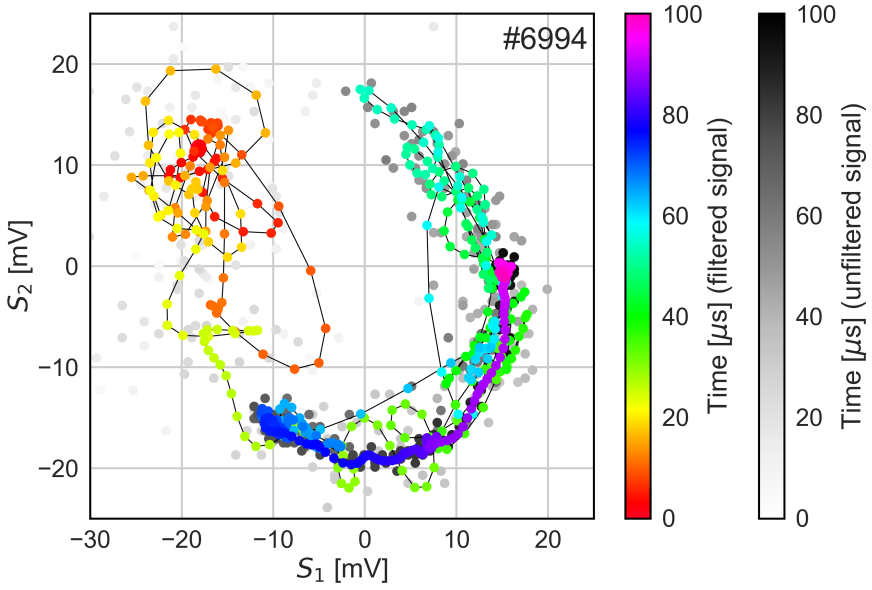

Figure 3.21: Lissajous figure produced over the course of shot #6994.

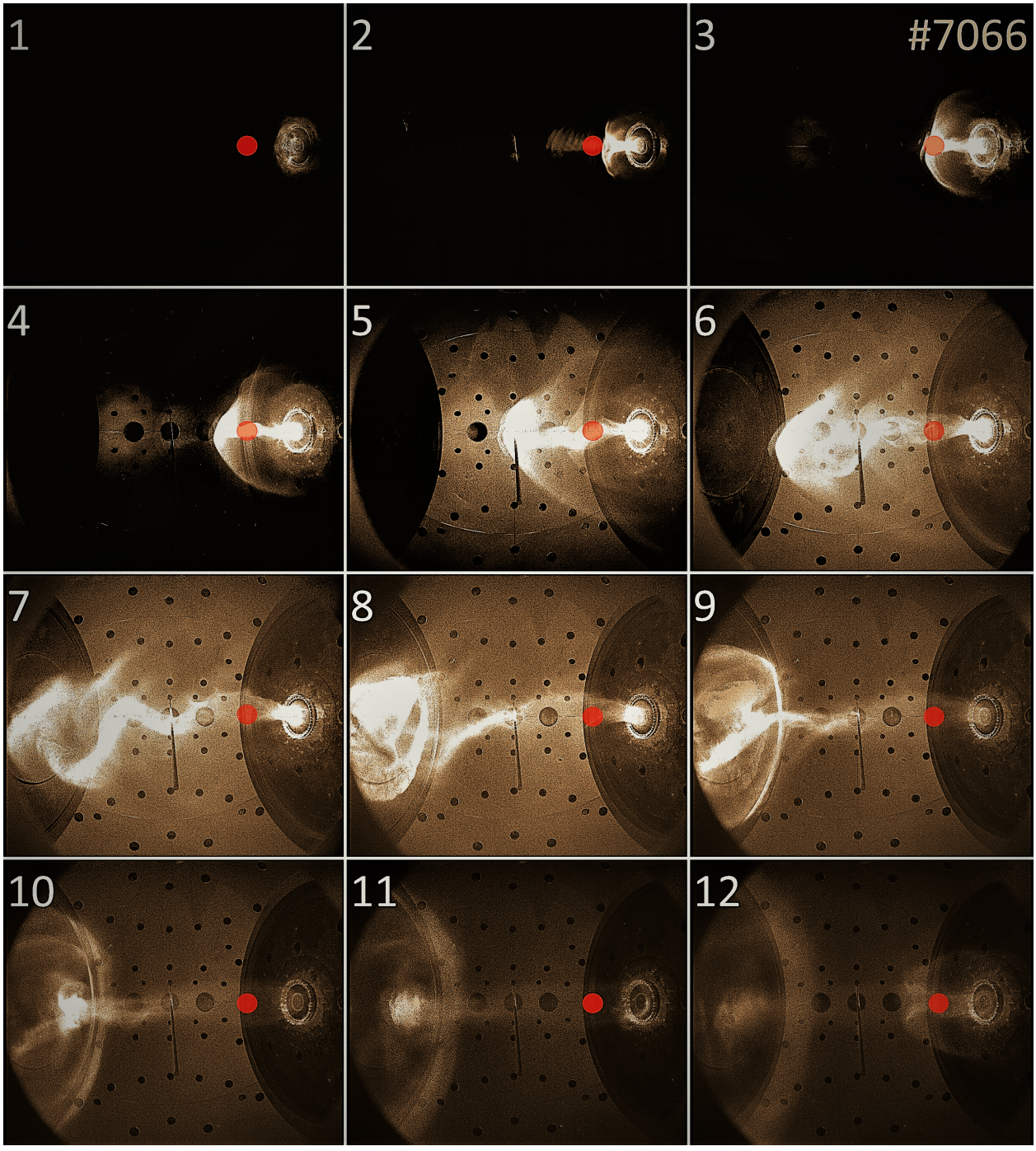

Figure 3.22: Frames taken from the Kirana video for shot #7066.

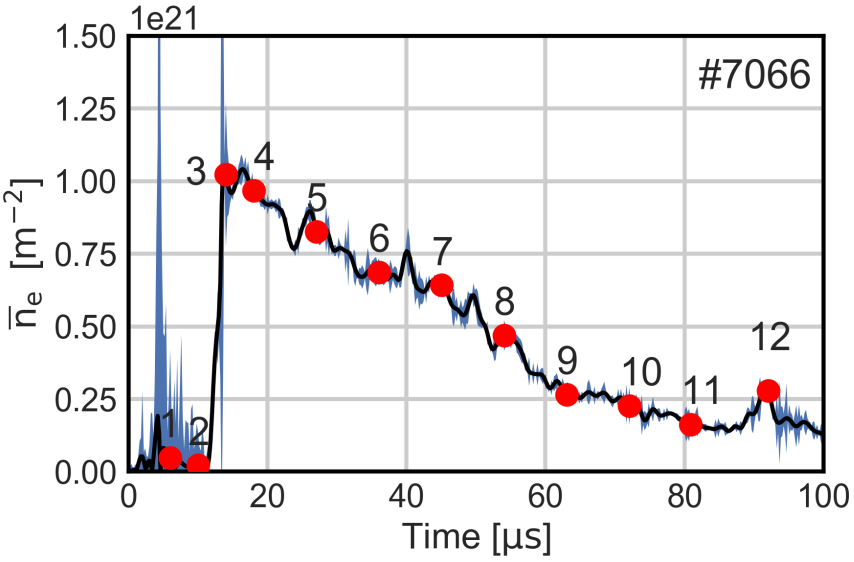

Figure 3.23: Line integrated density plot for shot #7066.

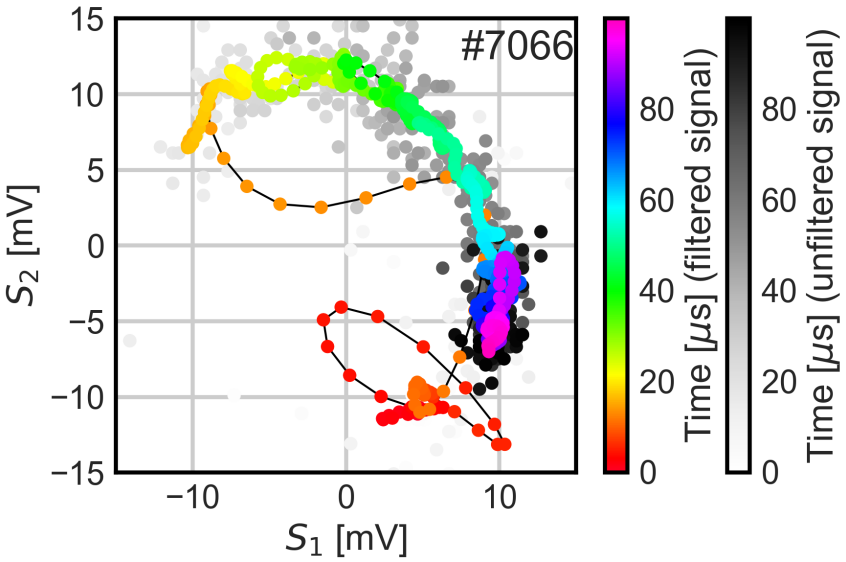

Figure 3.24: Lissajous figure produced over the course of shot #7066.

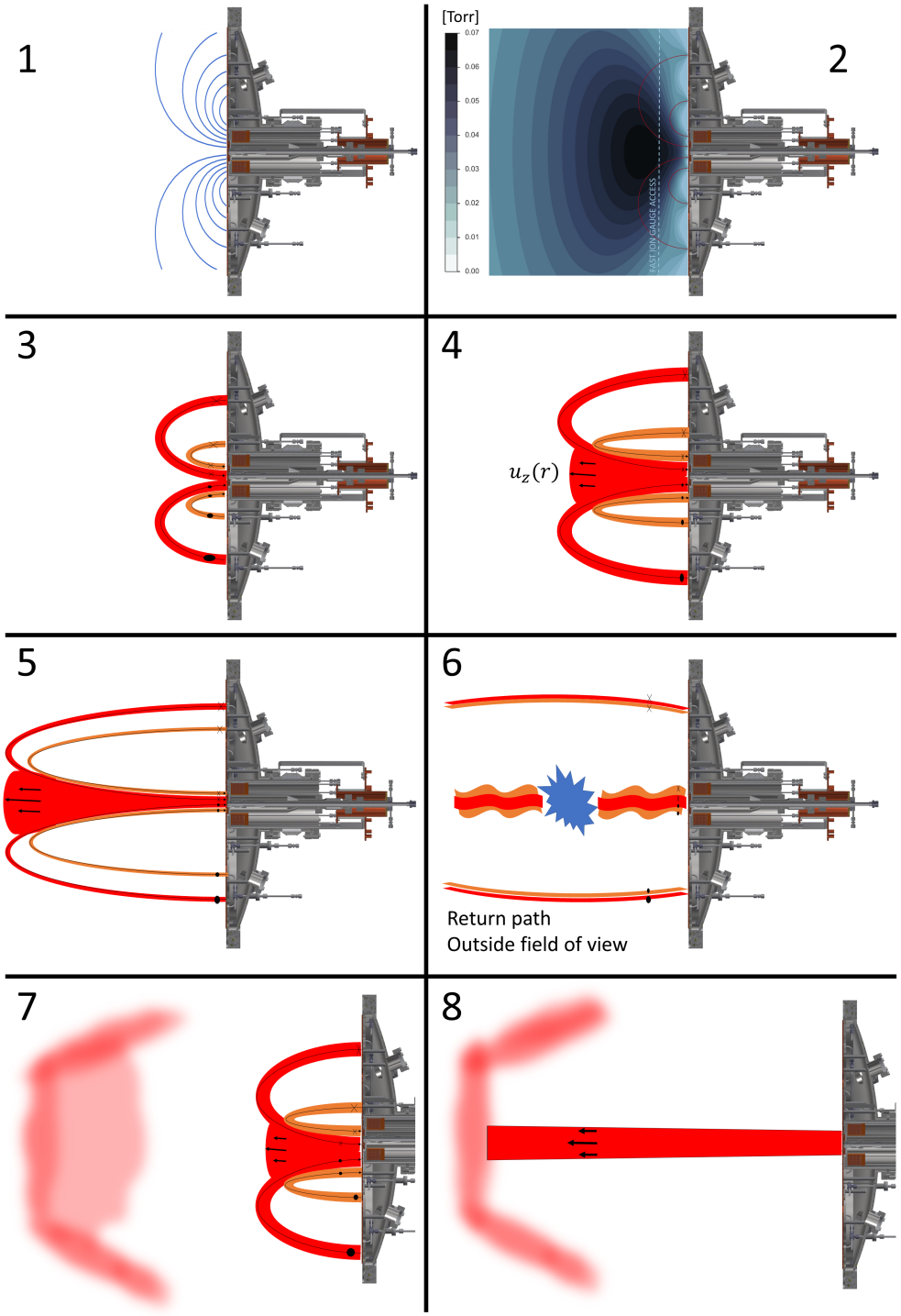

Figure 3.25: Step-by-step cartoon schematic of LabJet gun operation, updated for the long-duration, highly-stabilized, jet formation.

the current decreasing to zero its quarter cycle (90 μs, figure 1.7). We see from the coming shots that as the current dies away, the rotation apparently ceases, and the formation kinks. This marks the end of the relevant portion of the LabJet plasma discharge. As the current swings negative, plasmas are created, but these plasma are more unpredictable, and are not a focus of LabJet.

For the second operational campaign, the same diagnostic suite seen in the first operational campaign was used, with a single addition: a B-dot probe purposed to measure the magnetic field in three dimension [19]. This probe was added midway through the campaign, so it does not appear in the frames of shot #6830 (figure 3.16). For every shot, hydrogen was used (unless otherwise specified), and the interferometer laser chord was located at the *Near* position ($\sim 14\ cm$, figure 2.9).

Shot #6830 was a unique shot due to two reasons. The first is that the Lissajous figure did not need any filtering (figure 3.18); it is sampling at the the full 2.5 MHz Nyquist frequency. The second reason is its unique mushroom cloud shape, which forms when the collimated plasma jet collides with the diffuse plasma cloud. As seen in frames $2-4$ of figures 3.16 and 3.17, a strong plasma front blows by the laser over a span of 5 μs. In frame 4, the cloud curls back in, the creates a bright flash that propagates through the cloud. For the remainder of the shot a long, collimated plasma jet forms, which generally avoids the laser, curving around the beam during the time span of peak density (frames 8 and 9), so no density measurement is picked up. The experimental parameters were set as follows: the core gun was fired at 5 kV, the skin gun at 4 kV, the bias at 177.5 V, and all enabled valves at 1.1 kV. The banks were fired at $t = 0\ s$, and defines the experiment zero of the plasma discharge. The bias coil was fired at $-6\ ms$, the outer-outer gas valves at $-4\ ms$, the outer-inner valves at $-7\ ms$, the middle valve at $-6\ ms$, and the inner valve at $-7\ ms$.

Next, we come to shot #6994 (figures 3.19-3.3), the same shot used in the computational analysis of section 3.1. Looking at frames seen in figure 3.19, we find that the plasma first passes the laser at $\sim 10\ \mu s$ (frame 2). This is the short jet typical to planar plasma guns. The density, seen in figure 3.20, has a general positive trend that can easily bee seen past

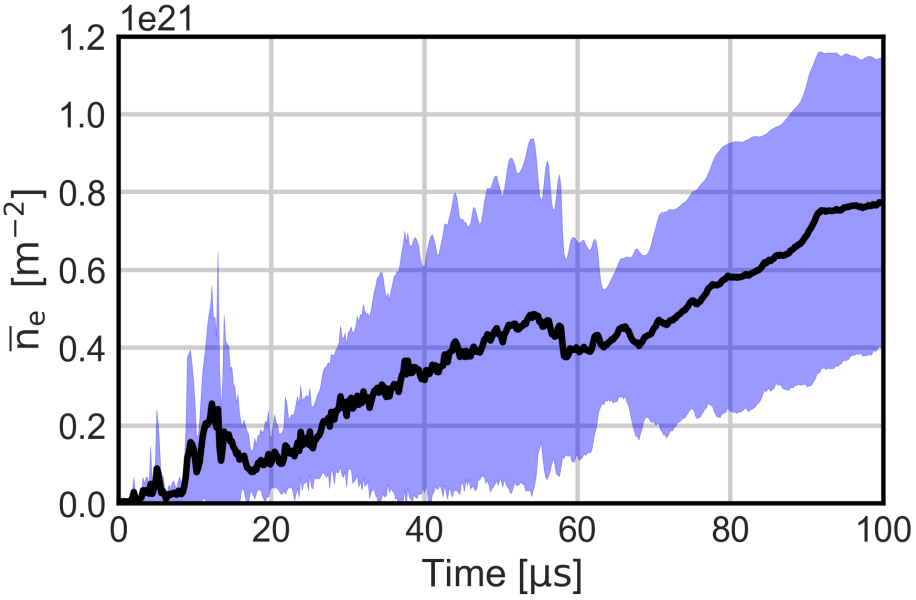

Figure 3.26: Plot displaying a trace taken over the best shots of the second campaign. Specifically, shots ...

70 μs (frames $10-12$). This is at the tail end of the gun current quarter-cycle (figure 1.7, so the highly-stable long jet has died out. Similarly the $J \times B$ forces decrease with the falling current [2]. The result is that plasma is created, but is not accelerated downstream, and builds in front of the face of the gun. Between frames 5 and 10, we see a rise above this trend: this is due to the long jet, which reaches a peak density of $\sim 1.5x10^{21}$ m^{-2} at 53 μs (frame 8). For shot #6994, the Lissajous was numerically 5th-order butterworth filtered at 750 kHz. The experimental parameters were set as follows: the core gun was fired at 5.7 kV, the skin gun at 6 kV, the bias at 176.5 V, and all enabled valves at 1.1 kV. The banks were fired at $t = 0$ s, and defines the experiment zero of the plasma discharge. The bias coil was fired at -6 ms, the outer-outer gas valves at -3.8 ms, the outer-inner valves at -4.5 ms, the middle valve at -4 ms, and the inner valve at -3.9 ms. Note that the B-dot probe has been added beginning with this shot, as seen in the images.

Shot #7066 (figures 3.22-3.24) was fired with nitrogen as the neutral gas. The Alfvén velocity is seen as the axial expansion of the plasma formation [2], which is defined in 3.7. Since v_A is inversely proportional to the root of the ion mass, the expansion rate of the nitrogen formation is reduced by this factor. Because of this, the initial plasma jet formation did not detach, and as the current rises to it's peak, the $J \times B$ forces cause the plasma column to coil as the later-in-time plasma accelerates into the existing plasma. This density measurement had the strongest front seen at with a $\sim 1\ \mu s$ rise time to $\sim 1x10^{21}$. It did not reach the end of the chamber until 45 μs. Secondary, and tertiary density fronts can be seen in frames 5 and 6, meaning that new bundt cake formations form after the jet is expanding, but do not break the column itself. For shot #7066, the Lissajous was numerically 5th-order butterworth filtered at 550 kHz. The experimental parameters were set as follows: the core gun was fired at 5.7 kV, the skin gun at 6 kV, the bias at 178 V, and all enabled valves at 1.1 kV. The banks were fired at $t = 0\ s$, and defines the experiment zero of the plasma discharge. The bias coil was fired at $-6\ ms$, the outer-outer gas valves at $-16.72\ ms$, the outer-inner valves at $-16.72\ ms$, the middle valve at $-13.84\ ms$, and the inner valve at $-13.46\ ms$.

3.3.1 Overview of the second operational campaign

Figure 3.26 is an overview of the campaign: the black line is the eight best plasma shots averaged, and the blue is the standard deviation of these shots. The uncertainty in these shots is small compared to the shot-to-shot deviation, so they were not included. We can see the short jet formation peaking at $\sim 10 - 15\ \mu s$ The positive-density trend, mentioned earlier, is evident in this plot: at this location, the interferometer was highly sensitive to the rising chamber pressure, due to its close proximity to the gas injection plenums. Peak density typically occurs from $45 - 55\ \mu s$, and is seen as a rise above the positive density trend.

3.4 Third Operational Campaign

The third operational campaign lasted from May to June 2017, and is marked by enabling of the final suite of diagnostics. The diagnostics added are: two more B-dot probes (now totaling three), and a 94-chord fiber bundle purposed for ion doppler spectroscopy. Look to Lavine, E.S.'s PhD dissertation to see results of both the B-dot probes and ion doppler spectroscopy [19]. It was in this campaign that the interferometer was placed in the three separate locations off the face of the electrodes (figure 2.9): Near ($\sim 14\ cm$), Middle ($\sim 54\ cm$), and Far ($\sim 94\ cm$). For all shots in this campaign, only hydrogen was used. The highest density observed occurred in this campaign: shot #7128, $2.5x10^{21}\ [m^{-2}]$ at 50 $[\mu s]$ (figures 3.28 and 3.29).

3.4.1 Near Location

The interferometer was in the Near position ($\sim 14\ cm$, figure 2.9) for shot #7093 (figures 3.31-3.33), which is the same as the first and second operational campaign. This shot displays a feature which is the result of a small arc over the alumina. This small arc does not sap much of the current, as evident by the long jet that is stabilized. It interacts with the long jet, a phenomenon that is most evident in frames $6-8$. When these arcs occur, the jet appears to splinter into multiple filaments, often times (as is the case with this shot) around the laser, seen in frames $6-9$ on the density plot. Frames 5 and 11 represent the only times when the jet directly bisected the laser chord. For this shot, the Lissajous was numerically 5th-order butterworth filtered at 600 kHz. The experimental parameters were set as follows: the core gun was fired at 6.0 kV, the skin gun at 5.7 kV, the bias at 175 V, and all enabled valves at 1.1 kV. The banks were fired at $t = 0\ s$, and defines the experiment zero of the plasma discharge. The bias coil was fired at $-6\ ms$, the outer-outer gas valves at $-3.8\ ms$, the outer-inner valves at $-4.5\ ms$, the middle valve at $-4\ ms$, and the inner valve at $-3.9\ ms$.

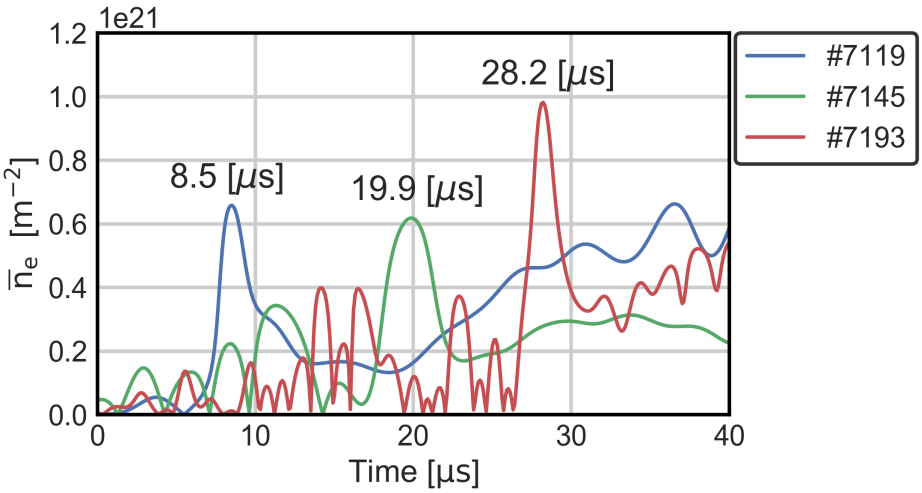

Figure 3.27: Estimation of axial jet propagation velocity. Seen is three plots taken at the three chord locations along the jet length.

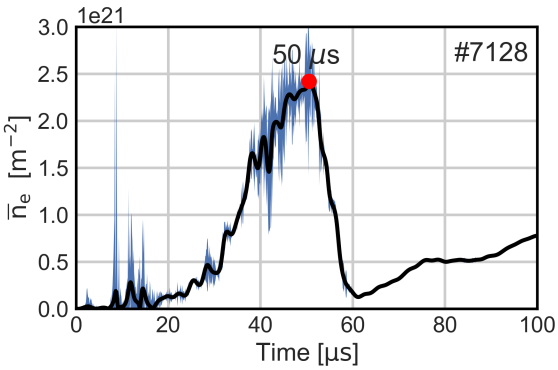

Figure 3.28: Plot of maximum density observed. Maximum density hits $\sim 2.5x10^{21}\ m^{-2}$ at 50 μs.

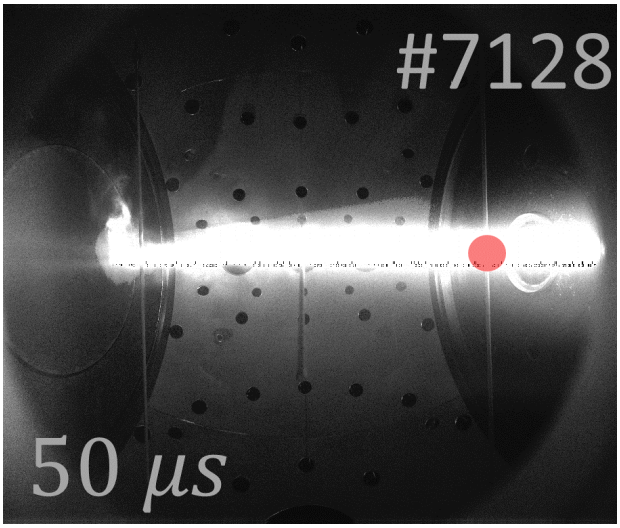

Figure 3.29: Picture of shot #7128 at maximum density: $\sim 2.5x10^{21}\ m^{-2}$ at 50 μs.

3.4.2 Middle Location

For shot #7145 (figures 3.34-3.36), the interferometer was moved to the *Middle* chord ($\sim$ 54 cm, figure 2.9). In the initial formation (frames $2-4$), we see two short jets form and break consecutively, with the initial density front crossing the laser chord at 20 μs. The jet then proceeds to form a splintered-arc collimation up until frame 8 where the splinters merged, and the jet straightened out. Being further from the electrode face, we find that the laser is more sensitive to spatial deviations of the jet. Peak density of $8x10^{20}$ m^{-2} occurs at $\sim$ 63 μs (frame 10). For this shot, the Lissajous was numerically 5th-order butterworth filtered at 250 kHz. The experimental parameters were set as follows: the core gun was fired at 6.1 kV, the skin gun at 5.7 kV, the bias at 175 V, and all enabled valves at 1.1 kV. The banks were fired at $t = 0$ s, and defines the experiment zero of the plasma discharge. The bias coil was fired at -6 ms, the outer-outer gas valves at -4.8 ms, the outer-inner valves at -6.5 ms, the middle valve at -6 ms, and the inner valve at -5.9 ms.

3.4.3 Far Location

The interferometer was located at the *Far* position ($\sim$ 94 cm, figure 2.9) for shot #7173 (figures 3.37-3.39). The long jet in shot #7173 is collimated along the $\hat{Z}$ axis up until the furthest B-dot probe, where the jet tip is highly mobile. Being furthest from the gun face, it is the most sensitive of the three position to spatial movement of the jet. This is evident in the density plot by many peaks and valleys, as the jet tip repeatedly swings across the laser chord, possibly even reflecting off the SpheromakGun and reflecting back into the chord. Note how at this chord position we do not see the positive trend in electron density that we saw in the *Near* position. As the current decreases from its peak value, the forces accelerating the plasma cease, so background density in the far end of the chamber does not rise on this time scale. Peak density of $1.1x10^{21}$ m^{-2} occurs at $\sim$ 63 μs (frame 9). For this shot, the Lissajous was numerically 5th-order butterworth filtered at 850 kHz. The experimental parameters were set as follows: the core gun was fired at 6.1 kV, the skin gun at 5.7 kV,

the bias at 178 V, and all enabled valves at 1.1 kV. The banks were fired at $t = 0$ s, and defines the experiment zero of the plasma discharge. The bias coil was fired at -6 ms, the outer-outer gas valves at -3.8 ms, the outer-inner valves at -4.5 ms, the middle valve at -4 ms, and the inner valve at -3.9 ms.

3.4.4 Long jet density

Figure 3.30 portrays the third campaign density, averaged over the nine best shots. The uncertainty in these shots is small compared to the shot-to-shot deviation, so they were not included. It is important to note that this data taken along three separate locations along the jet. The initial plasma fronts can be seen at the following locations: Near - ~ 10 μs, Middle - ~ 20 μs, and Far - ~ 30 μs. Note that the Near location wave front was consistently

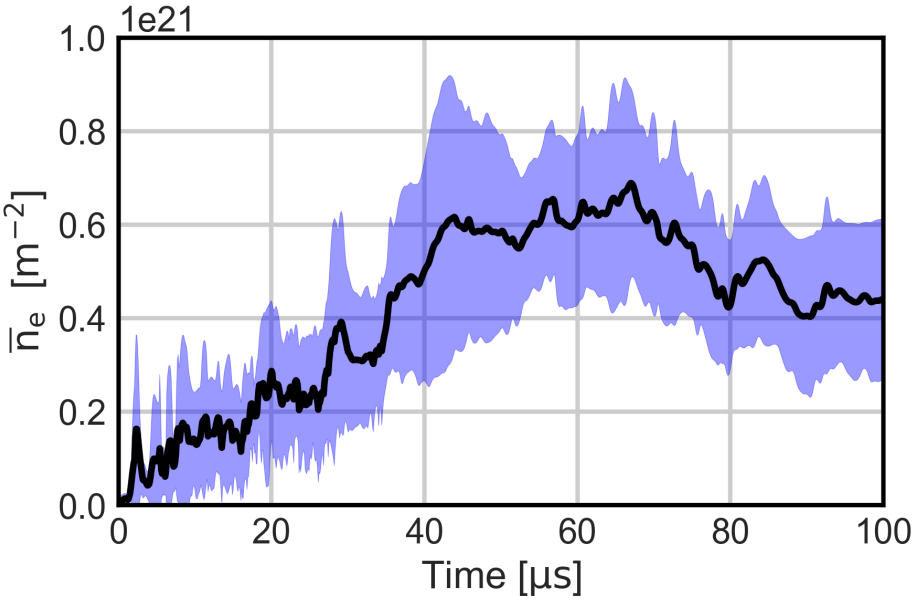

Figure 3.30: Plot displaying a trace taken over the best shots of the third campaign. This is averaged across three locations along the jet length. Note the relative flat region over the course of the long jet ($40 - 80$ μs).

shrouded in the noise that occurs during the early plasma discharge, so the peaks appear as a spread. The region from $40 - 80\ \mu s$ corresponds to the long jet region, and it appears to be linear over that extent. We find that the long jet has an average line integrated density of $\overline{n}_e = (6 \pm 2)x10^{20}\ \ [m^{-2}]$. The emission videos indicate that the jet has a diameter that varies widely. If we assume that the light emission corresponds to locations of electron density, we find that the jet diameter is $L_P = 10 \pm 5\ \ [cm]$. Equation 3.5 relates the total electron density n_e to the line integrated density $\overline{n}_e$ and the plasma length L_P, each of which are a source of uncertainty. The equation for the error propagation which results in the standard deviation of the electron density σ_{n_e} is shown in equation 3.6. Inserting the corresponding values, we find that the long jet has a electron density of $n_e = (6 \pm 3)x10^{21}\ \ [m^{-3}]$.

$$n_e = \frac{\overline{n}_e}{L_P} \tag{3.5}$$

$$\sigma_{n_e} = \sqrt{\left(\frac{\partial n_e}{\partial \overline{n}_e}\sigma_{\overline{n}_e}\right)^2 + \left(\frac{\partial n_e}{\partial L_P}\sigma_{L_P}\right)^2} = \sqrt{\left(\frac{1}{L_P}\sigma_{\overline{n}_e}\right)^2 + \left(-\frac{\overline{n}_e}{L_P^2}\sigma_{L_P}\right)^2} \tag{3.6}$$

3.4.5 Alfvén velocity and strength of axial magnetic fields

Figure 3.27 presents the first 40 μs of the three plasma shots with the most resolved initial density fronts, over the three chord locations. If the three available differences in time are taken in reference to the chord positions, we can obtain an estimation of the axial propagation velocity ($\hat{Z}$ axis) of the density front propagation velocity. At the *Near* chord position, the density front *is directly* a measurement of the axial velocity of the short jet, while at the *Middle* and *Far* chord positions the density front is the detached plasmoid. Under the assumption that the velocity at which the detached plasmoid propagates down the $\hat{Z}$ axis is representative of the axial expansion rate of density in the long jet, we can assume that this velocity is the Alfvén velocity [2, 9]. The Alfvén velocity is defined in equation 3.7, in CGS units, where $\mu = \frac{m_i}{m_p}$ is a ratio of the ion mass to the proton mass (equals 1 for hydrogen), n_i is the ion density (for an ionized hydrogen plasma, we can assume that $n_e = n_i$), B_z is

the axial magnetic field, and $C = 2.18x10^{11}$ [11].

$$v_A = \frac{B_z}{\sqrt{4\pi n_i m_i}} = C\mu^{-\frac{1}{2}} n_i^{-\frac{1}{2}} B_z \ \left[cm\ s^{-1}\right] \tag{3.7}$$

The axial long jet velocity was measured to be 41.3 ± 5.4 $\left[\frac{km}{s}\right]$. This speed is much higher than the neutral hydrogen speed of sound (1.3 $\left[\frac{km}{s}\right]$), so it is clear that the $J \times B$ forces have accelerated the plasma [27]. The uncertainty in the measurement of B_z is found using standard error propagation. Equation 3.8 is the variance of the uncertainty in B_z and equation 3.9 is the standard deviation of the measurement of B_z. After inserting the corresponding values, we arrive at a measurement of $B_z = 0.15 \pm 0.04$ $[T]$, with a confidence of $3.75\sigma_{B_z}$.

$$\sigma_{B_z}^2 = \left(\frac{\partial B_z}{\partial v_A}\sigma_{v_A}\right)^2 + \left(\frac{\partial B_z}{\partial n_i}\sigma_{n_i}\right)^2 + \left(\frac{\partial B_z}{\partial L_P}\sigma_{L_P}\right)^2 \tag{3.8}$$

$$\sigma_{B_z} = \sqrt{\left[\frac{\overline{n}_i^{\frac{1}{2}}}{CL_P^{\frac{1}{2}}}\sigma_{v_A}\right]^2 + \left[\frac{v_A}{CL_P^{\frac{1}{2}}\overline{n}_i^{\frac{1}{2}}}\left(\frac{1}{2}\sigma_{n_i}\right)\right]^2 + \left[\frac{v_A\overline{n}_i^{\frac{1}{2}}}{CL_P^{\frac{3}{2}}}\left(-\frac{1}{2}\sigma_{L_P}\right)\right]^2} \tag{3.9}$$

3.5 Future work

This single-chord interferometer can be thought of as a zeroth-pass diagnostic, and as such there are a few steps that can be taken to improve its functionality. Eliminating noise and need to visually inspect the Lissajous figure would allow for automation of the data analysis. Where the noise originates is a tricky topic to approach. Upgrades to the electronics box would include a low inductance ground plane to which all internal components would be attached with the active components place above the plane, and the PSUs below. The box should then be placed in a separate room, and the photodiode/AOM inside their own Faraday cages on the optical table; their wires shielded via a steel braid the whole length to the control room, as this is the effort that the ZaP flow Z-pinch experiment undergoes to keep noise out of their system [13, 7].

There is suspicion that the DC offsets, which arise from an unknown source in the system (author's guess would be the amplified photodiode chip), are not constant in time, however it is not possible to extract this information directly from the data. Furthermore, directly locating and measuring the offset in time would prove to be excessively difficult. The best way to remove this suspicion would be to add a DC-reference chord: build a second amplifier and associated electronics in the exact same way, and keep both scene and reference beam on the optical table. Or, it might be possible to utilize AC-coupling in the form of the MOCHI fast DAQs, or a high-pass filter, however the latter may introduce errors in tracking the $\Delta\phi$. While discussing the electronics, it is also worth mentioning that stabilizing the narrowband 'High Q' option in the amplified photodiode might allow for a Lissajous figure that is more robust against noise pickup.

The availability of diagnostic access on the MOCHI vacuum chamber allows access for multiple-chord interferometry, which would provide information on the propagation velocity of density features on a per-shot basis, rather than relying on shot-to-shot repeatability. With a relatively small addition of optical components the optical design could be re-worked to incorporate a second chord. This chord would be well suited to shine through the background plasma as a reference to help determine the density that is actually *in* the jet at the Near chord location. In summary, this diagnostic would benefit from five chords: one each at the Near, Middle, and Far positions, one looking into the chamber, but outside the jet purposed to measure chamber density over the course of a shot, and one that's entirely outside the chamber to get an independent measurement of noise and the time-dependence of the DC-offsets.

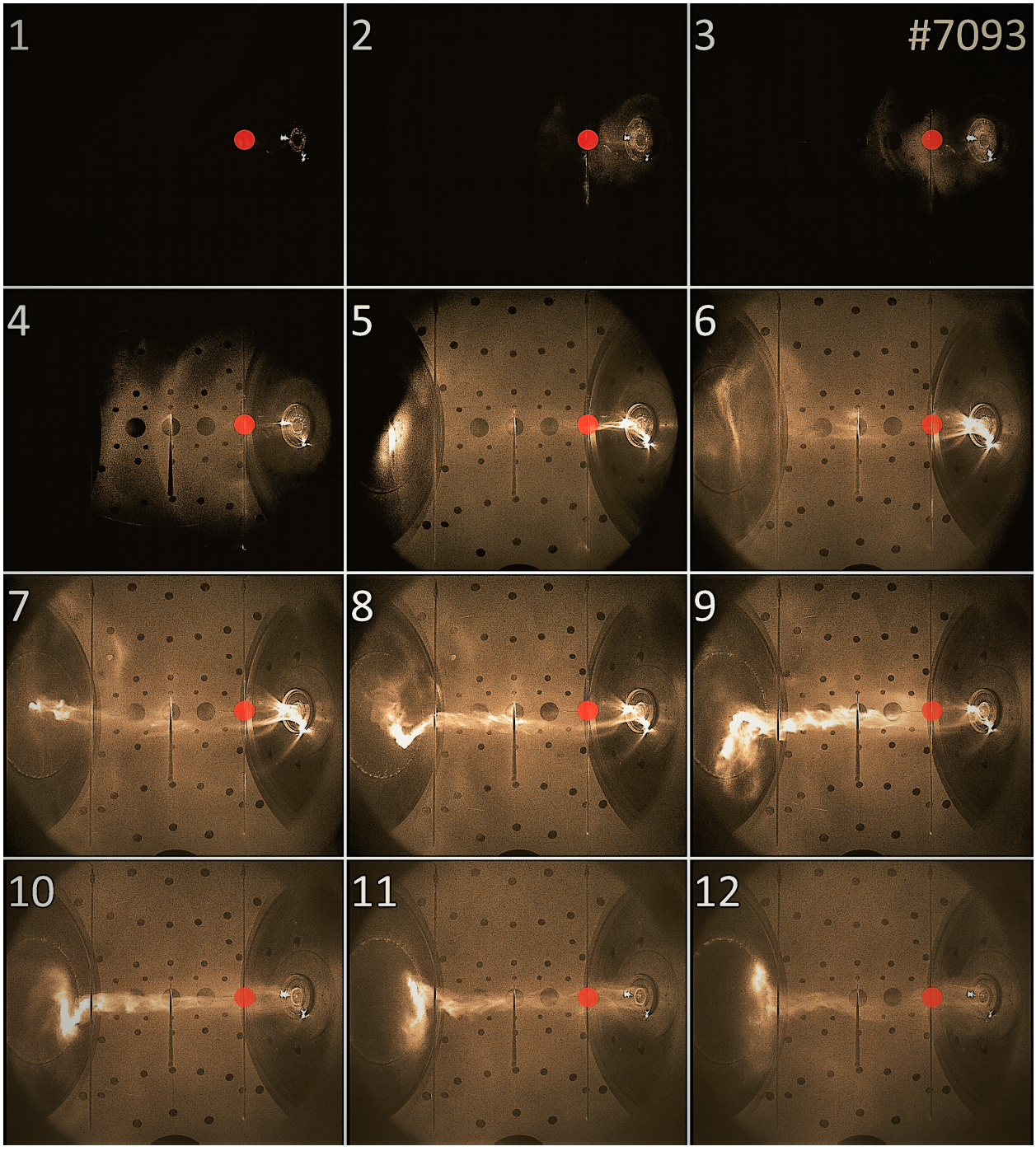

Figure 3.31: Frames taken from the Kirana video for shot #7093.

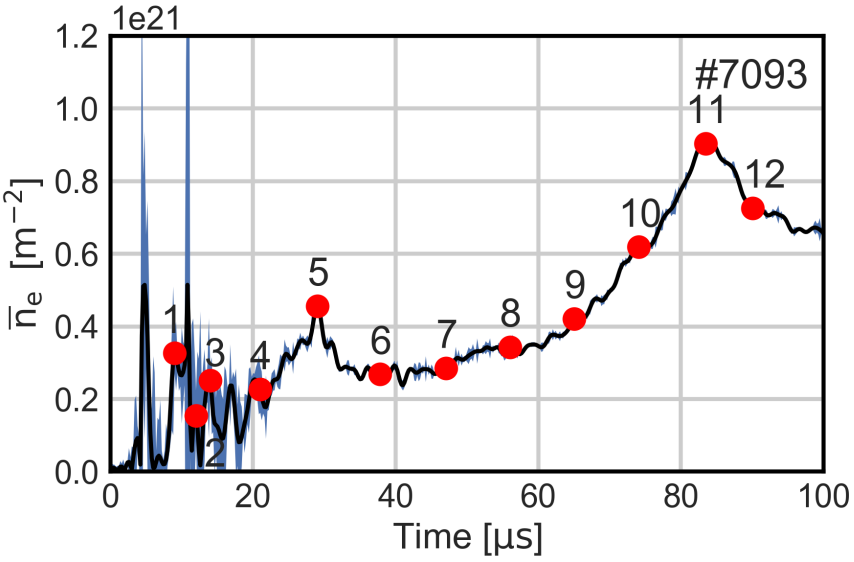

Figure 3.32: Line integrated density plot for shot #7093.

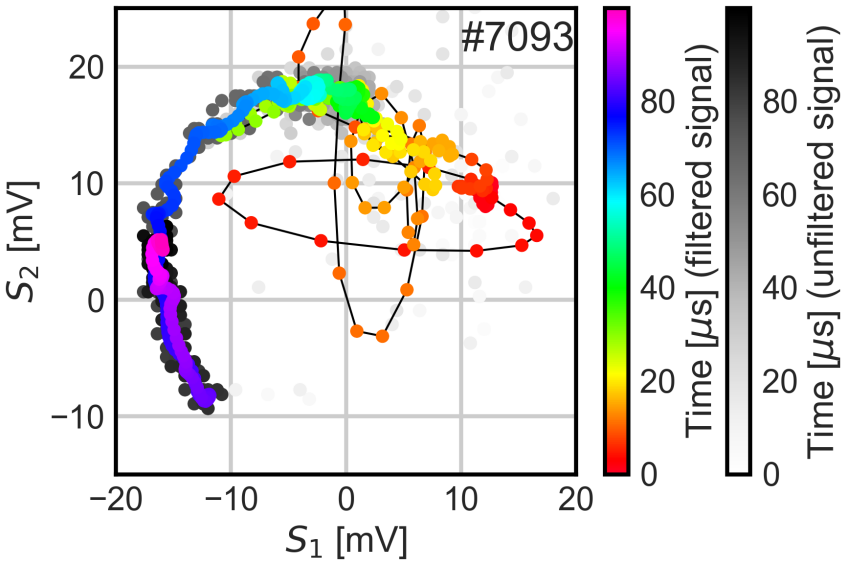

Figure 3.33: Lissajous figure produced over the course of shot #7093.

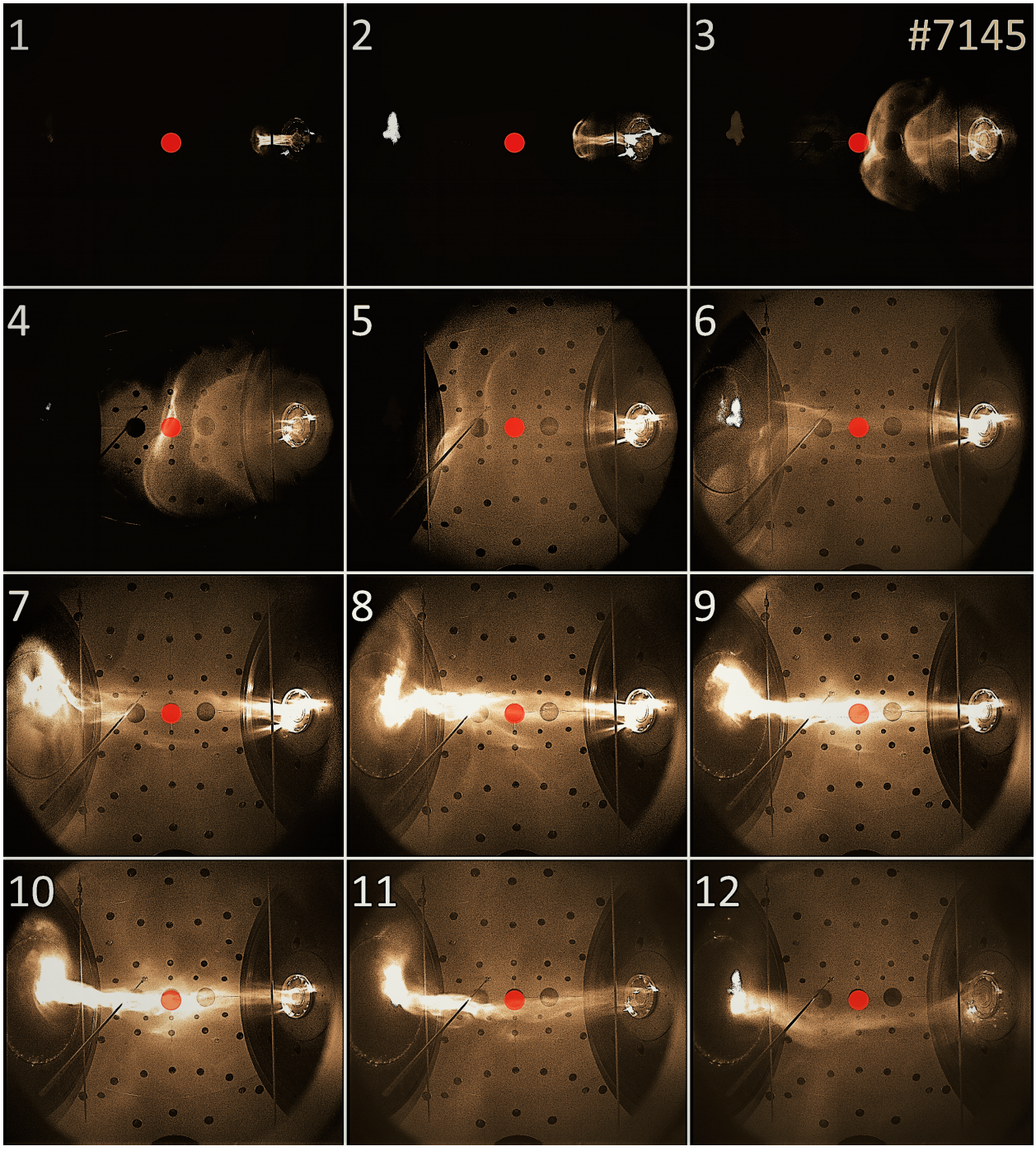

Figure 3.34: Frames taken from the Kirana video for shot #7145.

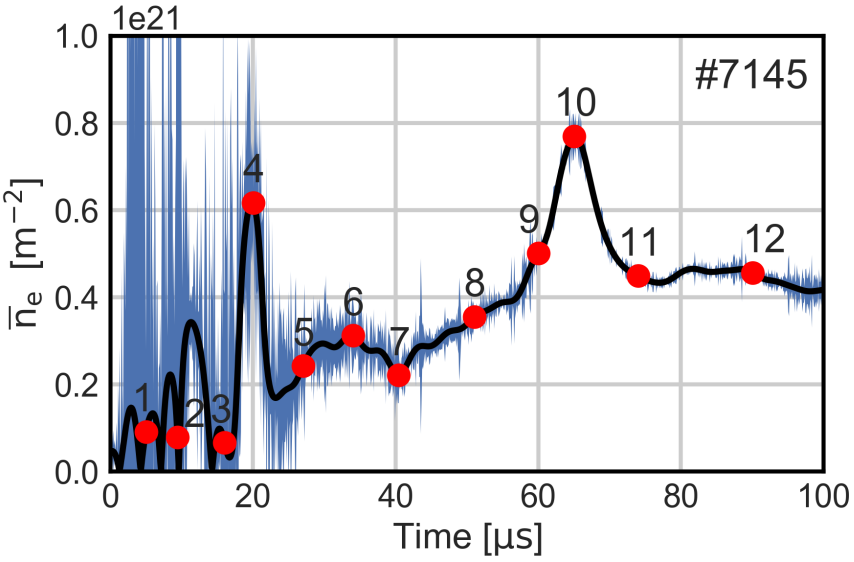

Figure 3.35: Line integrated density plot for shot #7145.

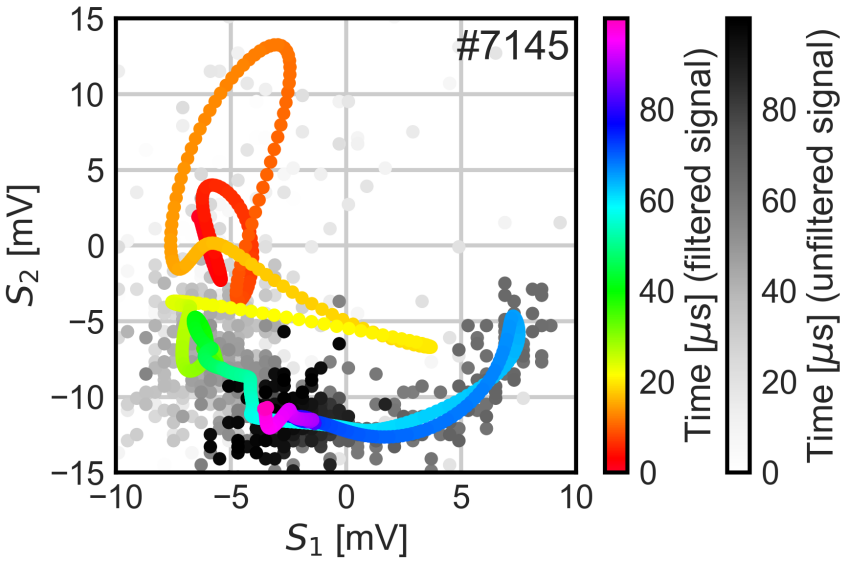

Figure 3.36: Lissajous figure produced over the course of shot #7145.

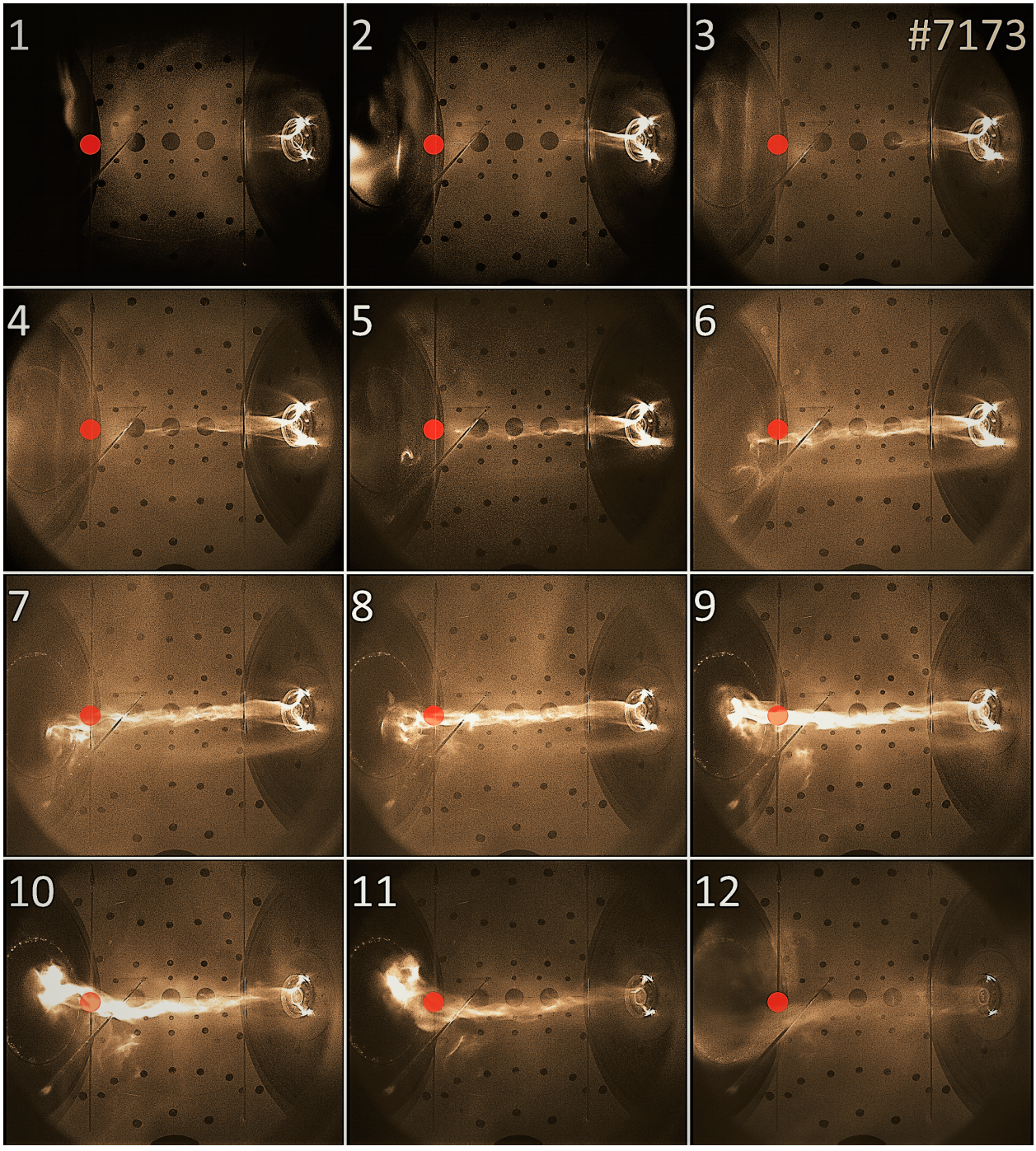

Figure 3.37: Frames taken from the Kirana video for shot #7173.

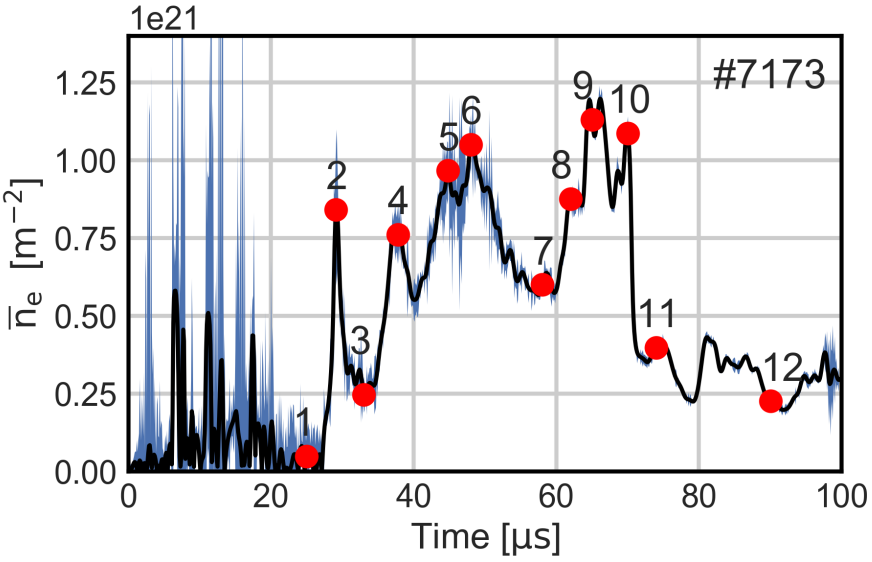

Figure 3.38: Line integrated density plot for shot #7173.

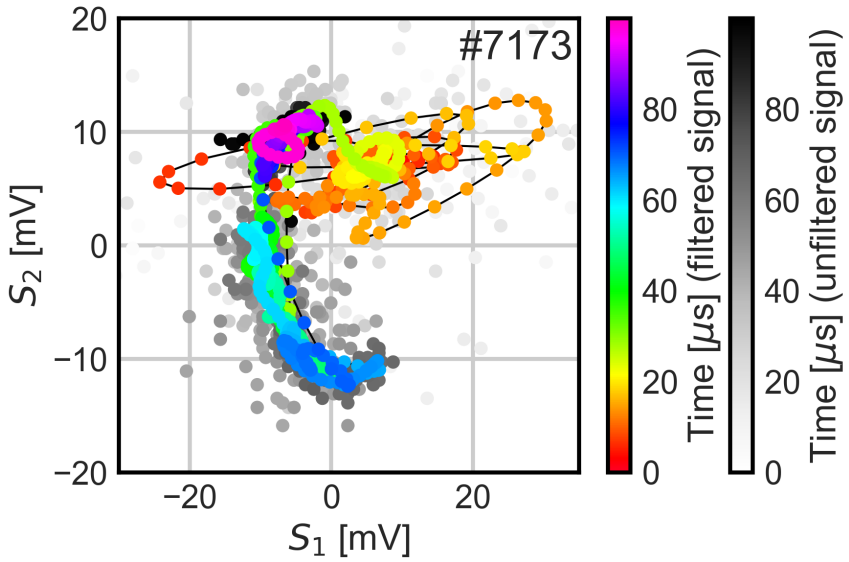

Figure 3.39: Lissajous figure produced over the course of shot #7173.

BIBLIOGRAPHY

[1] P.M. Bellan. Thermal instability of electrolytic capacitor bank used for gas puff valve. *Review of Scientific Instruments*, 73:2900–2905, 2002.

[2] P.M. Bellan. *Fundamentals of Plasma Physics*. Cambridge University Press, 2008.

[3] P.M. Bellan, S. You, and S.C. Hsu. Simulating astrophysical jets in laboratory experiments. *Kluwer Academic Publishers*, 2004.

[4] C.J. Buchenauer and A.R. Jacobson. Quadrature interferometer for plasma density measurements. *Review of Scientific Instruments*, 48:769–774, 1977.

[5] A. Card. MochiModel: MDSplus tree for MochiLab & Mochi.Labjet. Zenodo, 2017.

[6] E. Carroll. Driving flows in laboratory astrophysical plasma jets: The Mochi.Labjet experiment. Master's thesis, University of Washington, 2016.

[7] B.J. Chan. Four-chord interferometer measurements of the zap flow z-pinch. Master's thesis, University of Washington, 2008.

[8] J.P. Freidberg. Ideal magnetohydrodynamic theory of magnetic fusion systems. *Reviews of Modern Physics*, 54:801–902, 1982.

[9] R.J. Goldston and P.H. Rutherford. *Introduction to Plasma Physics*. Institute of Physics Publishing, 1995.

[10] R. Golingo. *Formation of a Sheared Flow Z-Pinch*. PhD thesis, University of Washington, 2003.

[11] J.D. Huba. *NRL Plasma Formulary*. Plasma Physics Division, Naval Research Laboratory, 2009.

[12] H. Hutchinson. *Principle of Plasma Diagnostics*. Cambridge University Press, second edition, 2002.

[13] S. Jackson. *Density Characteristics of a Sheared-Flow Z-Pinch*. PhD thesis, University of Washington, 2006.

[14] A.R. Jacobson. Heterodyne quadrature interferometer for simultaneous measurements of plasma density along several chords. *Review of Scientific Instruments*, 49:673–674, 1978.

[15] F.A. Jenkins and H.E. White. *Fundamentals of Optics*. McGraw-Hill Book Company, Inc., third edition, 1957.

[16] R. Kristal and R.W. Peterson. Bragg cell heterodyne interferometry of fast plasma events. *Review of Scientific Instruments*, 47:1357–1359, 1976.

[17] D. Kumar. *Experimental Investigations of Magnetohydrodynamic Plasma Jets*. PhD thesis, California Institute of Technology, 2009.

[18] D. Kumar and P.M. Bellan. Heterodyne interferometer with unequal path lengths. *Review of Scientific Instruments*, 77, 2006.

[19] E.S. Lavine. *PhD thesis title TBD*. PhD thesis, University of Washington, 2018.

[20] E.S. Lavine and S. You. The tolopology of canonical flux tubes in flared jet geometry. *The Astrophysical Journal*, 2017.

[21] H.W. Liepmann and A. Roshko. *Elements of Gasdynamics*. Courier Corporation, 1957.

[22] G. Manduchi, E. De Marchi, and A. Mandelli. A new labVIEW interface for MDSplus. *Fusion Engineering and Design*, 88, 2013.

[23] J. von der Linden. *Investigating the Dynamics of Canonical Flux Tubes*. PhD thesis, University of Washington, 2017.

[24] J. von der Linden, A. Card, S. You, and J. Stuber. MochiControl: LabVIEW experiment control with MDSplus data storage. Zenodo, 2017.

[25] J. von der Linden and S. You. Sausage instabilities on top of kinking lengthening current-carrying magnetic flux tubes. *Physics of Plasmas*, 2017.

[26] S. You. The transport of relative canonical helicity. *Physics of Plasmas*, 19, 2012.

[27] S. You, G. Yum, and P.M. Bellan. Dynamic and stagnating plasma flow leading to magnetic flux tube collimation. *Physical Review Letters*, 95, 2005.

Appendix A

ADDITIVE MANUFACTURING AND MONOLITHIC INTERFEROMETRY

A.1 Motivation of Concept

Additive manufacturing (AM) is a rapidly-evolving industry. It offers a manufacturing process by which material is added, typically layer-by-layer, to produce the final part. 3D printing is a common example of AM: two common types available at low cost are thermoplastic extrusion (PLA, ABS plastics) and laser sintering. 3D printers accept solid-surface model files (STEP, STL), produced by a CAD design program such as SolidWorks or Autodesk Inventor. The printing firmware decides the internal structure of the part using the surfaces as boundary conditions, as well as the printing process details, such as the amount of material to be consumed, the tool path (in the case of extruded plastic), and thus the total print time. As the part is designed using CAD software suites, and manufactured with an additive process, complexity comes free. That is, an increase in part complexity will not result in an disproportionate increase in part cost.

Plasma devices offer extreme environments, which often necessitate complicated diagnostic designs that are even more often unique to the limitations of the specific experiment, and on top of that no two experimental plasma devices are exactly alike. Differences in, for example, space available for diagnostic, angle of view to the plasma, plasma density, temperature, and magnetic field, will all provide design limitations unique to the device. Figure A.1 is a good example of AM overcoming an obstacle with ease: a CF mirror mount that holds the mirror exactly perpendicular to the CF window, is height and rotationally-adjustable, and has the capabilities of the two kinematic adjusters inherent to the commercial mirror from THORLABS. AM can offer rapidly-prototyped, increasingly complicated solutions to

such limitations (such as figure A.1), and furthermore do not require experienced staff to implement.

A.2 Additive manufactured unequal path length, heterodyne interferometer

The compact, isolated nature of the optomechanical pieces in the unequal path length, heterodyne interferometer (discussed in chapter 2) lends well to monolithic replication (figure A.2). The Monolithic, Unequal Path Length Interferometer (MUPLI) was modeled using Autodesk Inventor, and the mirror faces were aligned using constrictions on construction planes. The angles of the construction planes were manually calculated, propagating from the separation angle of the AOM crystal (figure A.3. The end result is that the pieces seen in figure A.2 can be dragged around by the user, and the alignment remains preserved. This will enable the most compact design, for a two-dimensional optical plane.

The foremost benefit to a AM monolithic interferometer is that the alignment is preserved; there is little to nothing to adjust. Not everything is printed: pieces such as the light source, mirrors and beamsplittters would still come from conventional suppliers. However, the end-user would simply insert the mirrors into the non-adjustable mounts, and the device would be aligned, removing the need for skilled optomechanical time. This removes cost, and not just labor costs, but also component costs. Another benefit to a monolithic interferometer is its capability for expansion. Adding more chords to the diagnostic needs only the time spent with CAD model, and the cost of extra mirrors, and a new print. The laser-sintered 3D printing process provided by ShapeWays was selected as the print provider. The initial design seen in figure A.2 was larger than the upper threshold of ShapeWays' print volume. Therefore, it was decided that a Proof-of-Principle (PoP) design showcasing a working, simple, 3D-aligned, Michelson interferometer would be a cost-efficient endeavor.

A.3 Proof-of-Principle interferomter

The first attempt at creating a working monolithic interferometer is seen in figure A.4. This designed failed, as contraction in the printed plastic caused the component mounts to deviate

from their press-fit dimensions; some of the mirrors didn't fit. Modifications were made to attempt to fit the mirrors properly, but for a HeNe the room for error is little to none.

Figures A.5 through A.8 display attempts made to compensate for the contraction in the printed mirror mounts. These various standardized mount designs were printed with a varying amount of material surrounding the mount itself. The deviation in mount diameter printed versus diameter specific in Inventor was measured, and incorporated into the CAD model.

The second attempt at a working monolithic interferometer is seen in figure A.9. As you can see, the new mounts were implemented, and they served their function well: the mirrors made a solid, press-fit connection. However, this design failed since another contraction made itself evident: contraction in the lone vertical extension opposite the beamsplitter.

Figure A.10 was the third and final iteration attempting to achieve interference. The vertical extension was stabilized against the beamsplitter mount section, this appeared to be successful. Another design implemented was a beam expansion cavity that expanded the beam by a factor of ten. This allowed the widened laser to hit every mirror (figure A.11), however the design still failed to achieve any indication of interference.

A.4 Discussion and Future Work

Even though the third iteration was successful in guiding the laser to each mirror face, the design ultimately failed on a conceptual level. The miniscule étendue of a HeNe laser makes it highly sensitive to any spatial deviations. The only way to make the design work would be to add adjustable components, either commercial or custom. However, this would mean that the interferomter needs to be aligned, which defeats the original purpose of ingrained laser alignment. Some ideas for a PoP design using a single adjustable beamsplitter mount can be seen in figures A.12 and A.13.

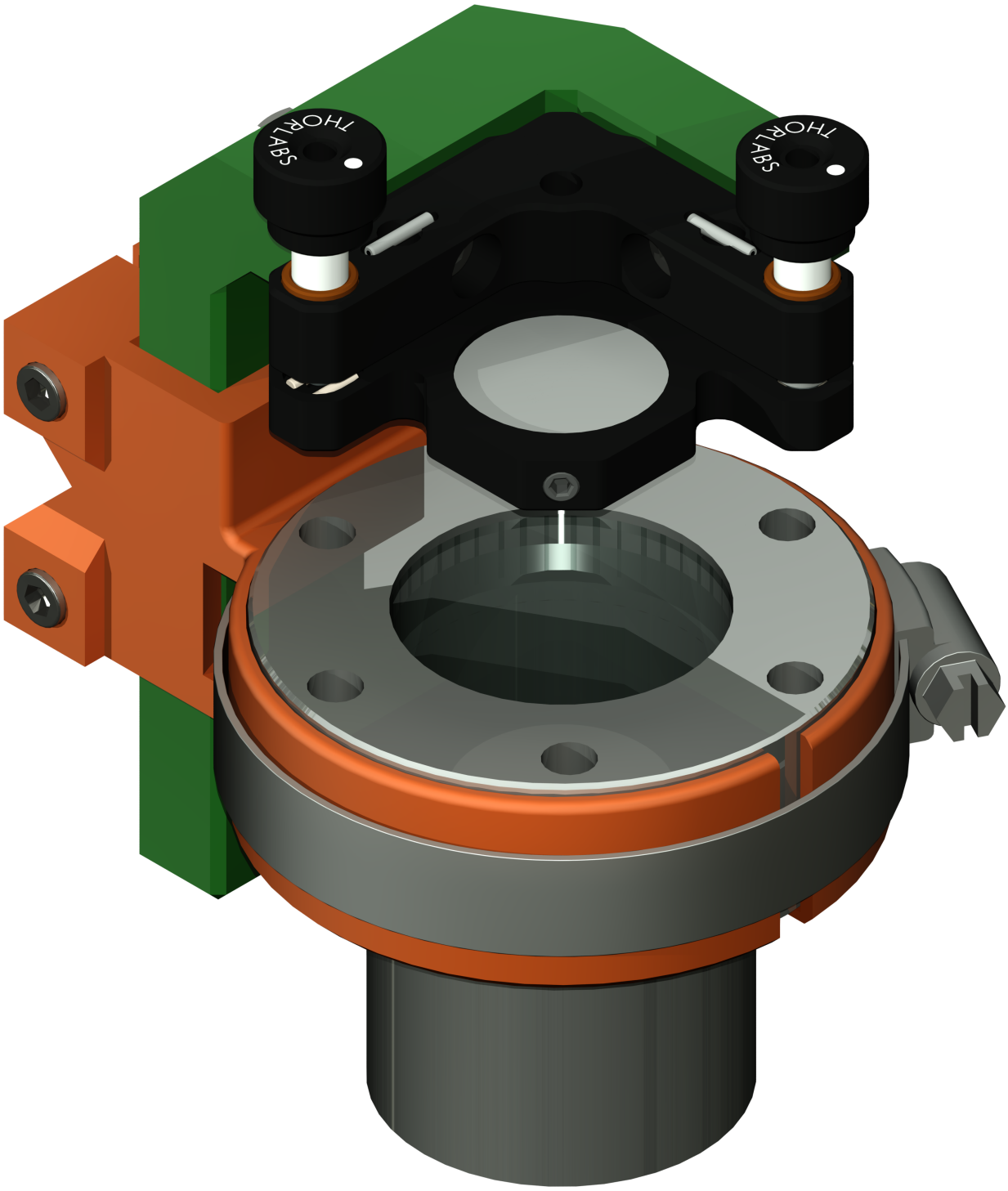

Figure A.1: ConFlat optical mount

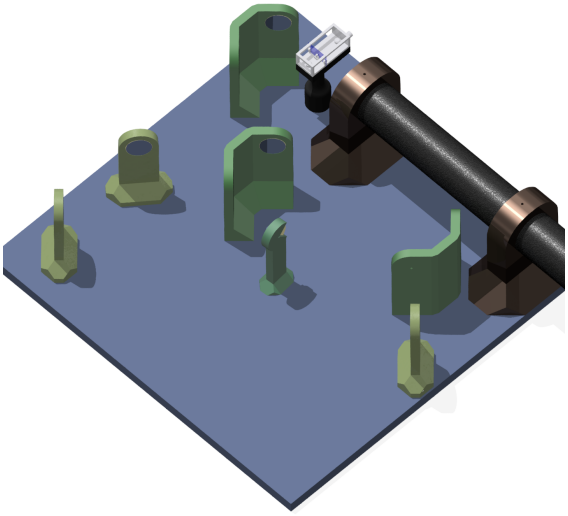

Figure A.2: Monolithic, Unequal Path Length Interferometer (MUPLI) was initially going to replicate the interferomter discussed in chapter 2.

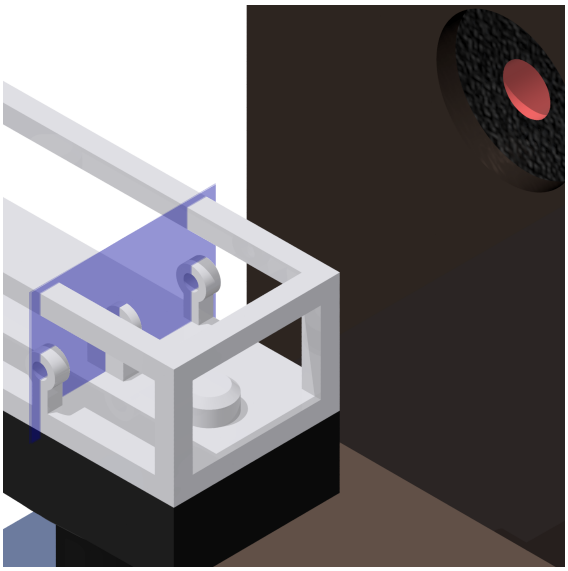

Figure A.3: Bragg separation planes of the AOM seen accurately represented via the visible construction planes.

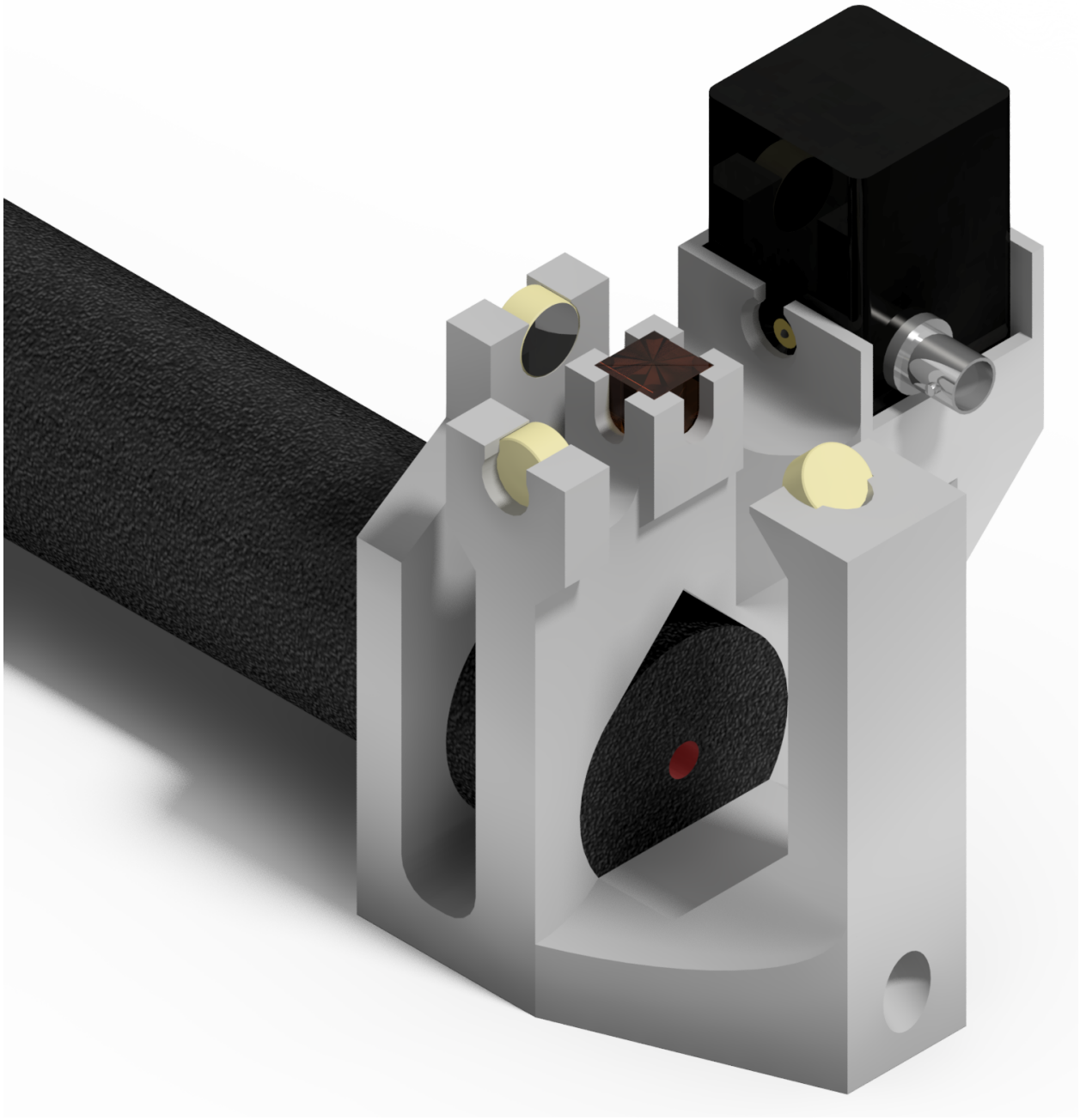

Figure A.4: Micro-Michelson: V1 design. The initial 3-D design. This did not have the print accuracy to guide laser properly to the recombination beamsplitter.

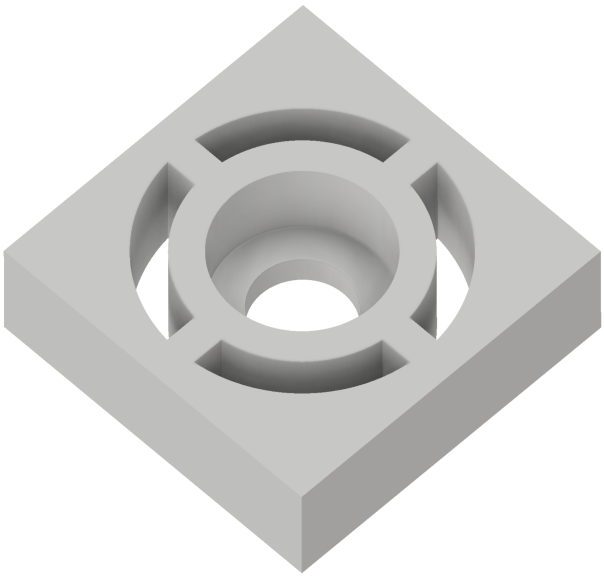

Figure A.5: Contraction testing: Round mount with minimal surrounding material

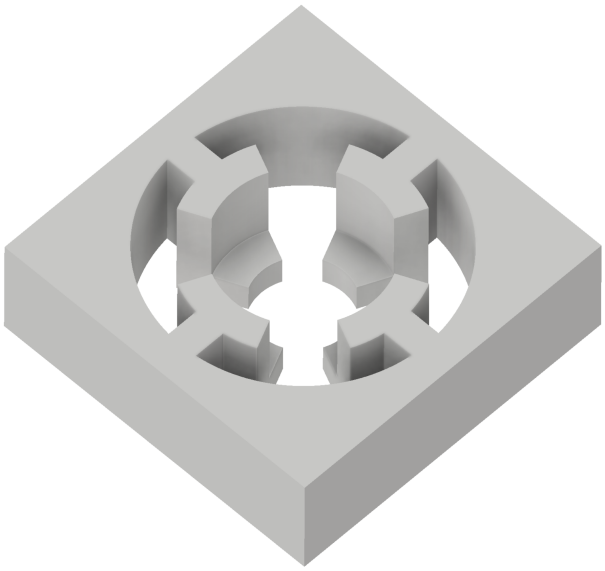

Figure A.6: Contraction testing: Discrete mount with minimal surrounding material

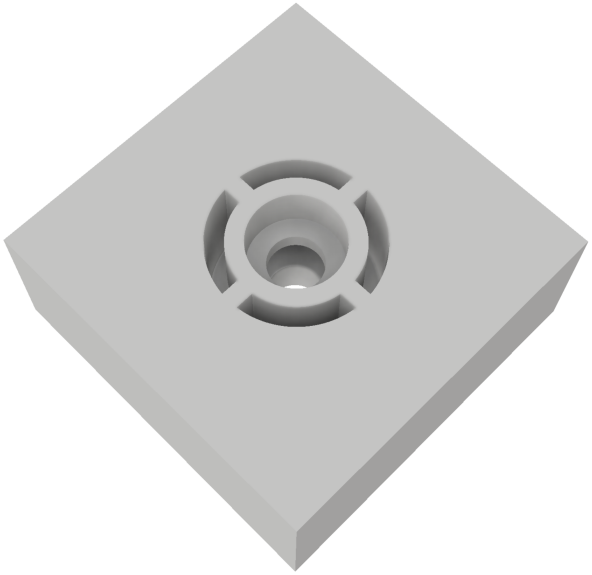

Figure A.7: Contraction testing: Round mount with excessive surrounding material

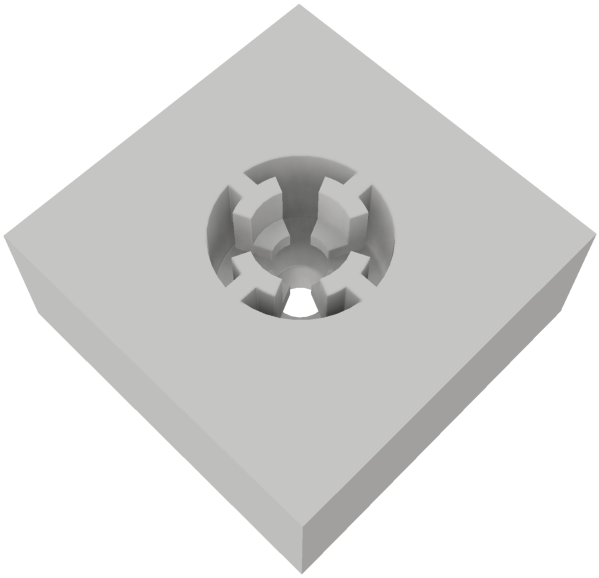

Figure A.8: Contraction testing: Discrete mount with excessive surrounding material

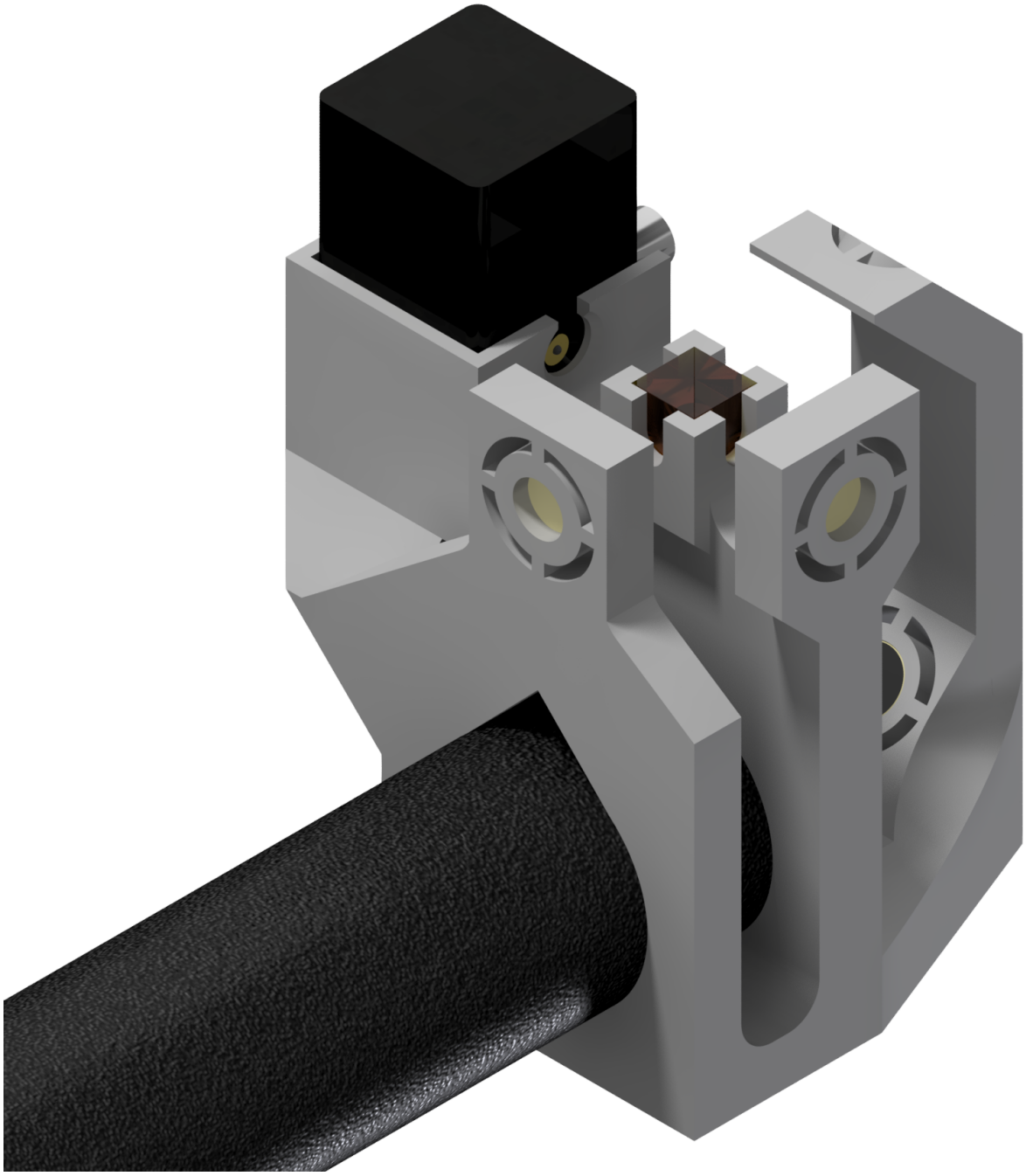

Figure A.9: Micro-Michelson: V2 design. The first iteration on figure A.4. This design incorporated the contraction-calibrated mirror mounts. The small deviations still ruined the laser alignment.

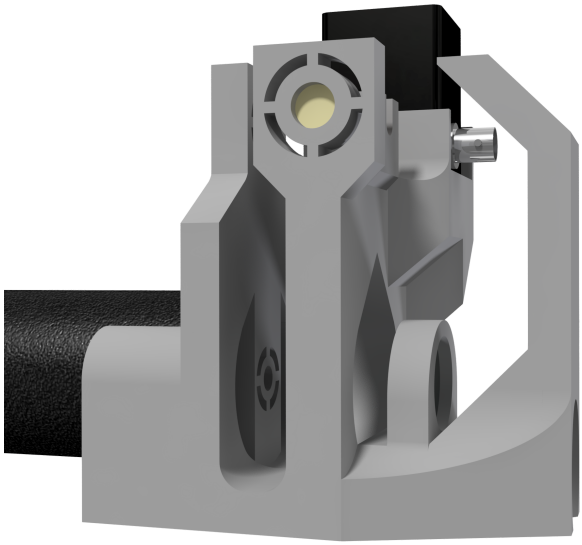

Figure A.10: Micro-Michelson: V3 design. The laser was expanded, and the top section stabilized against contraction. Produces the alignment seen in figure A.11.

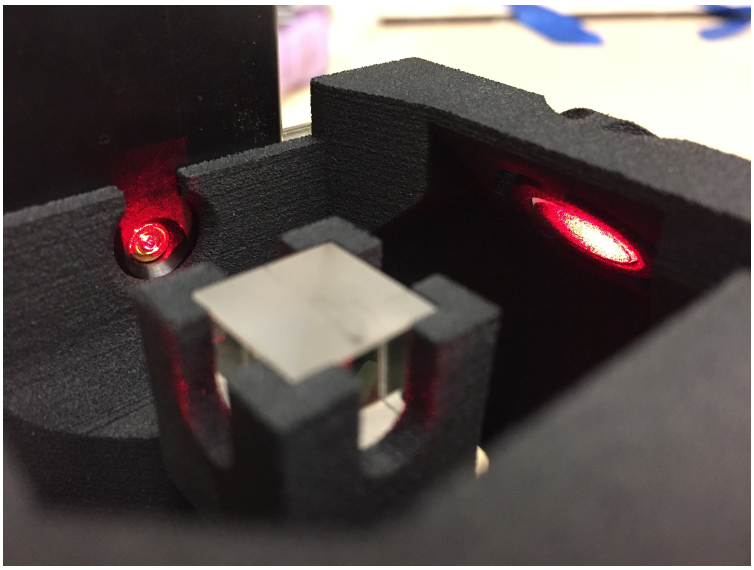

Figure A.11: Micro-Michelson: V3 alignment. Produced from the design seen in figure A.10. While the design did send the laser along the correct paths, we did not see any signature of interference.

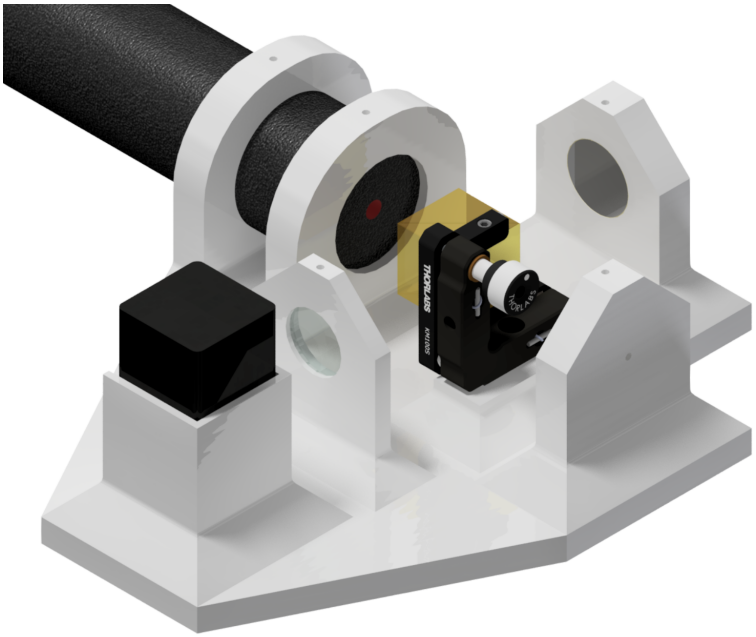

Figure A.12: Hyper compact Michelson design. Note how all angles are 90^o.

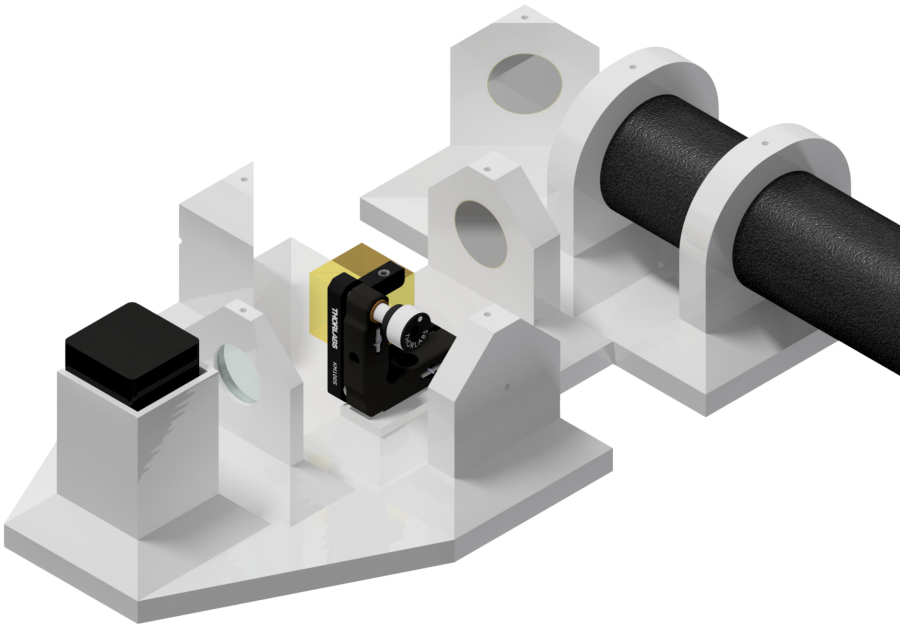

Figure A.13: Compact Michelson design. This design incorporates an angle to test the capability of manufacturing accuracy.

Appendix B

ENGINEERING DRAWINGS AND DIAGRAMS

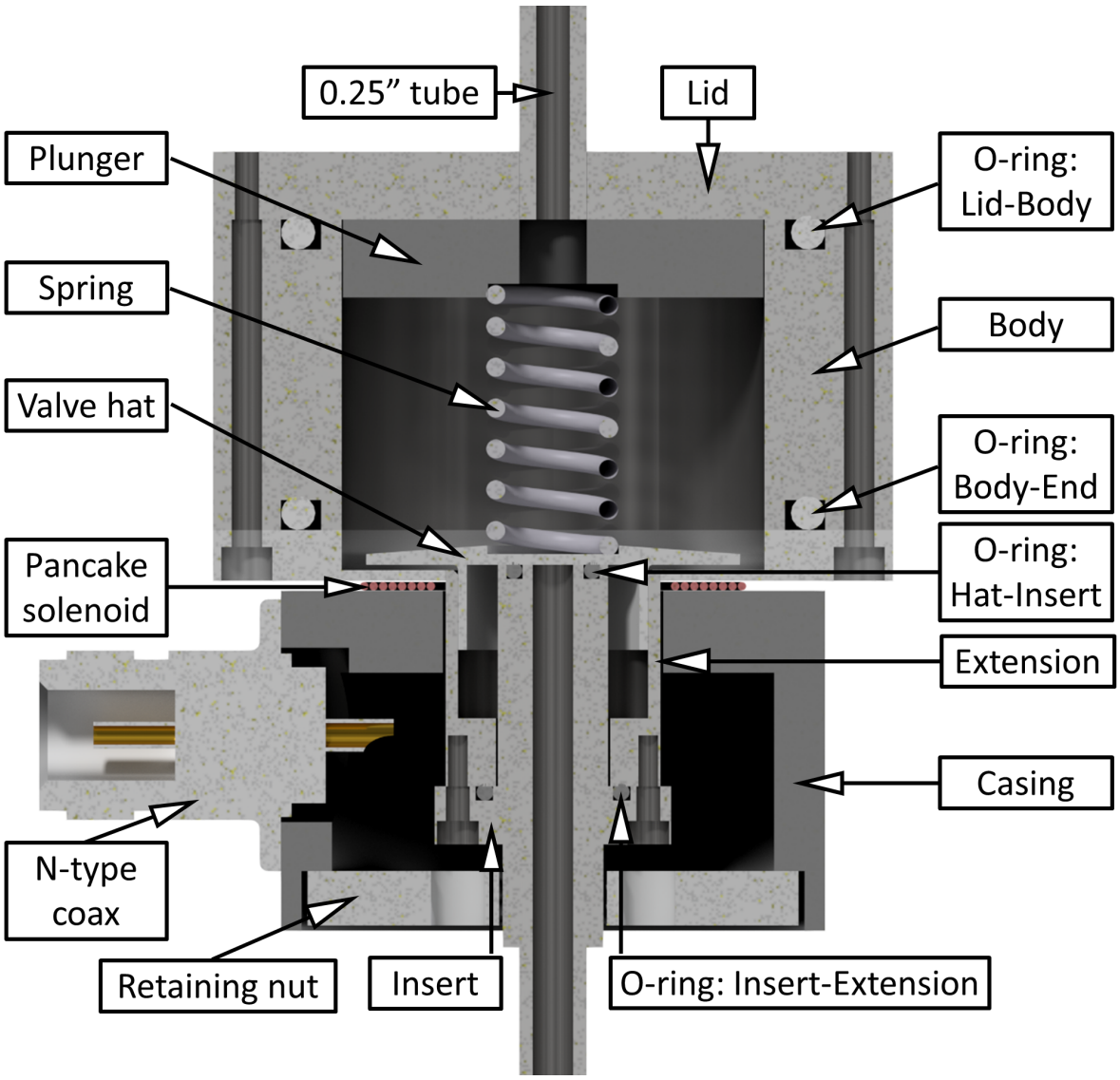

Figure B.1: Labeled valve cutaway to be used as a reference in the following relevant engineering drawings

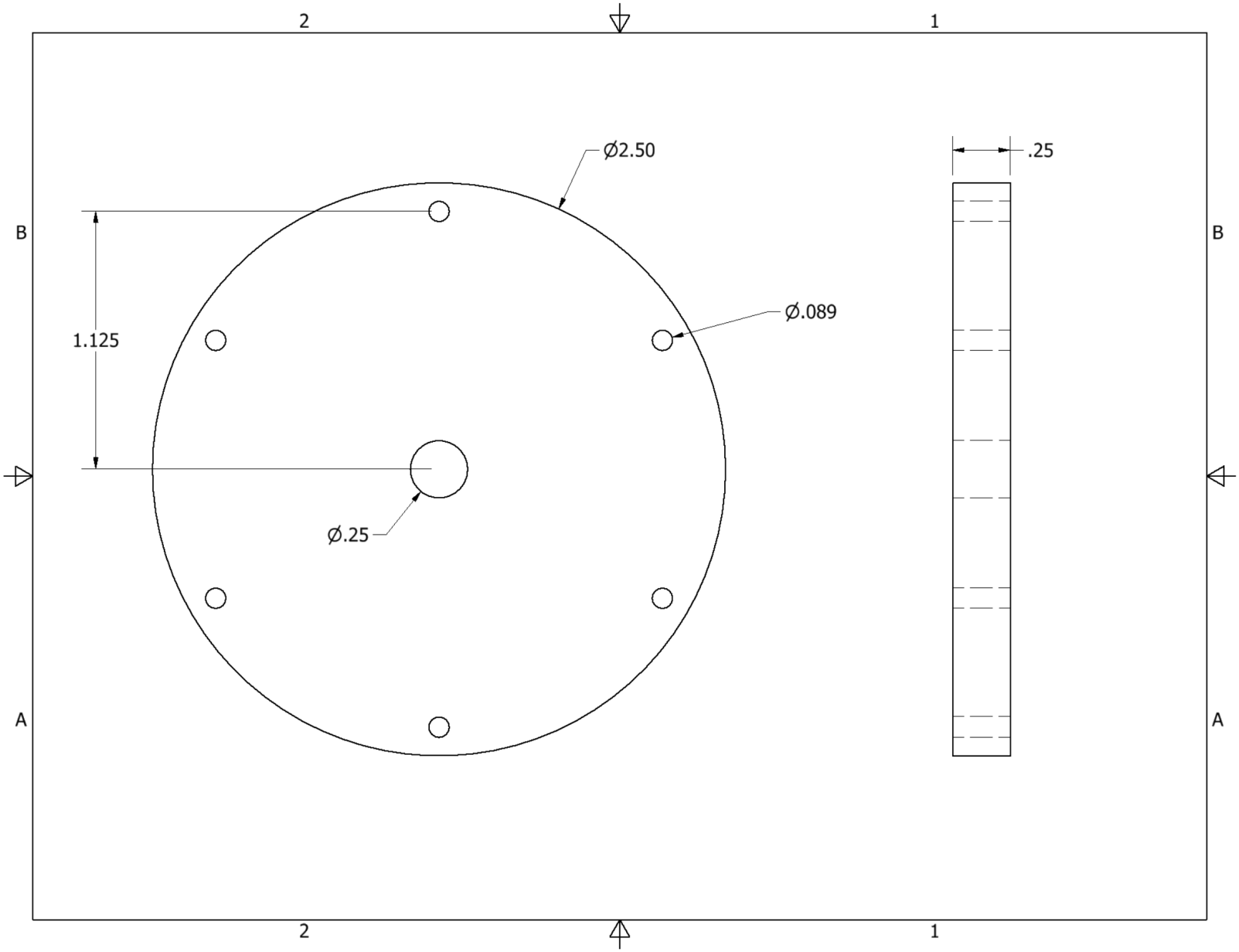

Figure B.2: Engineering drawing: Valve lid

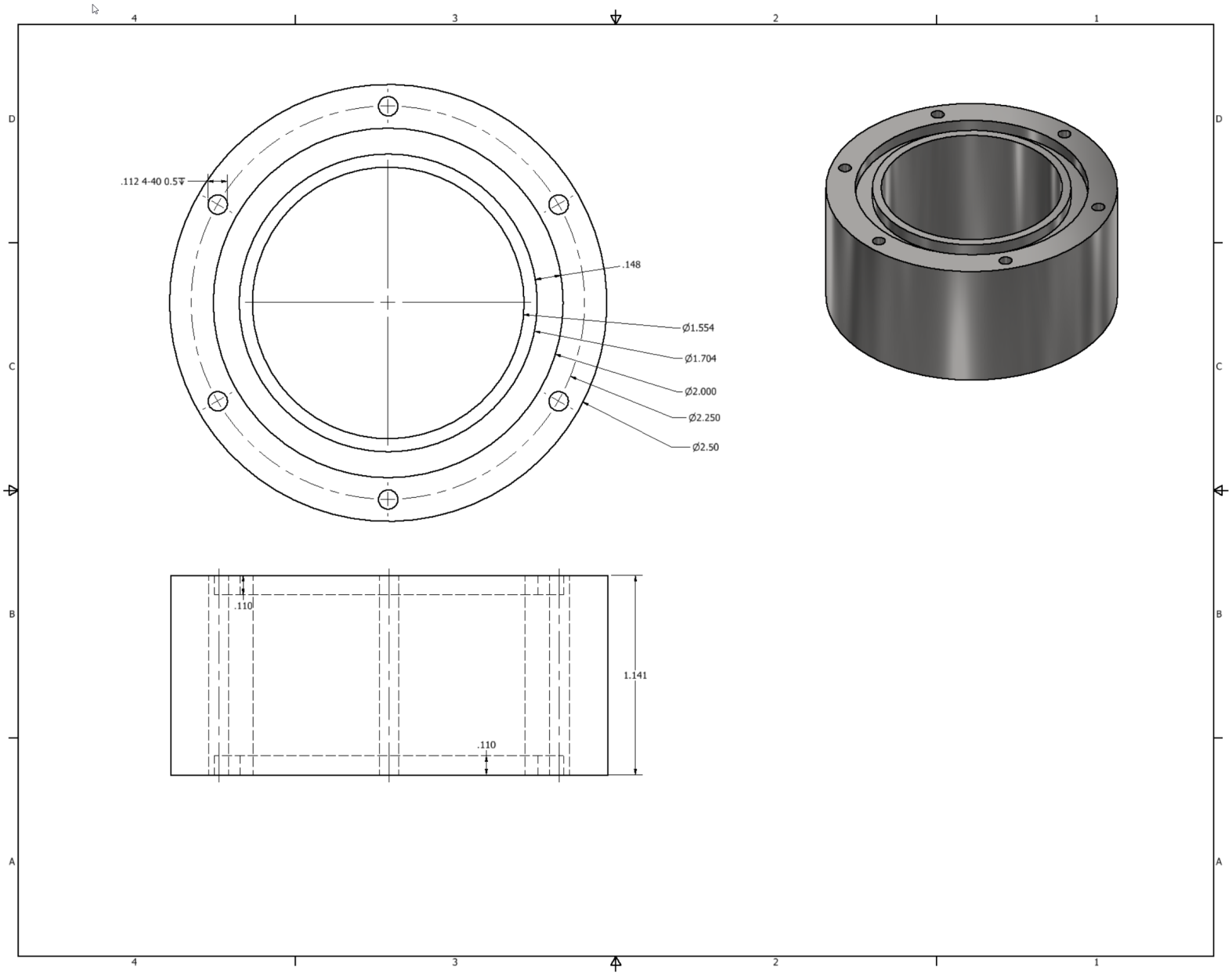

Figure B.3: Engineering drawing: Valve body

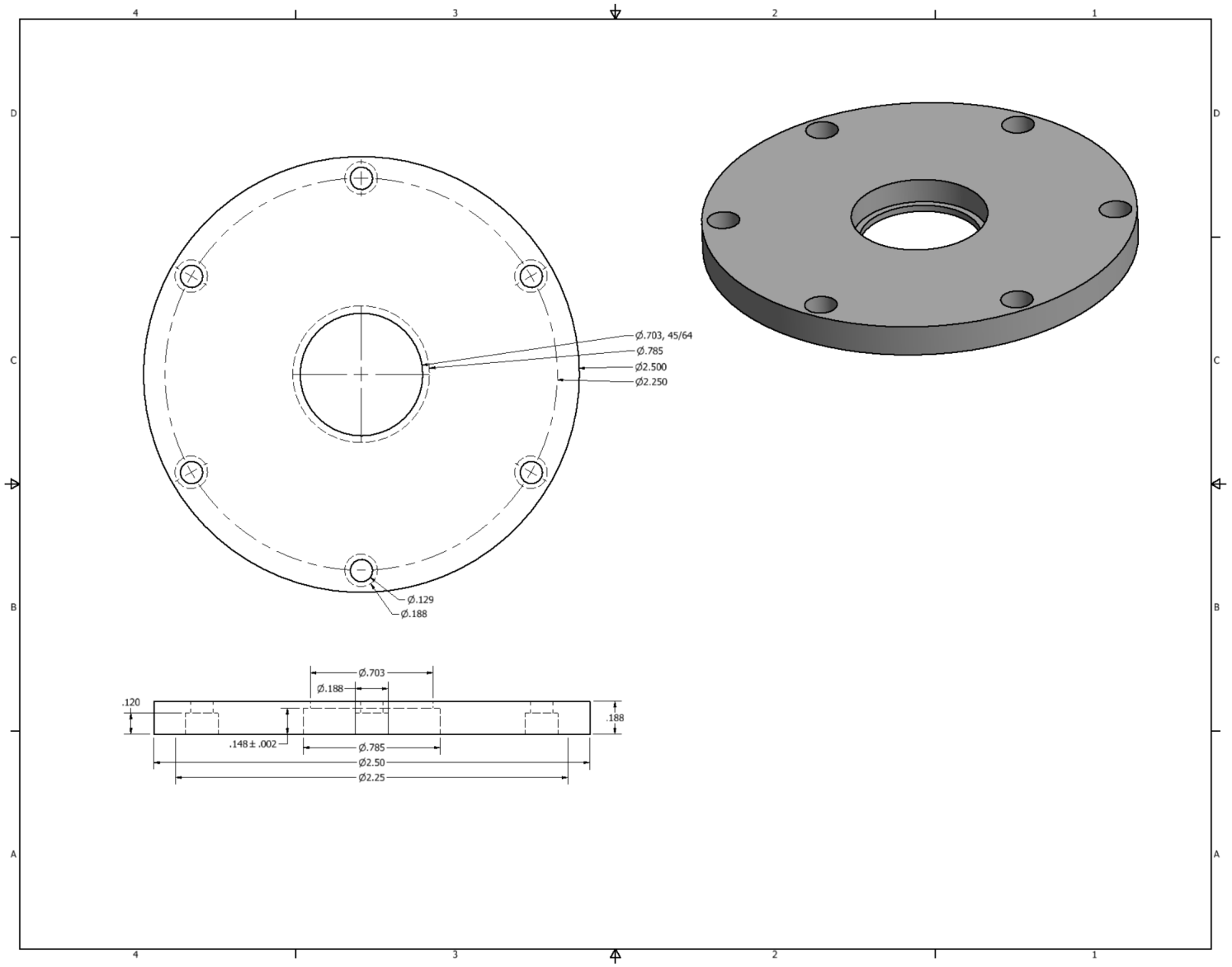

Figure B.4: Engineering drawing: Valve end before welding the extension (figure B.5) and making the modification (figure B.6)

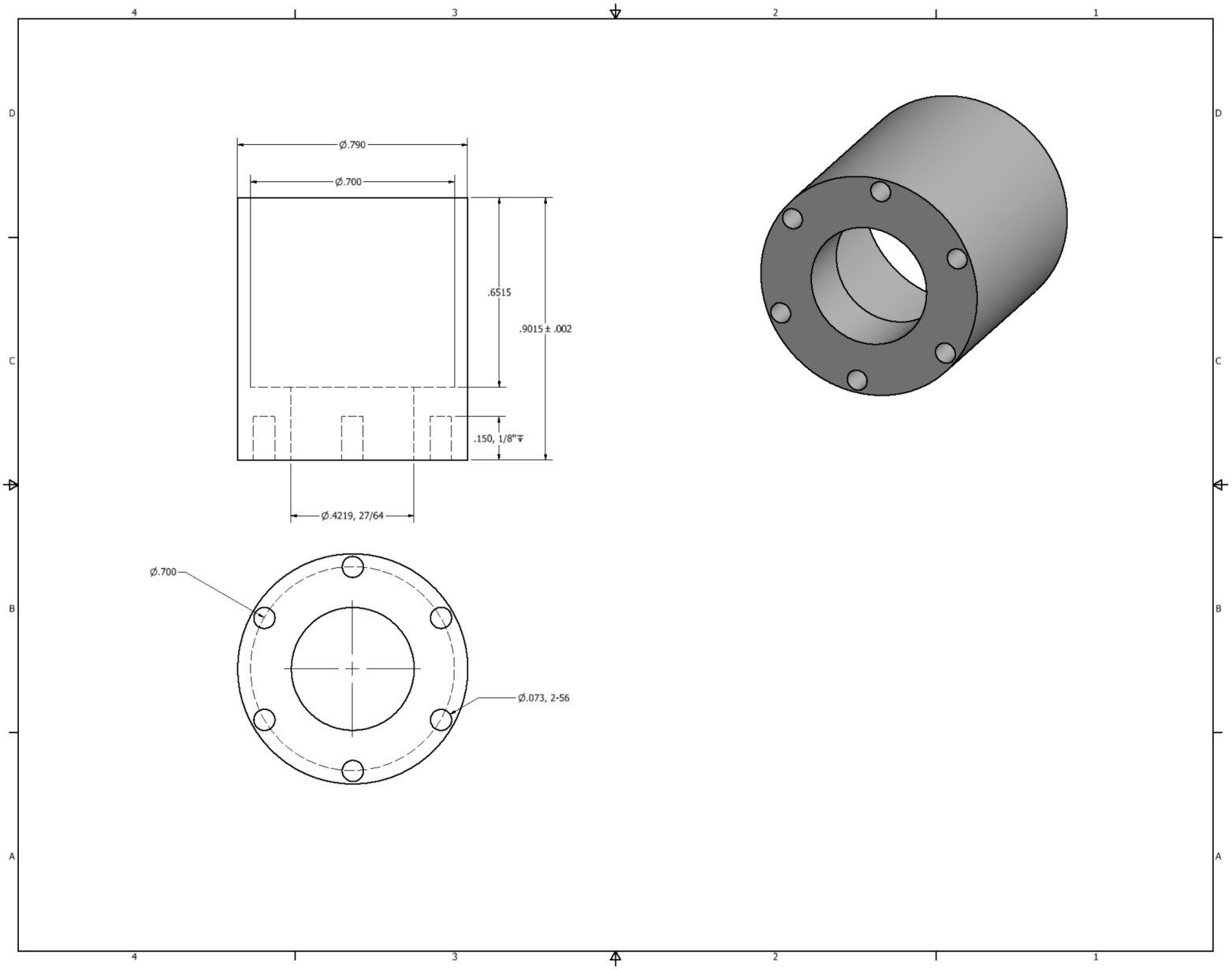

Figure B.5: Engineering drawing: Valve extension. To be welded into the initial valve end (figure B.4)

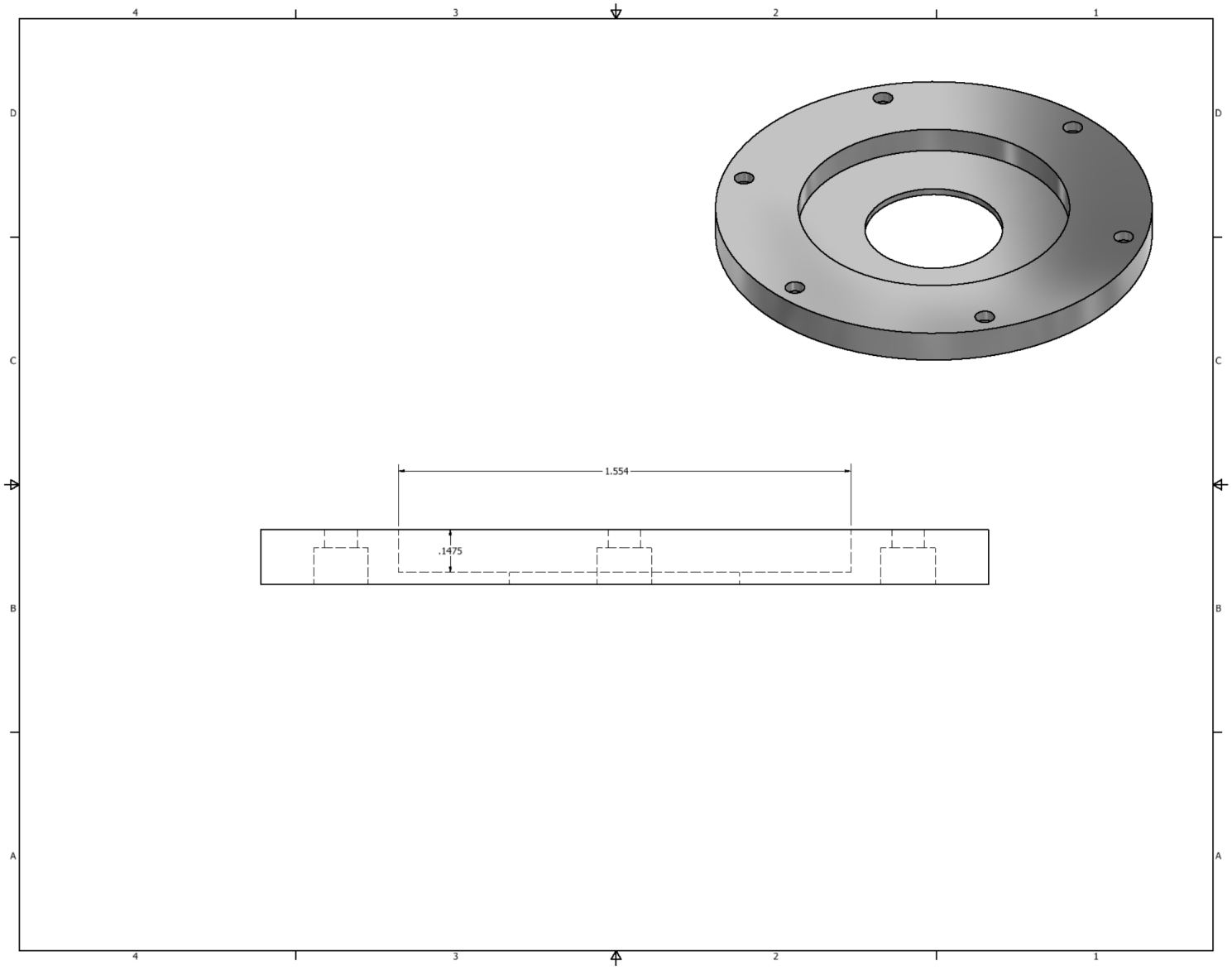

Figure B.6: Engineering drawing: Valve end modification to be made to the welded extension/initial end (figures B.5 and B.4)

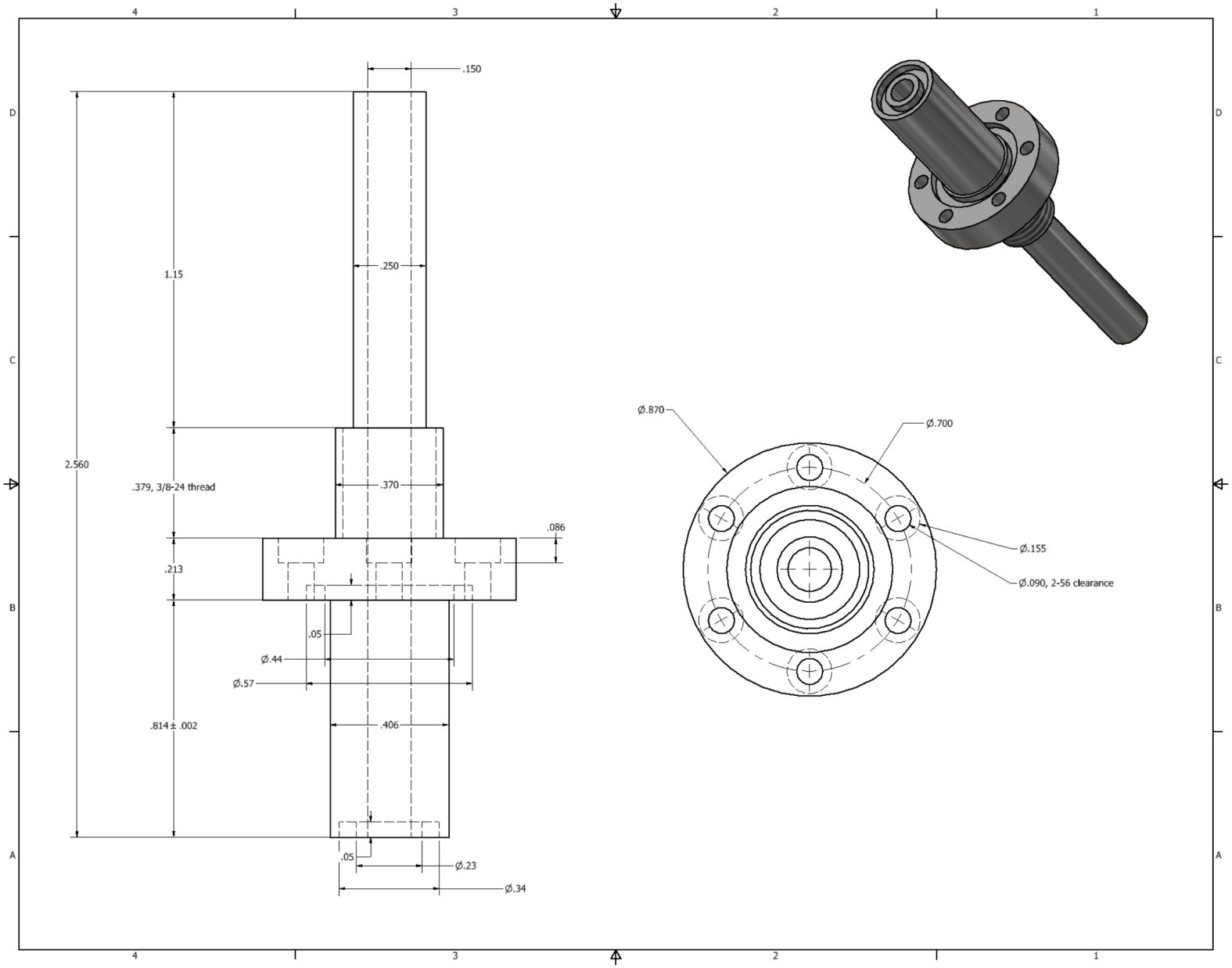

Figure B.7: Engineering drawing: Valve insert

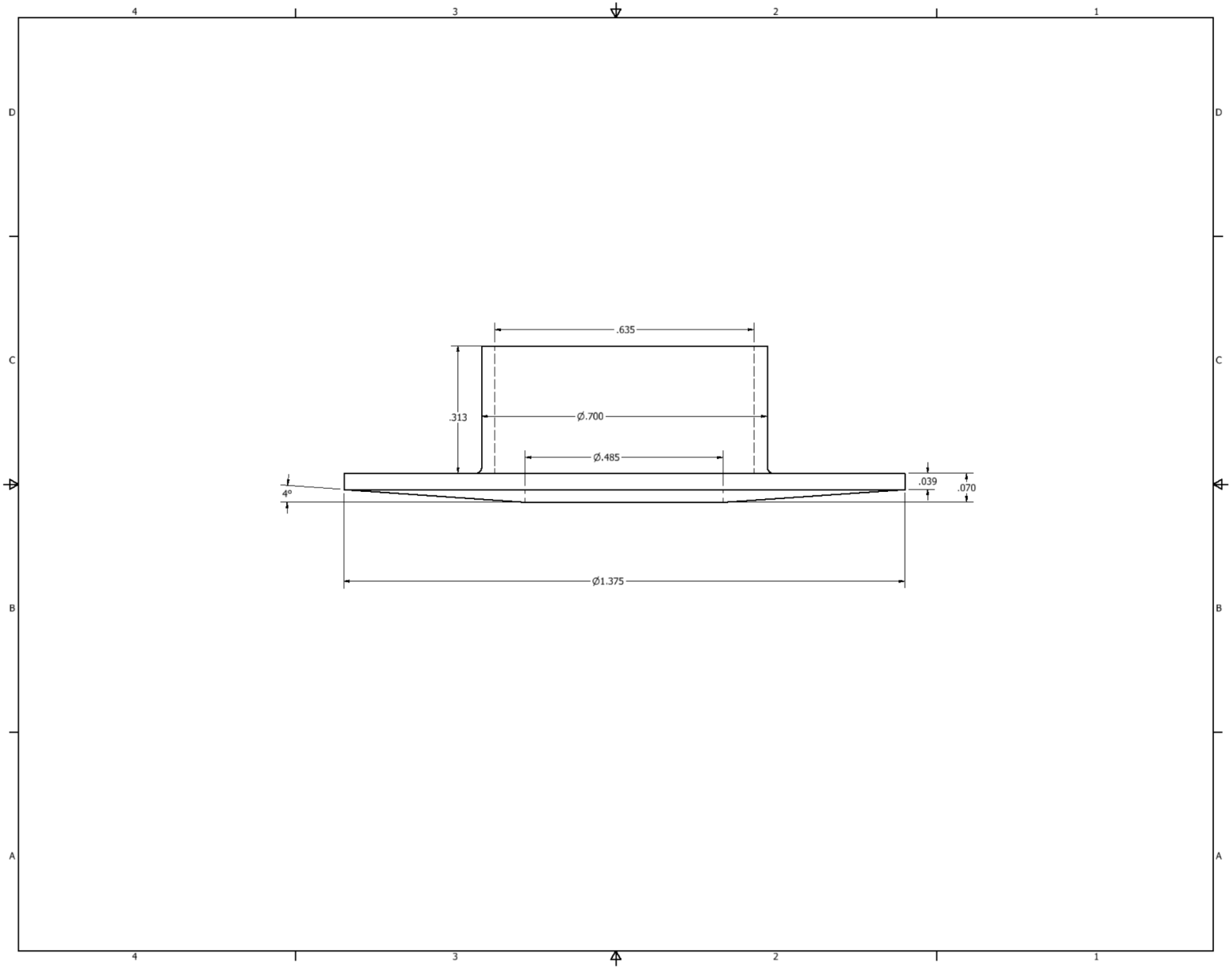

Figure B.8: Engineering drawing: Valve hat

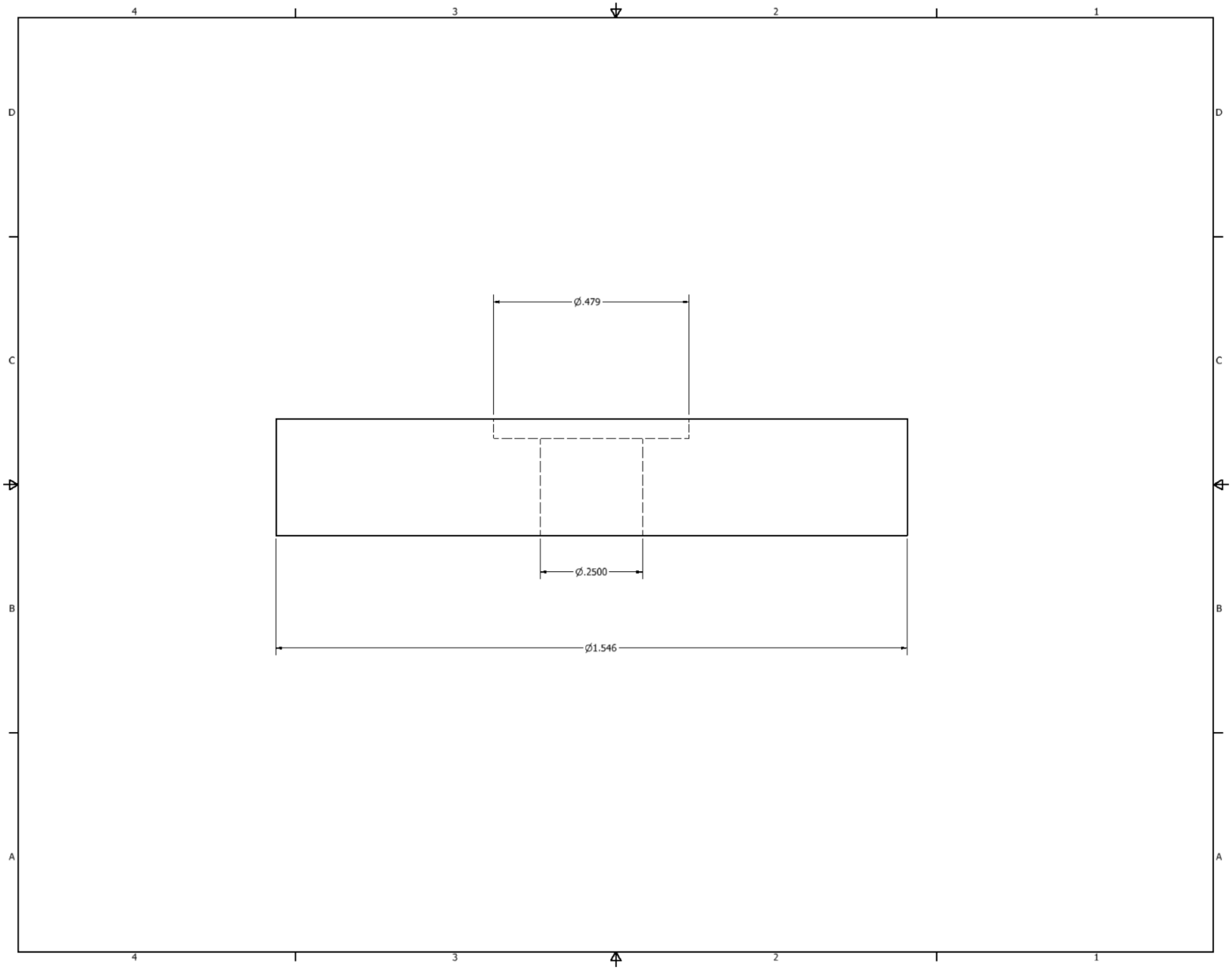

Figure B.9: Engineering drawing: Valve plunger

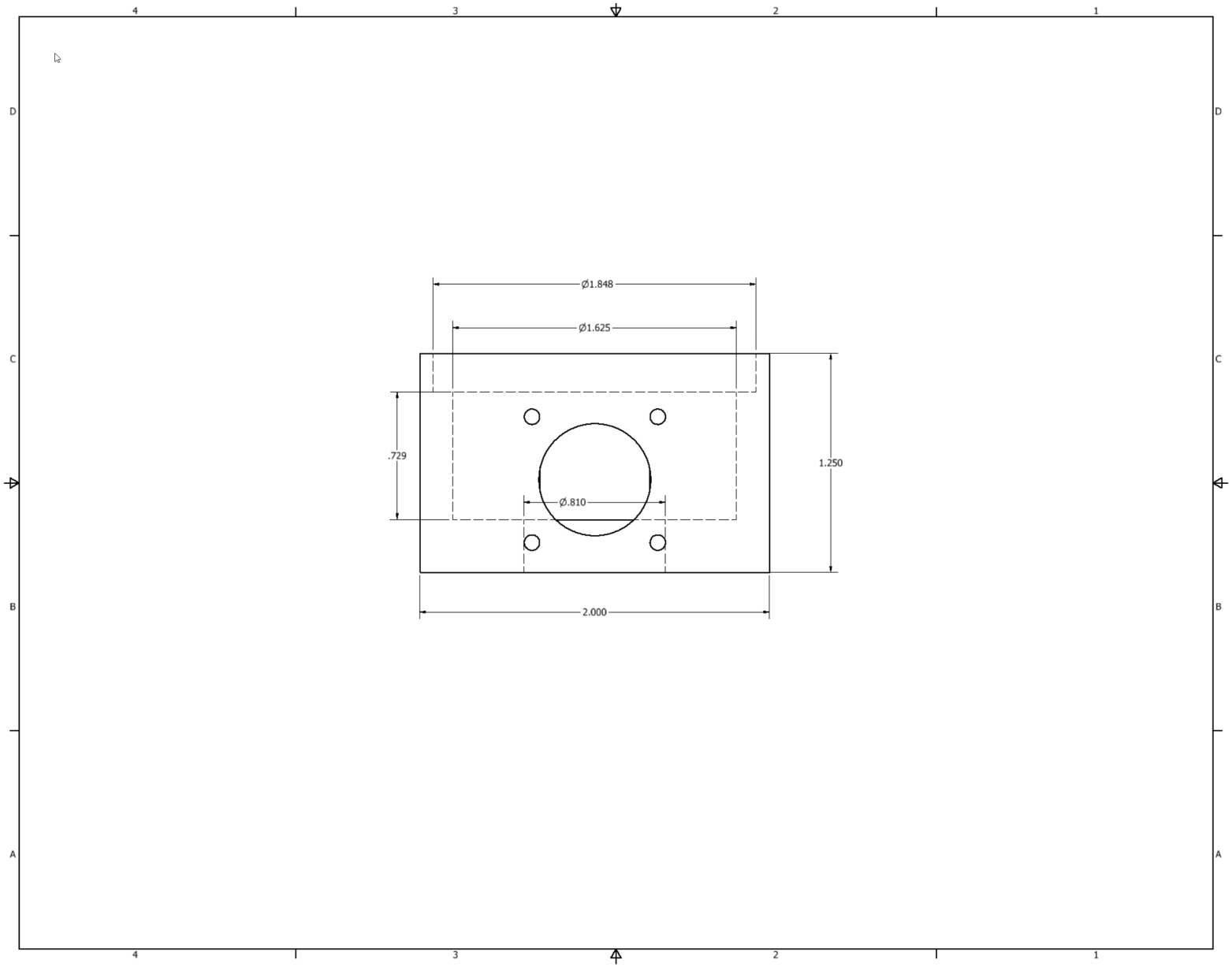

Figure B.10: Engineering drawing: Valve casing

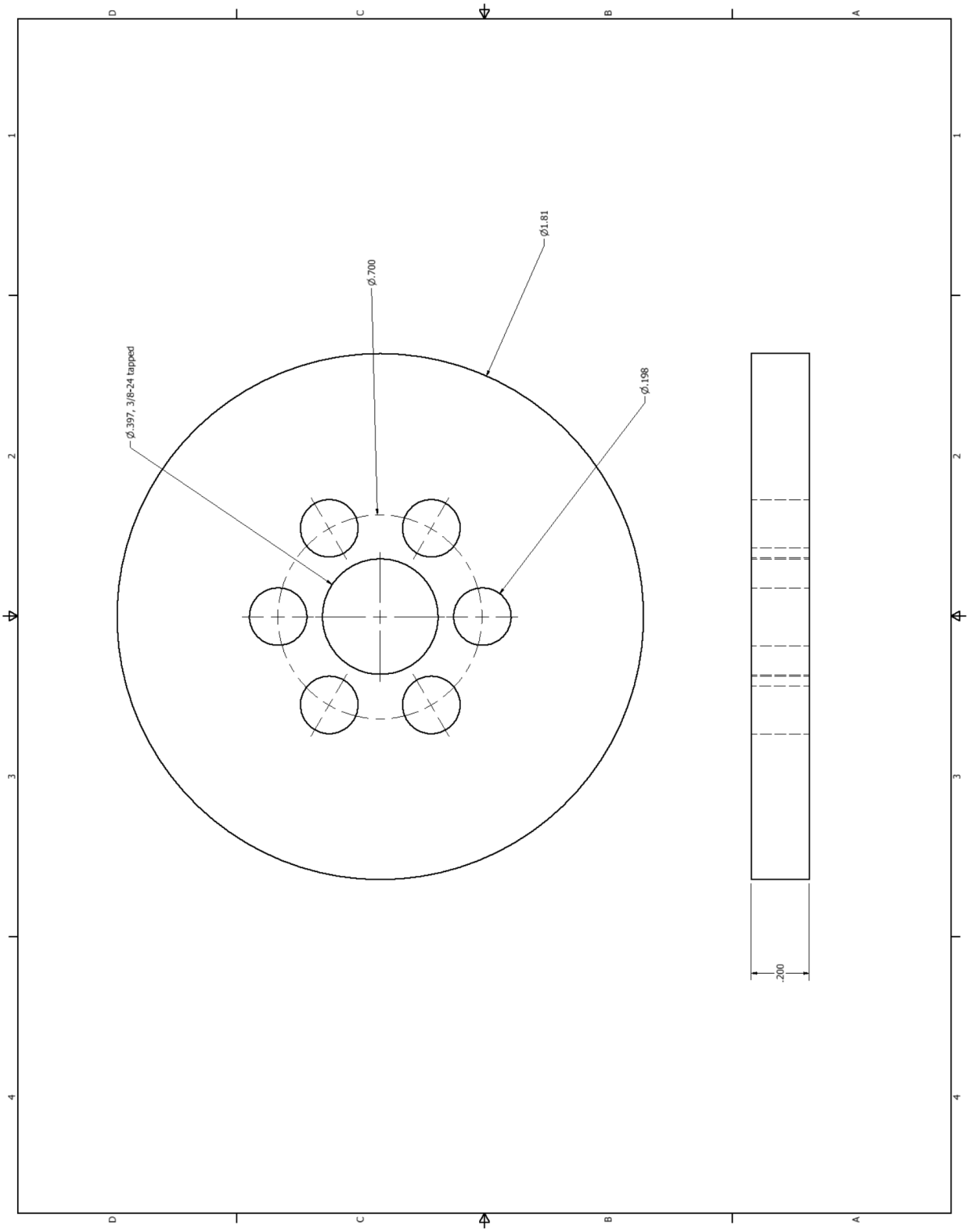

Figure B.11: Engineering drawing: Valve retaining nut

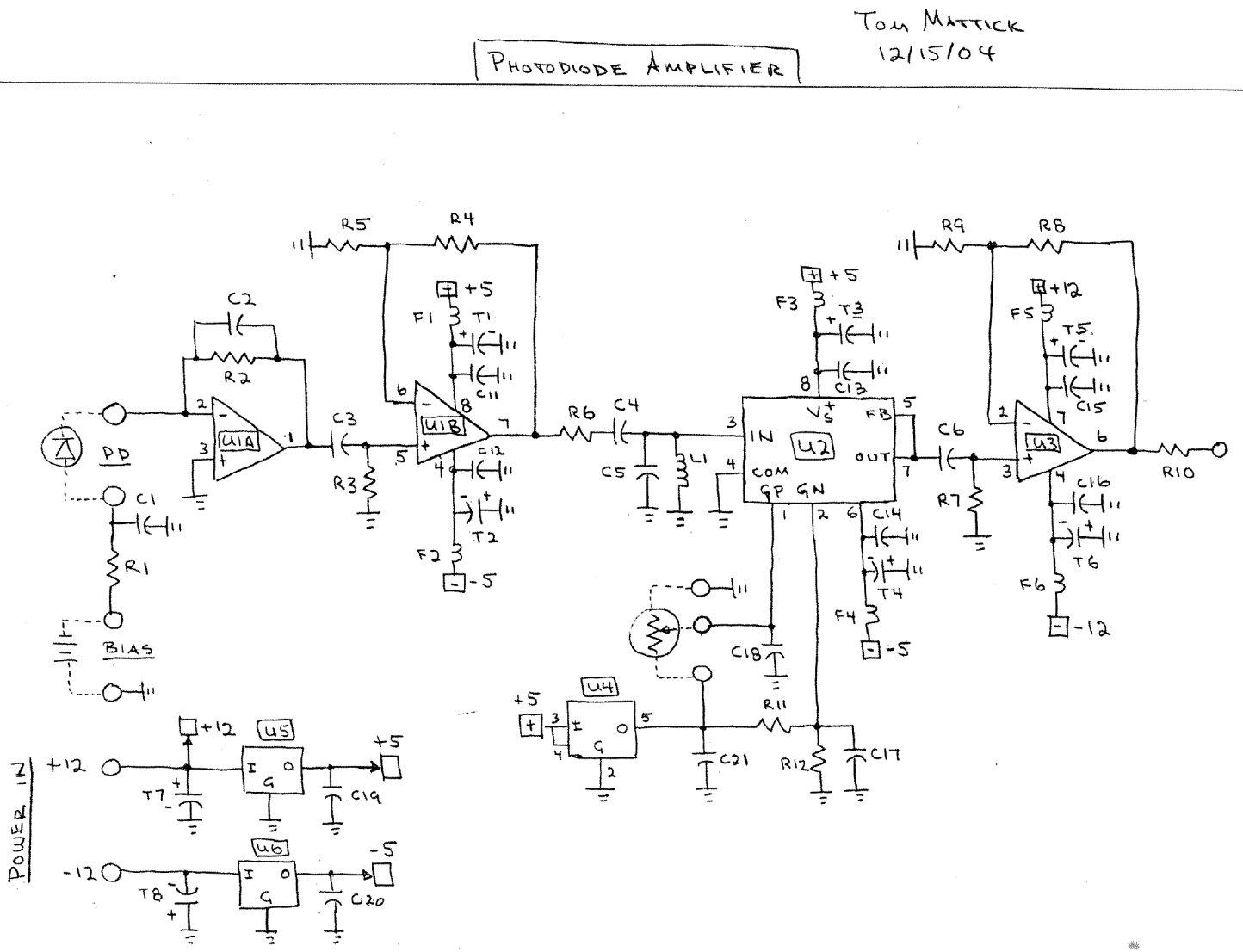

Figure B.12: Circuit diagram for the photodiode amplifier. Courtesy of Dr. Tom Mattick.

Breakdown of parts required for one PCB PD amplifier				
Item	**Package**	**Manufacturer**	**Desc.**	**# units**
Resistors				
R1, R11, R12	0603	PEC	1k Ohm, +/- 1%	3
R2, R4	0603	PEC	4.02k Ohm, , +/- 1%	2
R3, R5, R7, R9	0603	PEC	200 Ohm, +/- 1%	4
R6	0603	PEC	100 Ohm, +/- 1%	1
R8	0603	PEC	1.21k Ohm, +/- 1%	1
R10	0603	PEC	51.1 Ohm, +/- 1%	1
Capacitors				
C1	0805	AVX	0.022uF, 200V, +/- 10%	1
C2	0603	AVX	0.5pF, 50V, +/- 0.1pF = 20%	1
C3, C6	0603	muRata	200pF, 50V, +/- 5%	2
C4	0603	Kemet	10000pF (0.01uF), 50V, +/- 5%	1
C5	0805	muRata	200pF, 50V, +/- 1%	1
C11-C16	0508	AVX	0.1uF, 25V, +/- 10%	6
C17-C21	0603	Kemet	0.1uF, 25V, +/- 10%	5
Tantalum Capacitors				
T1-T4	1206	Vishay	6.8uF, 16V, "A" size - 3.2x1.6, +/- 10%	4
T5-T8	1411	Vishay	4.7uF, 25V, "B" size - 3.5x2.8, +/- 10%	4
Inductor				
L1	0603	muRata	20nH, +/- 2%	1
Ferrite Bead Clips				
F1-F6	0603	muRata	Diff mode, 600 Ohm @ 100MHz	6
Semiconductors				
U1	8-SOIC	TI	Voltage feedback, dual op-amp	1
U2	8-SOIC	Analog Dev Inc	Variable Gain Amp	1
U3	8-SOIC	TI	Current feedback op-amp	1
U4	SOT-23-5	TI	1.25V PMIC VReference, 5-pin	1
U5	SOT-89	STMicro	+5V regulator, 3-pin + tab	1
U6	SOT-89	STMicro	-5V regulator, 3-pin + tab	1

Table B.1: Chipset for one 80 MHz photodiode amplifier

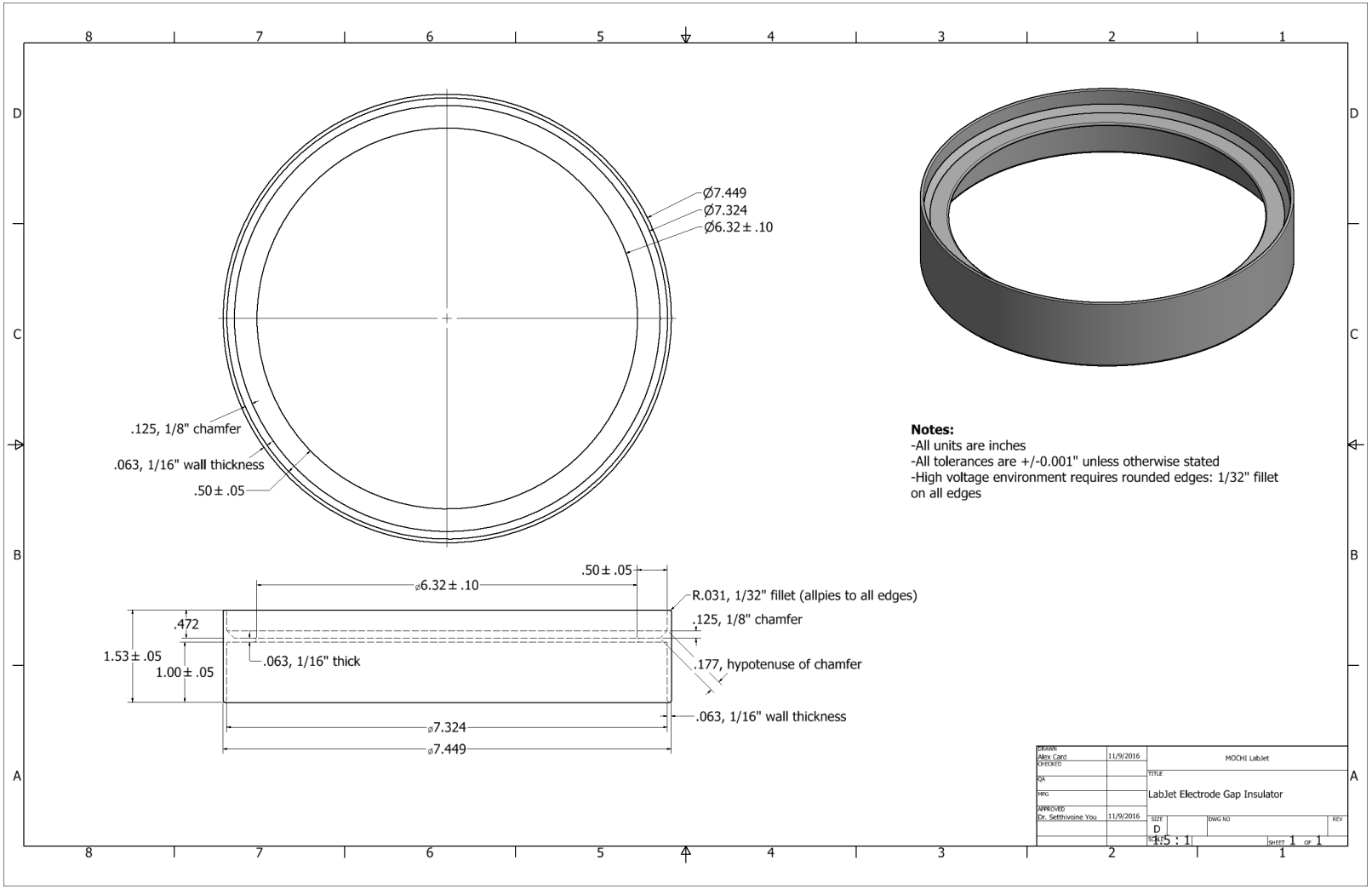

Figure B.13: Engineering drawing: Alumina end cap

Appendix C

PYTHON DENSITY ANALYSIS SOURCE CODE

The following code is used to produce the line-integrated density data. Note that modification of the *factor* and *Rmin* in the *Minimum smoothing factor* must be modified until the Lissajous figure radius does not go through zero. This is verified by visual inspection of the Lissajous figure.

Interferometer data analysis: 1st pass

 # This data analysis produces the electron density as measured by the single chord, unequal path
 # length, heterodyne, HeNe interferometer.

```
import numpy as np
import MDSplus as mds
import matplotlib.pyplot as plt
import scipy.fftpack as fftpack
import astropy.convolution as conv
from scipy import stats
import scipy.signal as sig
import seaborn as sns


default_fs = 2.1
sns.set_context('poster', font_scale=default_fs)
sns.set_style('whitegrid', {'axes.linewidth': 2, 'axes.edgecolor': 'black'})
```

```
#### Import the raw data


shotnum = 6994

tree = mds.Tree('op_tree', shotnum)


time = np.array(tree.getNode('\TIMEVALUES_TEKCH1').getData())

sine = np.array(tree.getNode('\VOLTAGEVALUES_TEKCH2').getData())

cosine = np.array(tree.getNode('\VOLTAGEVALUES_TEKCH1').getData())


#### Import the DC-offset correction reference shot and apply correction


offshot = 6814

offtree = mds.Tree('op_tree', offshot)

offsine = np.array(offtree.getNode('\VOLTAGEVALUES_TEKCH2').getData()).mean()

offcosine = np.array(offtree.getNode('\VOLTAGEVALUES_TEKCH1').getData()).mean()


sine -= offsine

cosine -= offcosine


#### Minimum smoothing factor


# The solution for the problem of phase uncertainty in the short-period initial jet lies in the
# fact that the radius of the lissajous figure goes to zero, and oscillates around the origin,
# causing unphysical $2 \pi$ jumps in the phase angle difference ($\Delta \phi$). To fix this,
# we use a while loop to increase the filter factor on the sine/cosine traces (and thus the
# lissajous radius) until the minimum value does not approach zero. Since the Radius is sign-
```

```
# less, we have to determine some minimum radius at which the while loop ends.

samp_rate = 1./(time[1]—time[0])

nyq = 0.5 * samp_rate

print 'Nyquist frequency [MHz] =', np.round(nyq/1e6)


factor = 0.3

Rmin = 3. # [mV]


print 'Initial loop factor =', factor

normal_cutoff = factor*nyq / nyq

butter = sig.butter(5, normal_cutoff)

sin_nonoise = sig.filtfilt(butter[0], butter[1], sine)

cos_nonoise = sig.filtfilt(butter[0], butter[1], cosine)


R = np.sqrt(sine**2. + cosine**2.)


while 1 > 0:

    outlier = 0

    R_nonoise = np.sqrt(sin_nonoise**2. + cos_nonoise**2.)


    for i in range(len(R_nonoise)):

        if R_nonoise[i]/1e—3< Rmin:

            outlier = 1


    if outlier == 1:

        factor —= 0.01
```

```
        print '(Factor decrement to '+str(factor)+')'
        normal_cutoff = factor*nyq / nyq
        butter = sig.butter(5, normal_cutoff)
        sin_nonoise = sig.filtfilt(butter[0], butter[1], sine)
        cos_nonoise = sig.filtfilt(butter[0], butter[1], cosine)

    else:
        break

print 'LP Filter cutoff [kHz] (@ '+ str(100*factor) +'% nyq_freq) =',
                                                    np.round(factor*nyq/1e3)
```

Error analysis

```
ocosine = cosine — cos_nonoise
osine = sine — sin_nonoise

NoiseMag_cos = np.abs(ocosine)
NoiseMag_sin = np.abs(osine)

sigma_S1 = ocosine#NoiseMag_cos
sigma_S2 = osine#NoiseMag_sin

S1 = cos_nonoise
S2 = sin_nonoise

sigma_delphi = np.sqrt(( —(S2 * sigma_S1) / (S1**2. + S2**2.) )**2.
```

```
                                        + ( (S1 * sigma_S2) / (S1**2. + S2**2.) )**2.)
```

Aside: Lissajous figures

```
lissashot = 6815
lissatree = mds.Tree('op_tree', lissashot)
lissatime = np.array(lissatree.getNode('\TIMEVALUES_TEKCH1').getData())
lissasine = np.array(lissatree.getNode('\VOLTAGEVALUES_TEKCH2').getData())
lissacosine = np.array(lissatree.getNode('\VOLTAGEVALUES_TEKCH1').getData())


lissasine -= offsine
lissacosine -= offcosine
```

Final lissajous

```
sns.set_context('poster', font_scale=1.5)
plt.figure()
plt.clf()
size = 80
t1 = 250-1; t2 = 750+1
plt.scatter(cosine[t1:t2]/1e-3, sine[t1:t2]/1e-3,  c=time[t1:t2]/1e-6, s=size,
                    label=r'Unfiltered', zorder=1)
plt.colorbar(label=r'Time [$\mu$s] (unfiltered signal) ')
plt.plot(cos_nonoise[t1:t2]/1e-3, sin_nonoise[t1:t2]/1e-3, 'k', linewidth=1,
             zorder=2)
plt.scatter(cos_nonoise[t1:t2]/1e-3, sin_nonoise[t1:t2]/1e-3,  c=time[t1:t2]/1e-6,
                        cmap='gist_rainbow', s=size,
```

```
                label=str(np.round(factor*nyq/1e3))+' Filtered', zorder=3)

num = np.arange(0, 2500)
#for i in range(len(sine)):
#    plt.annotate(str(num[i]), ( cos_nonoise[num[i]]/1e-3, sin_nonoise[num[i]]/1e-3))
plt.colorbar(label=r'Time [$\mu$s] (filtered signal)')
plt.xlabel(r'$S_1$ [mV]'); plt.ylabel(r'$S_2$ [mV]')
#plt.title('Shot-duration Lissajous figure, shot ' + str(shotnum))
axlim = 25.
plt.xlim([-axlim-5, axlim]); plt.ylim([-axlim, axlim])
plt.annotate('#'+str(shotnum), xy=(0.82, 0.93), xycoords='axes fraction', size=30)
#plt.text(axlim-10, axlim-5, '#'+str(shotnum), size=20)
#plt.legend()
plt.grid(True, linewidth=2)
plt.tight_layout()
plt.savefig('./un_filtered_lissajous_shot'+str(shotnum)+'.png', dpi=300)
plt.show()


#### Obtain $\Delta \phi$

# The first step is to use the arctan2 function to produce the 'absolute' angle
# relationship of the smoothed data traces. Since arctan2 is defined in the range
# [-$\pi$, $\pi$], we have to add $2 \pi$ to data points located in quadrants $III$ and
# $IV$. This will produce the correct angle in the range [0, $2 \pi$].
#
# The next step is to correct for fringe jumps. A fringe jump is defined when the phase
# angle moves over the 0/$2 \pi$ boundary. To do so, we set the maximum jump that any two
```

```
# points can have to be $\pi$. Therefore if a point changes by a value larger than $\pi$
# relative to the previous, we say that it is due to a fringe jump and add/remove $2 \pi$
# accordingly.

delphi_rad = np.arctan2(sin_nonoise, cos_nonoise)
delphi_deg = delphi_rad * 180. / np.pi

delphi_adj = delphi_rad

for i in range(len(delphi_adj)):
    if np.sign(sin_nonoise[i]) < 0.:
        delphi_adj[i] += 2.*np.pi

loopnum = np.zeros(len(delphi_adj))
loop = 0.

for j in range(len(loopnum)-1):

    val = delphi_adj[j+1] - delphi_adj[j]
    #print delphi_adj[j+1], delphi_adj[j], val, loop

    if np.abs(val) > np.pi:
        if val < -np.pi:
            loop += 1.
        if val > np.pi:
            loop -= 1.
```

```
    loopnum[j+1] = loop
```

```
#for k in range(len(loopnum)):
#    print k, loopnum[k]
```

```
delphi_loop = delphi_adj + (2.*np.pi*loopnum)
```

```
####Remove background vibration trend
```

```
ind_offset = 250
polyfit = np.polyfit(time[0:ind_offset], delphi_rad[0:ind_offset], 1)
polyfit1d = np.poly1d(polyfit)
fit = polyfit1d(time)
delphi_shift = delphi_loop - fit
delphi = np.abs(delphi_shift)
```

```
####Summary plot of background removal
```

```
plt.figure()
plt.clf()
plt.plot(time/1e-6, delphi_loop, label='Initial')
plt.plot(time/1e-6, fit, 'r', label='Linear fit')
plt.plot(time/1e-6, delphi, 'g', label='Corrected')
plt.xlabel(r'$Time\/[\mu s]$'); plt.ylabel(r'$\Delta \phi\/[rad]$')
#plt.title('Phase angle difference, shot ' + str(shotnum))
plt.legend(loc=2)
#plt.xlim(time.min()/1e-6, time.max()/1e-6)
```

```
plt.xlim(-50, 150)

plt.tight_layout()

plt.savefig('./analysis_plots/delphi_subtract'+'_shot'+str(shotnum)+'.png', dpi=300)

plt.show()
```

Apply calibration factor: $\bar{n_e} =2.78x10^{20}\Delta \phi$ $[m^{-2}]$

```
calfac = 2.78e20

neL = calfac*delphi

sigma_neL = calfac*sigma_delphi
```

Plot of $\overline{n} _e$

```
sns.set_context('paper', font_scale=2.1)

sns.set_style({'axes.linewidth': 2, 'axes.edgecolor': 'black'})


ymax = 1.75e21

plt.figure(9)

plt.clf()
```

#plt.fill_between(time[511:551]/1e-6, 0., ymax, color='#4dff4d', label='Jet Region')

#plt.plot(time/1e-6, neL, c='#999999', label='Unfiltered')

```
plt.fill_between(time/1e-6, neL-sigma_neL, neL+sigma_neL)

plt.plot(time/1e-6, neL, 'k', linewidth=1)

plt.xlabel(r'Time [$\rm{\mu s}$]'); plt.ylabel(r'$\rm{\overline{n} _e}$  [$\rm{m^{-2}}$]')
```

#plt.title('Line-integrated electron density, shot ' + str(shotnum))

```
plt.xlim(0., 100.)
```

#plt.xlim(time.min()/1e-6, time.max()/1e-6)

```
plt.ylim([0., ymax])

#plt.legend()

plt.grid(True, linewidth=2)

#plt.text(82.5, ymax-0.1e21, '#'+str(shotnum), size=20)

plt.annotate('#'+str(shotnum), xy=(0.82, 0.88), xycoords='axes fraction', size=20)

plt.tight_layout()

plt.savefig('./density_LOS_shot'+str(shotnum)+'.png', dpi=300)

plt.show()


####Save array to file


a = np.asarray([time, neL, sigma_neL])

np.savetxt('./shot'+str(shotnum)+'.csv', a, delimiter=',')
```

VITA

Alexander Card earned a dual B.S. degree at the University of Minnesota in the fields of Physics and Astrophysics in 2013. He sought to study experimental laboratory astrophysics; a hands-on approach to the stellar sciences. He found a position in the Dept. of Aeronautics & Astronautics at the University of Washington, focusing on astronautics. He intends to continue this pursuit down the path of fusion sciences, for in the pursuit of studying laboratory astrophysics, what could be more fitting than recreating the stellar furnaces themselves?